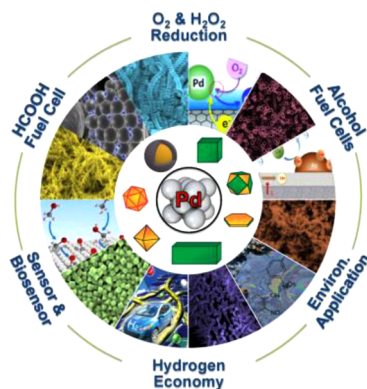


## Palladium-Based Nanomaterials: Synthesis and Electrochemical Applications

Aicheng Chen\* and Cassandra Ostrom

Department of Chemistry, Lakehead University, 955 Oliver Road, Thunder Bay, Ontario P7B 5E1, Canada



### CONTENTS

1. Introduction	11999
2. Synthesis and Properties of Pd and Pd-Based Nanomaterials	12000
2.1. Structure and Size Effects	12000
2.2. Physical Synthesis Techniques	12003
2.3. Hydrothermal Methods	12004
2.4. Electrochemical Deposition	12006
2.5. Chemical Reductions and Other Methods	12010
3. Electrochemical Applications of Pd and Pd-Based Nanomaterials	12014
3.1. Direct Alcohol Fuel Cells	12014
3.1.1. Electrochemical Oxidation of Methanol	12014
3.1.2. Electrochemical Oxidation of Ethanol	12017
3.2. Electrochemical Oxidation of Formic Acid	12020
3.3. Electrochemical Reduction of Oxygen	12022
3.4. Electrochemical Reduction of Hydrogen Peroxide	12024
3.5. Toward a Hydrogen Economy	12026
3.5.1. Hydrogen Production and Purification	12026
3.5.2. Hydrogen Storage	12027
3.6. Gas Sensors	12029
3.7. Electrochemical Biosensors	12031
3.8. Other Applications	12032
4. Conclusions and Outlook	12033
Author Information	12034
Corresponding Author	12034
Notes	12034
Biographies	12034
Acknowledgments	12034
References	12034

### 1. INTRODUCTION

Cumulative anthropogenic energy demands, coupled with continual increases in carbon dioxide emissions, have triggered

a critical need for the use of non-fossil-fuel resources. Sustainable alternatives, including solar, wind, geothermal, wave energy power, and fuel cells, are being actively pursued. Fuel cells are considered to be a leading alternative green energy technology with applications spanning myriad areas including transportation, portable power, and stationary power generation.<sup>1–4</sup> Currently, Pt-based electrocatalysts are predominant, but they are expensive and in limited supply. As an alternative, the design of highly active and stable catalysts using Pd and Pd-based nanomaterials has become an area of intense interest.<sup>5–7</sup> Pd is well-known for its high affinity for hydrogen, which facilitates the broad use of Pd nanomaterials as primary catalysts, encompassing a wide variety of applications, particularly in organic coupling synthesis,<sup>8,9</sup> hydrogen detection, purification, and storage.<sup>10</sup>

Comparatively speaking, the abundance of Pd within the crust of the Earth is 0.015 ppm by weight, which is 3-fold higher than that of Pt (0.005 ppm), positioning their relative costs at ca. \$614 and \$997 per ounce, respectively (Kitco Gold Index, Aug 15, 2015). However, it is worth noting that although the relative price of Pd in comparison to Pt is lower, the price of Pd remains above acceptable levels for large-scale commercial applications. It may be expected that as interest in the applications of Pd materials intensifies, its cost may increase further. Nevertheless, the replacement of scarce Pt noble metal with more abundant materials is a critical step in the development of sustainable catalysts. Through the use of diverse synthesis techniques, Pd-based nanomaterials have the potential to provide superior and cost-effective solutions to meet the requirements of present and evolving electrochemical applications, specifically the development of a hydrogen economy.

This comprehensive review will examine the synthesis methods, the dimensional and morphological effects, and the electrochemical applications of nanostructured Pd and Pd-based materials. Effective methodologies aimed at reducing the usage of Pd in electrochemistry with enhanced catalytic activity and stability are also discussed. This review topic aligns well with the currently intense research and development of high-performance fuel cell technologies and a hydrogen economy. The U.S. Department of Energy (DOE) Fuel Cell Technologies Office has recently established major milestones to guide rapidly emerging fuel cell technologies, such as a durability target of 5000 h with less than 10% loss of performance, automotive fuel cell system target cost of \$40 per kilowatt, and a reduced platinum group metal content and loading target of 0.125 g/kW by 2020. In step with efforts

Received: May 30, 2015

Published: September 24, 2015



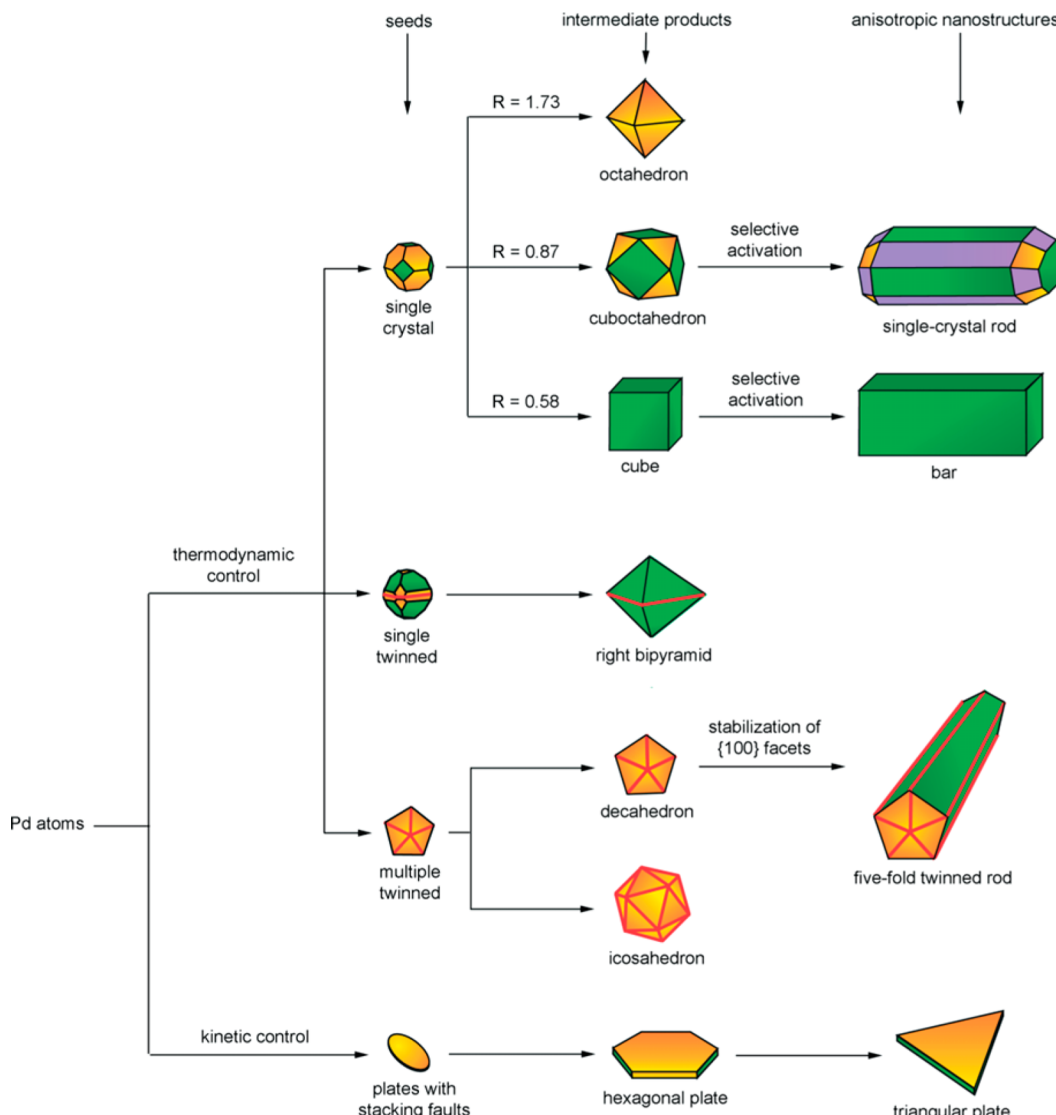


**Figure 1.** Schematic illustration of the reaction pathways that lead to Pd nanostructures with different morphologies. Green, orange, and purple represent the {100}, {111}, and {110} facets, respectively. Twin planes are delineated in the figure with red lines. The parameter R is defined as the ratio between the growth rates along the ⟨100⟩ and ⟨111⟩ axes. Reprinted with permission from ref 13. Copyright 2007 Wiley-VCH Verlag GmbH & Co.

aimed at transitioning these innovative technologies to the marketplace, the demand for efficient Pd-based catalysts will undoubtedly increase. The intent of this critical review is to serve as a useful reference to facilitate further research and development in this significant and fascinating domain.

This review continues with section 2, which explores various techniques for the synthesis of Pd and Pd-based nanomaterials, inclusive of the influences of different parameters, along with the impacts of structure and size on catalytic activity. Section 3 examines the electrochemical applications of Pd and Pd-based nanomaterials that may serve as catalysts for the oxidation of various alcohols (e.g., methanol and ethanol) and formic acid toward their use in fuel cells. Furthermore, section 3 surveys the electrochemical reduction of oxygen and hydrogen peroxide. Critical aspects of a hydrogen economy are also described, encompassing hydrogen production, purification, and storage. Finally, the incorporation of Pd and Pd-based nanomaterials into gas sensors, electrochemical biosensors, and other applications is discussed.

## 2. SYNTHESIS AND PROPERTIES OF PD AND PD-BASED NANOMATERIALS

### 2.1. Structure and Size Effects

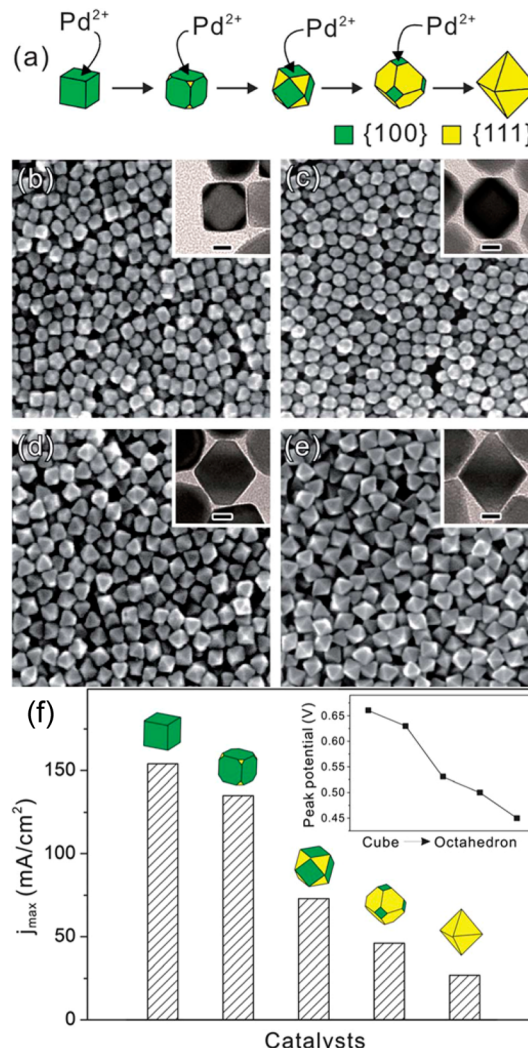
The morphologies and dimensions of Pd nanomaterials are critical aspects that enable the optimization of their performance over a broad range of applications. The dimensions of nanomaterials facilitate the determination of their specific surface areas, while their morphology controls the arrangement of facets and surface structures.<sup>11–13</sup> With Pd playing a central role in a number of environmental and energy applications, the controlled synthesis of Pd nanomaterials is essential for enabling specific catalytic properties.

As a face-centered cubic (fcc) metal, Pd has the capacity to form a variety of geometrical shapes.<sup>13–16</sup> These myriad morphologies may be achieved through the manipulation of either the thermodynamics or the kinetics involved in crystal growth. Thermodynamic mediation occurs predominantly at rapid reduction rates, while slower reduction transitions the synthesis to a kinetically mediated mode, due to changes in the

concentrations of Pd seed aggregation.<sup>7,13,17</sup> A summary of the major Pd nanostructured shapes that have been observed under various experimental conditions is presented in Figure 1. The crystallinity of Pd seeds plays the most essential role in controlling the morphology of the final products.<sup>7,15,18–24</sup> Shapes such as octahedrons, cuboctahedrons, or cubes may evolve from single-crystal seeds, contingent on the ratio of growth rates along the [111] and [100] directions. When the seeds are twinned, the evolution of growth becomes dependent on the presence and stability of the {100}, {111}, and {110} facets.<sup>7,13</sup> Morphological aspects offer greater versatility than dimensions and other parameters when tuning the catalytic properties of nanocrystals, as a result of the ability of atoms that are resident in different facets to possess diverse activity.<sup>7,12,25–27</sup> Over the past decade, the number of reports in the literature that investigate the catalytic properties of nanoparticles with various well-defined shapes, has grown substantially. Among other groups, important contributions to the understanding of shape–reactivity relationships have been made by Xia et al.,<sup>13,28</sup> Burda et al.,<sup>29</sup> Narayanan et al.,<sup>30</sup> and Niu et al.<sup>16</sup>

As a further example, Jin et al.<sup>31</sup> demonstrated the seed-mediated synthesis of Pd nanocrystals with controlled sizes, shapes, and different proportions of {100} and {111} facets (Figure 2a–e). The synthesized nanocrystalline shapes included Pd cubes, truncated cubes, cuboctahedrons, truncated octahedrons, and octahedrons. The Pd polyhedrons were characterized via the proportions of their {100} to {111} facets, and tested for correlations between surface structures and catalytic performance in the oxidation of formic acid. The maximum current densities decreased in the order cubes > truncated cubes > cuboctahedrons > truncated octahedrons > octahedrons, indicating that the oxidation of formic acid on Pd(100) was more rapid than that on Pd(111). As well, the geometry of the Pd polyhedron had an impact on the anodic peak potential, resulting in a similar trend with increased proportions of {100} to {111} (Figure 2f). The dimensions of the polyhedrons were determined by the edge length, in the range spanning 14–37 nm. As the edge length was reduced, the maximum current density remained constant, suggesting that size was not a major factor for significant change toward the catalytic activity of formic acid oxidation. Additionally, in work by Yarulin et al.,<sup>12</sup> Pd cubes, octahedrons, and cuboctahedrons containing {100}, {111}, and {100}/{111} facets, respectively, were synthesized and tested for their catalytic activity in selective acetylene hydrogenation. It was found that catalyst structures exhibited approximately identical selectivity, while octahedral Pd particles containing {111} facets demonstrated 1.5 times greater activity than cubic Pd particles containing {100} facets. The authors attributed this enhanced catalytic activity to both the morphology and dimensions of the nanoparticles.

The aforementioned examples illustrate the importance of a thorough knowledge of nanoparticle shape control as well as the average size, since both affect chemical reactivity. Nanocatalysis is a new area of rapid development in contrast to its bulk counterpart; the tailoring of catalysts at the nanoscale greatly enhances reactivity and selectivity.<sup>12,17,25,32,33</sup> However, the underlying origins of the distinct changes observed in catalytic reactivity are relatively unknown. The examination of nanoparticles and, in particular, nanoparticle clusters provides insight into physical and chemical properties as a function of size due to their natural bridge between atoms

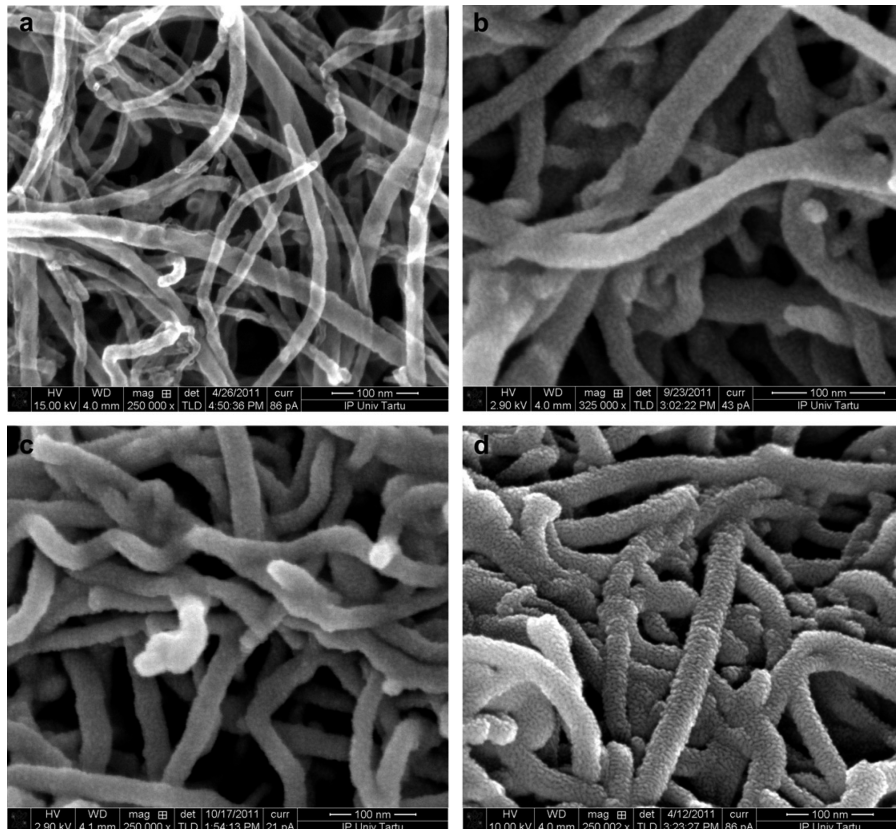


**Figure 2.** (a) Schematic illustration of how continuous growth on the {100} planes leads to the eventual transformation of a Pd cube bound by {100} facets into an octahedron, enclosed by {111} facets. (b–e) SEM images of the Pd polyhedrons obtained by controlling the volume of Na<sub>2</sub>PdCl<sub>4</sub> that is added to the reaction solution: (b) 5.8 mg, (c) 8.7 mg, (d) 17.4 mg, and (e) 29.0 mg. TEM images of the Pd polyhedrons are presented in the insets (scale bars 10 nm). (f) Maximum current densities of formic acid oxidation over Pd cubes, truncated cubes, cuboctahedrons, truncated octahedrons, and octahedrons enclosed by {111} and {100} facets in different proportions. The inset shows their corresponding peak potentials. Adapted with permission from ref 31. Copyright 2012 The Royal Society of Chemistry.

and molecules as well as the bulk limit.<sup>34</sup> It is surmised that the resulting enhancement of catalytic activity and selectivity for small nanoparticles is the product of several factors operating in parallel. For example, with decreases in nanoparticle size, the population of low-coordinated atoms available for interactions with chemical adsorbates increases. The distinct electronic properties of such sites are expected to play a role in chemical reactivity by facilitating the dissociation of reactants, or by stabilizing intermediate reaction species.<sup>25</sup> It is known that when Pd is enclosed by {100} facets, it exhibits higher catalytic activity than when it is enclosed by {111} facets in CO oxidation. Jin et al.<sup>35</sup> reported an approach for the size-controlled growth of Pd nanocubes and nanobars. The formed

**Table 1.** Nonexhaustive List of Common Palladium Support Materials

support material	Pd structure	applications	ref
carbon black	nanostructures, porous nanoparticles, nanoflowers, nanochain networks	DAFC, DFAFC, ORR, PEMFC	102, 125–127, 129, 132, 134, 146, 147, 165, 210, 242, 251, 280, 343–345
activated carbon (AC)	nanostructures	hydrogen storage, HOR, ORR	282, 292, 299, 346
carbon spheres	nanostructures	DAFC	128, 347
carbon nanofibers (CNFs)	nanostructures	biosensors, H <sub>2</sub> O <sub>2</sub> detection	293, 317, 320
SWCNTs	nanostructures	biosensors, gas sensor	135, 287
MWCNTs	nanostructures	biosensors, DFAFC, DAFC	131, 136, 141, 203, 287, 348–351
graphene/rGO	nanostructures	DFAFC, DAFC, hydrogen storage, ORR, biosensors	118, 143, 150, 178, 241, 289, 325, 326, 352
Ti	nanostructures, nanodendrites	DEFC, DFAFC	70, 82, 90
TiO <sub>2</sub>	thin film, nanoparticles	DFAFC	159, 345, 349
TiO <sub>2</sub> NTs	nanostructures, membrane	photooxidation of organics, PEMFC, hydrogen storage, DAFC	160, 161, 212, 290
Fe <sub>2</sub> O <sub>3</sub>	nanostructures	DAFC	353
MnO <sub>2</sub>	nanostructures	DFAFC, DMFC, Li ion battery	354, 355
V <sub>2</sub> O <sub>5</sub>	thin film	hydrogen sensor	356, 357
ZnO	nanostructures	CO oxidation	35

**Figure 3.** SEM images of uncoated (a) and Pd-coated (b–d) MWCNTs on GC electrodes. Nominal Pd film thickness: (b) 5, (c) 10, and (d) 15 nm (calculated per geometric area of GC). Reprinted with permission from ref 45. Copyright 2013 Elsevier.

Pd nanocubes/bars with variable sizes (e.g., 6, 10, and 18 nm) were dispersed onto ZnO nanowires and employed for size effect studies in the catalytic CO oxidation. The results demonstrated that decreasing the size of the Pd cubes/bars enhanced the conversion rate dramatically, with the maximum conversion temperature being strongly dependent on the size of the Pd nanomaterials. It is believed that this dependence on nanoparticle size may be attributed to factors such as structural and electronic effects, metal–support interactions, and the formation of active oxide layer species.<sup>33,35</sup> As noted in the

aforementioned examples, it is quite common for a supporting material to be utilized in catalysis. A further understanding of size effects may be facilitated by distinct nanoparticle–substrate interactions. Such interactions may be a combination of electronic (e.g., nanoparticle/support charge transfer) and/or structural (e.g., strain effects at the nanoparticle/support interface) effects.<sup>25</sup>

Nanoparticle supports play an important role in nanocatalysis and may serve to enhance chemical performance, but perhaps more importantly to stabilize supported nanoparticles. The

primary requirements for suitable support materials are a high surface area, good electrical and thermal conductivity, and high stability during electrochemical operation. Examples of common support materials and their applications are summarized in Table 1. The complex interactions between nanoscale catalysts and their supports may affect catalytic reactivity in several different ways: (i) by maximizing or enhancing useful lifetimes, (ii) by changing the structure and morphology of the nanoparticles, (iii) by means of charge transfer to or from nanoparticles, (iv) through the provision of additional reaction sites, and (v) by stabilizing intermediate reactive species.<sup>25</sup>

Significant progress toward the development of synthetic techniques for the fabrication of nanostructured materials with controllable morphologies and dimensions has been made over the past decade. Continued research will be required to elucidate the inherent interactions between catalysts and supporting materials and the further development of complex nanocatalysts. Further technological advancements will be achieved through the capacity to synthesize and organize matter into controlled geometries at the nanoscale.

## 2.2. Physical Synthesis Techniques

Physical synthesis techniques involve the use of metal precursors that are not chemically changed, but rather undergo molecular rearrangements where no new substances are created, nor chemical bonds cleaved or forged. Pd and Pd-based nanomaterials synthesized by this technique include nanoscale films, nanoparticles, nanowires, and nanorods. This broad range of fabrication techniques includes sputtering,<sup>36–51</sup> ion or electron beam deposition,<sup>49,52–57</sup> and laser ablation.<sup>58–66</sup>

Sputtering methods allow for the fabrication of nanostructures such as thin film catalysts, nanoparticles, and bimetallic Pd-based nanomaterials with controlled cluster size and dispersion.<sup>37,46</sup> The controlled synthesis of Pd nanomaterials with sputtering methods enables the minimization of the total required amount of metal catalyst, as illustrated by Sarto et al.,<sup>46</sup> who fabricated various Pd catalysts via direct current (dc) magnetron sputtering deposition. The substrates were placed within a vacuum chamber and sputtered under the following conditions: Ar atmosphere pressure of  $1.2 \times 10^{-2}$  mbar, 45 mA current control, sputtering rate of  $0.40 \pm 0.05$  nm/s, and a Pd 99.98% foil ( $\phi = 54$  mm) target. The thickness of the formed thin film was time controlled, allowing for the Pd loads to be effectively monitored. In work by Jukk et al.,<sup>45</sup> Pd nanoparticles were deposited onto multiwalled carbon nanotubes (MWCNTs) by means of a magnetron sputtering procedure. The various Pd loadings correlated to film thicknesses of 0, 5, 10, and 15 nm may be seen in Figure 3; the uniform distribution demonstrates the facile use of magnetron sputtering as an effective method for decorating MWCNTs with Pd nanoparticles.

Ion- and electron-beam-induced deposition (IBID and EBID) methods are attractive for their unique ability to fabricate three-dimensional structures in a single step. Both IBID and EBID allow for morphologies, dimensions, and interparticle distances to be tailored by high-energy focused beams, ions, and electrons, respectively.<sup>54,55,57</sup> They are both vacuum-based techniques, and their deposition processes are fairly similar, as illustrated in Figure 4. The precursor materials are introduced via an injection system, allowing them to be adsorbed onto the substrate. A focused beam then stimulates the decomposition of the precursor materials to produce the

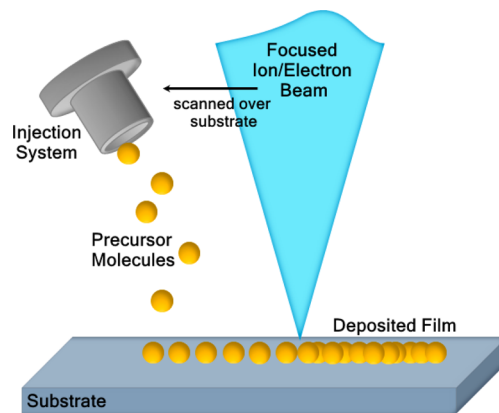


**Figure 4.** Schematic representation of focused electron/ion-beam-induced deposition techniques.

desired nanostructures. Barzola-Quiquia et al.<sup>55</sup> employed IBID (FEI NanoLab XT 200 dual-beam microscope (DBM)) to synthesize Pd-based nanowires that exhibited nonmetallic behavior due to their low metallic content, where palladium bis(hexafluoroacetylacetone) was used as the precursor. The synthesis conditions included an operating energy of 30 kV, a  $\text{Ga}^+$  ion beam, a 10 pA current, and a precursor temperature of 36 °C. The nominal dimensions of the nanowires to be produced were set in the DBM at 250 nm (width) × 200 nm (thickness). The formed Pd nanowires were polycrystalline in structure, and had a high carbon content.

The advantages of EBID over IBID are its capacity to create smaller features, with less amorphization and without ion implantation, such as  $\text{Ga}^+$ .<sup>54</sup> Bhuvana et al.<sup>56</sup> produced highly conductive Pd nanopatterns utilizing palladium hexadecanethiolate, which served as a negative-tone direct-write electron resist. A Nova NanoSEM 600 instrument from FEI Co. was employed for the procedure. A palladium hexadecanethiolate film (~60 nm) was spin coated onto a Si substrate and patterned using a 5 kV electron beam at  $135 \mu\text{C}/\text{cm}^2$ . The regions exposed to the electron beam remained on the substrate subsequent to being developed in toluene for 10 s. Following the post-treatment of the Pd nanowires at 230 °C in ambient air, metal lines with low (<10%) carbon content were obtained.

The laser ablation method possesses several advantages, including simplicity of preparation, weak agglomeration, and the capacity for the production of multicomponent nanoparticles.<sup>58–69</sup> The laser ablation process involves the directed deposition of a vaporized plasma by laser radiation (of particular energy fluence) on a target. Various Pd plasmas were investigated by Torrisi et al.,<sup>69</sup> which were produced at different laser ablation wavelengths. A Q-switched Nd:YAG laser irradiated a Pd target placed under vacuum, using 1064 nm (fundamental) and 532 nm (second harmonic) wavelengths, both at an intensity of approximately  $10^9 \text{ W/cm}^2$ . The pulse duration was 3 ns, which was set at a single shot (1–10 Hz repetition) rate mode. At 1064 nm, the laser pulse energy was varied over the 1–300 mJ range; when the wavelength (532 nm) was selected, the pulse energy was altered to between 1 and 150 mJ. The laser beam was focused through a convergent lens, at an optimal focalization distance of 50 cm on a polished 2  $\text{cm}^2$  Pd sheet target, which was introduced into a vacuum chamber ( $10^{-6}$  mbar). To ensure that each laser pulse would impact a flat fresh surface, the target was moved

vertically with the vacuum feedthrough. The results demonstrated that, in terms of ablation yield vs laser fluence, IR irradiation was more efficient for the ablation process in comparison to visible light irradiation. However, the 532 nm wavelength appeared to be more effective than the fundamental wavelength in terms of plasma equivalent temperature, equivalent acceleration voltage, and mean charge state.

In recent years, the laser ablation of bulk Pd targets in liquids has been proven to be an efficient technique in the generation of Pd nanomaterials.<sup>58,59,61–63,65–67</sup> The chief advantage of this approach is that liquids allow for the production of stably dispersed nanoparticles, toward the generation of ultrapure colloidal nanoparticle solutions.<sup>67</sup> However, for laser ablation synthesis in liquids, the nanoparticle dimensions and morphologies are primarily contingent on several experimental parameters, encompassing the type of solvent, as well as the laser-related fluence, wavelength, and ablation times.<sup>61</sup> An example of this was provided in the work of Semaltianos et al.,<sup>67</sup> who synthesized Pd-based nanoparticles via the laser ablation of bulk Pd in deionized water (DIW), acetone, and ethanol. The laser ablation of the generated nanoparticles was carried out using a 12 ps pulsed laser source at a beam wavelength of 532 nm. A high pulse repetition rate laser beam (200, 80, or 10 kHz) with an average power of 2.6 or 1.6 W was employed to ensure high ablation efficiency. A bulk portion of Pd metal (purity 99.999%) served as the target, and ablation was carried out with the target positioned at the bottom of a Pyrex Petri dish, which was filled each time with DIW, acetone, or ethanol. The beam was scanned onto a stationary sample in circular spiral motions ( $\phi = 3$  mm, pitch 0.006 mm, scanning speed 25 mm/s, 10 overscans) by means of a computer-controlled scanning galvo head (SGLV). Each ablation cycle was carried out for 8.4 min to produce  $\sim 0.7$  mg of nanoparticles. Transmission electron microscopy (TEM) images of the final products are depicted in Figure 5a–c, revealing that all three liquids produce spherical and solid nanoparticles. Variations from the median diameter were observed among the samples, where the Pd nanoparticles obtained in acetone and ethanol were more diminutive (e.g., 1.1 and 1.5 nm) in comparison to those formed in DIW (3.3 nm). Furthermore, X-ray photoelectron spectroscopy (XPS) results (Figure 5d–f) revealed the presence of peaks corresponding to Pd metal and Pd present in different oxidation states. Moreover, the spectral region of energies above 345 eV revealed the presence of a weak band centered at approximately 346.6 eV for the nanoparticles generated in DIW, accounting for the presence of empty d states, slightly above the Fermi level. The absence of this band from the spectra of the nanoparticles synthesized in acetone or ethanol indicated the formation of  $\text{PdH}_x$  nanoparticles through the laser ablation of the bulk Pd target. This study highlighted the feasibility and importance of the laser ablation method for the synthesis of Pd nanoparticles with desirable morphological and structural properties.

Sputtering, ion or electron beam deposition, and laser ablation have been utilized to synthesize a variety of Pd nanomaterials with unique properties and morphologies. Through the alteration of the synthesis parameters, reagent concentrations, and presence of stabilizing surfactants, physical production techniques may be employed to achieve the synthesis of Pd-based nanomaterials with controlled compositions, morphologies, and other attributes.

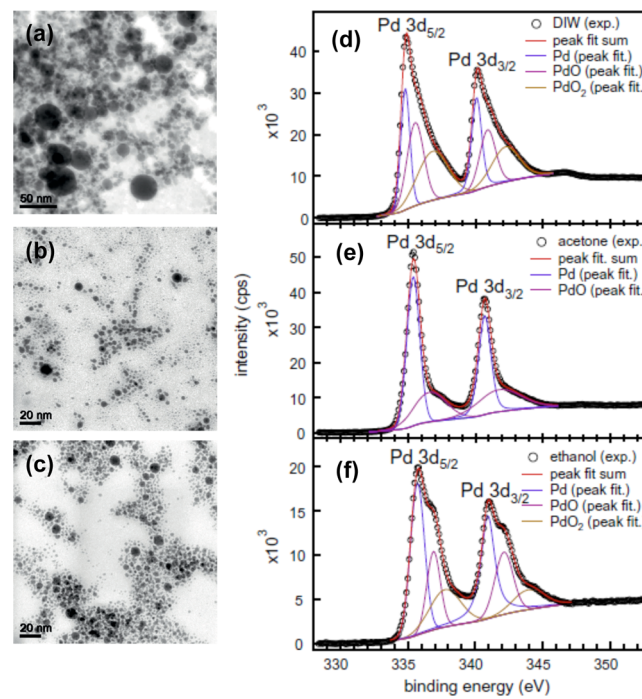


**Figure 5.** TEM images of nanoparticles synthesized in DIW (a), acetone (b), and ethanol (c). XPS spectra of the corresponding nanoparticles synthesized in DIW (d), acetone (e), and ethanol (f). Adapted with permission from ref 67. Copyright 2013 Elsevier.

### 2.3. Hydrothermal Methods

The hydrothermal method comprises a low-cost, facile, and templateless approach for the synthesis of Pd and Pd-based nanomaterials.<sup>70–84</sup> By adjusting parameters such as temperature, pressure, and precursor concentration, the characteristics of the crystalline phase and particle size may be altered. The hydrothermal method is generally based on a chemical reaction that occurs within a solvent at temperatures above the solvent boiling point, and under pressures exceeding 1 bar. This technique takes into consideration the fundamental properties of water, exploiting increases in temperature and pressure to alter its capacity as a solvent. The hydrothermal method allows for many advantages over other conventional and nonconventional synthesis techniques, with the most prevalent being a one-step approach that can produce a wide variety of nanostructures. The majority of Pd and Pd-based nanomaterials fabricated by the hydrothermal process utilize  $\text{PdCl}_2$  as the Pd precursor.<sup>70–73,75,77,79,81,83</sup> Adams et al.<sup>72</sup> prepared PdCd nanostructures, which were grown directly on titanium plates using a facile hydrothermal reduction method. Etched Ti substrates were introduced into Teflon-lined autoclaves, along with the following: 5 mM  $\text{PdCl}_2$ , 5 mM  $\text{Cd}(\text{NO}_3)_2 \cdot 4\text{H}_2\text{O}$ , and 1 M ammonium formate up to a volume of 10 mL. Varied quantities of the  $\text{Cd}(\text{NO}_3)_2 \cdot 4\text{H}_2\text{O}$  precursor were added to obtain the desired Pd:Cd ratio. The autoclaves were heated at 180 °C for 2 h, and once cooled, the PdCd-coated plates were annealed at 250 °C for 2 h in a tube furnace under an argon flow to ensure good surface adhesion of the PdCd thin film. The resulting nanomaterials formed alloyed PdCd dendritic structures (Figure 6a–c). Dendritic growth is believed to be driven by the competition between associated crystal structure symmetries and morphological instabilities arising from a nonlinear diffusion process.<sup>85</sup> The Cd nanoparticles were considered as foreign impurities, which acted as instabilities that

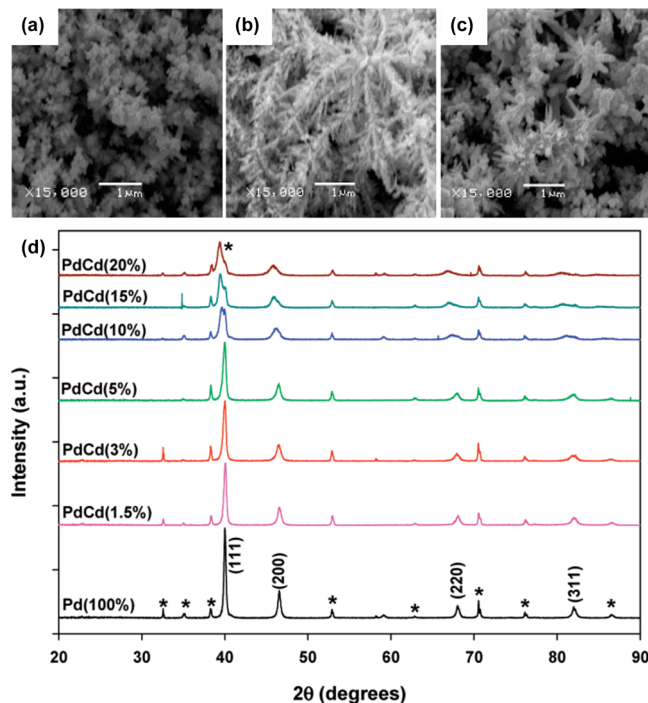


**Figure 6.** SEM images at 15000 $\times$  magnification of Pd–Cd surfaces with normalized atomic ratios of Pd to Cd of 100:0 (a), 95:5 (b), and 85:15 (c). Corresponding XRD patterns of the prepared PdCd films follow in (d). The diffraction peaks belonging to the Ti substrate are labeled with an asterisk. Adapted from ref 71. Copyright 2009 American Chemical Society.

initiated changes in the nucleation and growth rate. As well,  $\text{HCOO}^-$  served as both a reducing and a capping agent that dictated growth orientation.<sup>85,86</sup> X-ray diffraction (XRD) identified the internal crystalline structures of the prepared PdCd nanomaterials (Figure 6d), revealing that, as more Cd was added, all of the diffraction peaks were slightly shifted to smaller  $2\theta$  values, indicating increased  $d$  spacing and a dilation of the lattice constant. Recently, Adams et al.<sup>87</sup> fabricated Pd-based catalysts using the hydrothermal reduction of  $\text{PdCl}_2$ ,  $\text{H}_2\text{PtCl}_6 \cdot 6\text{H}_2\text{O}$ ,  $\text{IrCl}_3 \cdot 3\text{H}_2\text{O}$ ,  $\text{Pb}(\text{NO}_3)_2$ , and  $\text{Cd}(\text{NO}_3)_2 \cdot 4\text{H}_2\text{O}$  precursors. In all cases, the  $\text{PdCl}_2$  precursor and reducing agent were kept constant at 5.0 mM and 1.0 M, respectively. To obtain the desired compositions, the stoichiometric quantity of Pd:M was maintained at a ratio of 90:10. The autoclaves were heated at 180 °C for 2 h. The prepared Pd-based catalysts (Figure 7) showed negligible morphologic differences upon the addition of 10 atom % Pt, Ir, Cd, and Pb, with the exception of Cd, which initiated the formation of small dendritic structures. The other catalysts exhibited a random array of nanoporous structures with a particle size distribution that ranged from ~10 to ~200 nm.

The most common reducing agents used in the hydrothermal synthesis of Pd and Pd-based nanomaterials are ammonium formate (AF),<sup>71,72,75,81</sup> formaldehyde ( $\text{CH}_2\text{O}$ ),<sup>70,78,82</sup> and ethylene glycol (EG).<sup>78,83,84</sup> As depicted in Figure 8, bimetallic PdCu nanoparticles (NPs) dispersed on a three-dimensional graphene (GE) hydrogel were synthesized by Yuan et al.<sup>83</sup> via the hydrothermal method, utilizing EG as the reducing agent. A modified Hummers method involved the preparation of graphene oxide (GO),  $\text{PdCl}_2$ ,  $\text{CuSO}_4 \cdot 5\text{H}_2\text{O}$ , glutamate, and EG, which were combined and sealed within a stainless-steel autoclave and maintained at 100 °C for 3 h. Once cooled,

as-prepared samples were rinsed with distilled water and freeze-dried overnight. The PdCu/GE hydrogels shown in Figure 8a exhibited an interconnected, porous 3D framework with Pd and Cu nanoparticles uniformly dispersed on both sides of the GE sheets, as well as encapsulated within the GE layers. In Figure 8b, TEM characterization confirmed the uniform distribution of the PdCu nanoparticles on the GE. Lattice fringe distances of 0.208 and 0.225 nm were ascribed to the (111) lattice spacing of fcc Cu and fcc Pd (Figure 8c). Overall, the hydrothermal method allowed for the production of bimetallic PdCu catalysts with good dispersion and encapsulation on 3D framework GE sheets with a high surface area. As relates to reducing agents, Yi et al.<sup>78</sup> conducted a detailed study of the hydrothermal preparation of porous Pd catalysts using different reduction agents in the absence and presence of EDTA (ethylenediaminetetraacetic acid). The reducing agents employed included polyethylene glycol (PEG),  $\text{CH}_2\text{O}$ , and EG. A typical synthesis procedure involved the introduction of etched Ti sheets into an autoclave that contained 10 mL of  $\text{PdCl}_2$ , a reducing agent, and EDTA. The autoclave was subsequently heated at 180 °C for 10 h. Once cooled to room temperature, the samples were air-dried at 100 °C for 30 min, and then rinsed with pure water. The dimensions of the Pd nanoparticles ranged from 70 to 220 nm. Among the three reducing agents investigated, EG was revealed to be superior for the formation of small-sized Pd nanoparticles.

As of late, poly(vinylpyrrolidone) (PVP) has emerged as a promising candidate for the production of nanocrystals<sup>73</sup> and bimetallic core–shell nanostructures<sup>74</sup> via the hydrothermal method. Kuai et al.<sup>74</sup> described a one-pot hydrothermal co-reduction synthesis of Au–Pd core–shell nanostructures, using PVP under a controlled reducing process. The preparation of the Au–Pd core–shell nanoparticles began with the addition 0.2 g of PVP to 10 mL of 0.7 mM  $\text{HAuCl}_4$  and 0.9 mM  $\text{H}_2\text{PdCl}_4$  mixtures under vigorous stirring. Subsequently, 5 mL of 2.8%  $\text{NH}_3 \cdot \text{H}_2\text{O}$  was added and the resulting solution stirred for 10 min. The solution was then transferred into a 25 mL Teflon-lined stainless-steel autoclave for 12 h at 180 °C. Once cooled to room temperature, the as-prepared nanoparticles were collected by centrifuge and rinsed with deionized water and absolute ethanol. The resulting nanoparticle size was ~300 nm, with the Au core and Pd shell thicknesses averaging 180 and 60 nm, respectively. Figure 9a displays the growth process of the typical core–shell nanostructures after 4 h at 180 °C. The formation of the core–shell nanoparticles (Figure 9b) was dependent on the reducing capacity of PVP, which is relatively low, making the reduction of Pd(II) more difficult than that of Au(III). Correspondingly,  $\text{HAuCl}_4$  was initially reduced by PVP followed by  $\text{H}_2\text{PdCl}_4$  to naturally form the core–shell structure.

Not only is hydrothermal synthesis a simple single-step process that minimizes waste, it also enables the ability to exploit the properties of solvents and the selection of nontoxic reducing agents, which places the hydrothermal method among other promising “green” synthesis techniques. A highly active and durable nanocomposite consisting of carbon nanotubes (CNTs), reduced graphene oxide (rGO), and Pd nanoparticles was synthesized by Zhang et al.<sup>80</sup> For their synthesis, 4 mL of 10 mM  $\text{H}_2\text{PdCl}_4$  was added to a dispersion of 30 g of MWCNTs (10–20 nm  $\varnothing \times$  10–30  $\mu\text{m}$  long) and 2 mg·mL<sup>-1</sup> (30 mL) of homogeneous GO, and maintained in an ice bath under sonication for approximately 30 min. The resulting 3D CNT–rGO hydrogel possessed a large surface area and abundant volume with a hierarchically porous structure. The

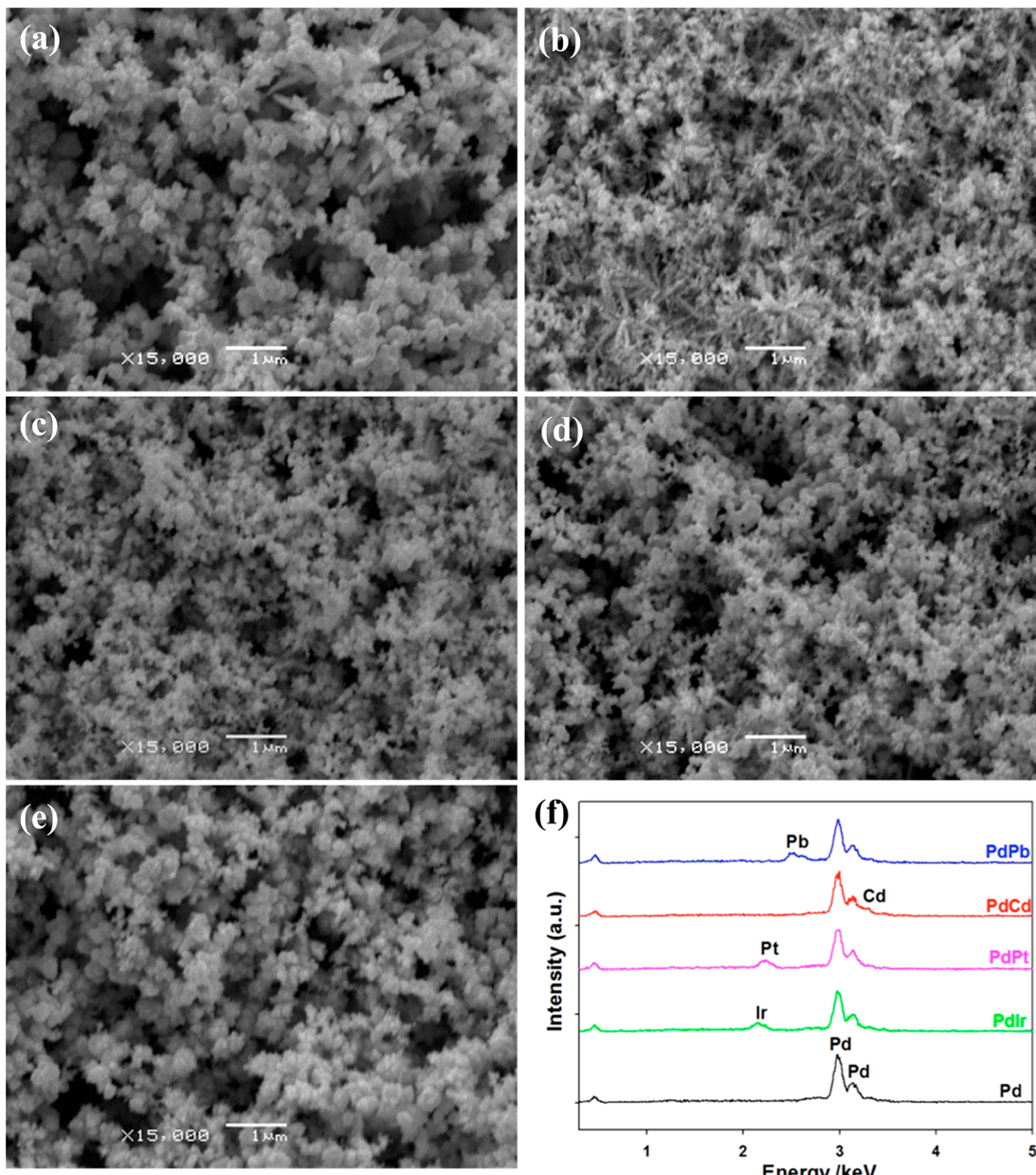


**Figure 7.** SEM images of the electrode surfaces at 15000 $\times$  magnification: (a) Pd, (b) PdCd, (c) PdIr, (d) PdPb, and (e) PdPt. The EDX spectra of all the catalysts are shown in (f). Reprinted from ref 81. Copyright 2014 American Chemical Society.

precursor solution was then sealed within a 50 mL Teflon-lined autoclave and held at 180 °C for 12 h. Following cooling, the final product was a black gel-like 3D cylinder. By adjusting the volume of the GO aqueous dispersion, the dimensions of the hydrogel could be freely altered. This self-assembled hydrogel exhibited remarkably high and stable catalytic activity for the degradation of pollutants.

The hydrothermal method is a useful technique for the creation of a variety of Pd-based nanomaterials. This one-step synthesis technique allows for the compositions and morphologies of Pd and Pd-based materials to be easily altered through the manipulation of precursors, pH, and reaction temperature. Potential nanostructures include nanoparticles,<sup>73–77,80,81,83</sup> nanodendrites,<sup>71,72,81</sup> core–shell nanoparticles,<sup>74,78</sup> nanocubes,<sup>84</sup> tetrapods,<sup>82</sup> and nanoporous networks,<sup>70,78</sup> all of which may be supported on various substrate materials. The potential for mass production of Pd-based

nanostructured materials, while maintaining good control over their composition, makes this technique a viable option for the development of Pd-based catalysts for electrochemical applications.

#### 2.4. Electrochemical Deposition

Electrodeposition is a simple, rapid, and inexpensive method for the preparation of nanoparticles, as well as nanowires and nanorods.<sup>37,38,46,87–115</sup> The electrodeposition process involves the use of a two- or three-electrode cell system, where the electrolyte generally serves as the source of Pd as well as the conductive medium. By controlling the potential or current density of an electrochemical cell, deposition occurs from an oxidized form in solution to a metallic state at the surface. There are a variety of electrodeposition techniques that may be employed for the fabrication of Pd and Pd-based nanomaterials, such as cyclic voltammetry (CV),<sup>38,88,95,96,106</sup> square-wave

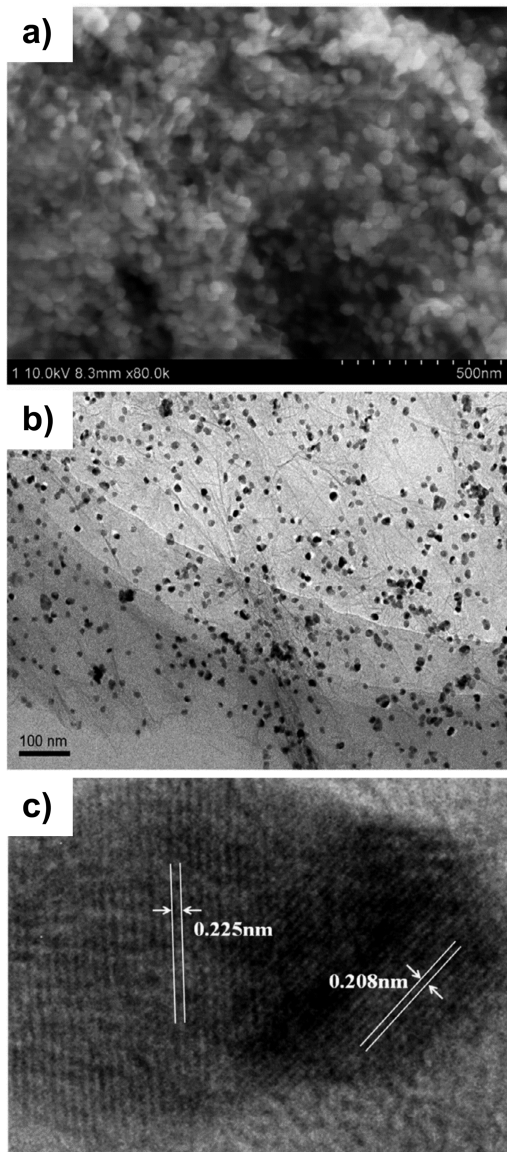


**Figure 8.** (a) Scanning electron microscopy image of (a)  $\text{Pd}_{66}\text{Cu}_{34}$ /GE hydrogel. (b) Transmission electron microscopy and (c) high-resolution TEM images of PdCu NPs on a GE sheet. Adapted with permission from ref 83. Copyright 2013 Elsevier.

voltammetry,<sup>116, 117</sup> chronoamperometry (CA),<sup>89–94, 97–100, 102–105, 109–112, 118</sup> chronopotentiometry (CP),<sup>46, 87, 107, 114</sup> chronocoulometry (CC),<sup>101</sup> and pulsed electrodeposition<sup>108</sup> at a fixed or varied potential.

Potentiostatic control methods (e.g., CA) are widely utilized for the fabrication of Pd and Pd-based nanomaterials. For example, Xiao et al.<sup>100</sup> electrochemically deposited Pd onto a Au rotating disk electrode (RDE) ( $\phi = 5$  mm, Pine Research Instruments) at a fixed potential of  $-0.2$  V with a rotation rate of 1600 rpm in a deaerated 0.1 M NaCl solution, which contained varied concentrations of  $\text{PdCl}_2$ , between  $10^{-4}$  and  $10^{-5}$  M. A Pd sheet served as the counter electrode, whereas Ag/AgCl (0.1 M NaCl) served as the reference electrode. The morphologies of the obtained Pd electrodes were strongly dependent on the precursor concentration, producing Pd nanorods (Figure 10) and Pd nanoparticles in  $3 \times 10^{-4}$  M  $\text{PdCl}_2$  and  $10^{-5}$  M  $\text{PdCl}_2$ , respectively. For the deposition of identical quantities of Pd, the deposition times were adjusted to

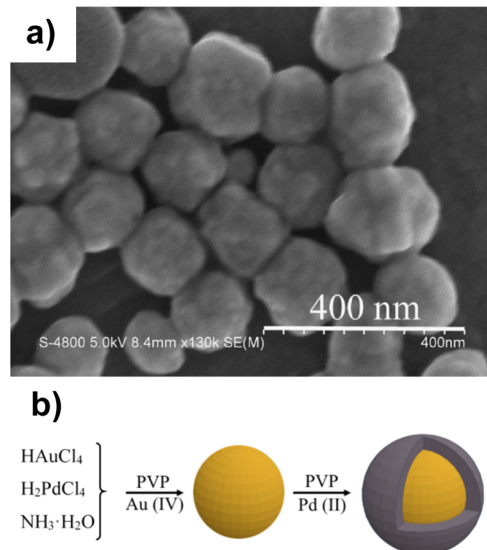


**Figure 9.** (a) Obtained products with a 1 h reaction time at  $180$  °C. (b) Formation process of Au–Pd core–shell and alloy bimetallic nanostructures. Adapted from ref 74. Copyright 2012 American Chemical Society.

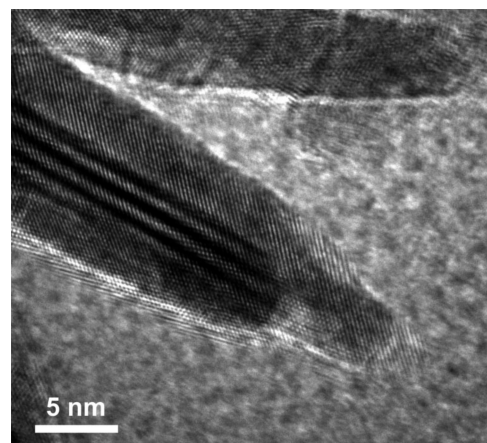


**Figure 10.** TEM image of a Pd NR deposited on carbon powder, in which two or three overlapping single-crystal Pd NRs with a clear rod shape may be resolved. Reprinted from ref 100. Copyright 2009 American Chemical Society.

achieve the same coulometric charge. The diameters of the Pd nanoparticles ranged from 5 to 10 nm, while the Pd nanorods were uniform in shape with a diameter of  $\sim 5$  nm. The unusual nanorod form that was obtained by this simple electrodeposition process exhibited superior activity in oxygen reduction reaction. This was not due to bulk effects, such as lattice strain, but rather could be ascribed to the morphologic peculiarity of the exposed Pd(110) facets of the Pd nanorods (NRs) themselves.

Cyclic voltammetry is often employed as an additional method for the preparation of Pd and Pd-based nanomaterials. Zhao et al.<sup>106</sup> electrochemically deposited dendritic Pd nanoarchitectures on single-crystal n-GaN(0001) via CV. A standard three-electrode cell arrangement was used, with n-GaN as the working electrode, Pt wire ( $\phi = 1$  mm) as the counter electrode, and a Ag/AgCl reference electrode. Pd catalysts were prepared on n-GaN using one, three, five, and seven cycles in a solution of 17.7 mg of  $\text{PdCl}_2$  dissolved in 20

mL of 0.1 M HCl. Figure 11 depicts the typical cyclic voltammograms of n-GaN(0001) in 0.1 M HCl and 0.1 M HCl

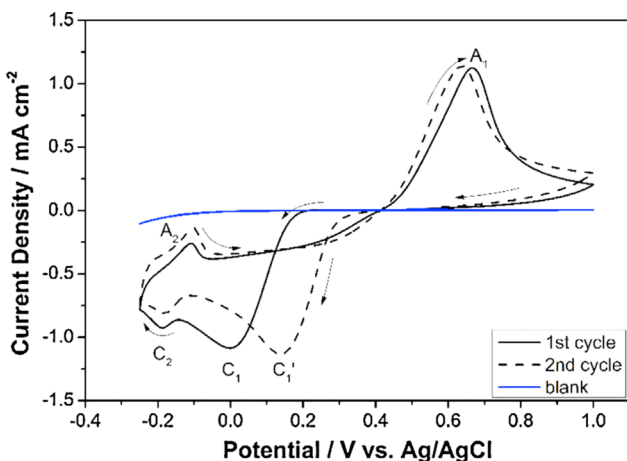


**Figure 11.** Cyclic voltammograms of n-GaN(0001) in 0.1 M HCl (blue line) and 0.1 M HCl + 5 mM  $\text{PdCl}_2$  (black solid and dashed lines) at a scan rate of  $20 \text{ mV s}^{-1}$ . Reprinted with permission from ref 106. Copyright 2014 Elsevier.

+ 5 mM  $\text{PdCl}_2$ . In the presence of  $\text{PdCl}_2$  (black line), Pd electrocatalysis occurred as indicated by the presence of an obvious cathodic peak  $C_1$  at 0.0 V, which was attributed to the direct reduction of  $\text{Pd}^{2+}$  to  $\text{Pd}^0$ . Peak  $A_1$ , observed at  $\sim 0.66$  V, was the anodic oxidation peak, showing a typical quasi-reversible process. The cathode peak  $C_2$  at  $-0.19$  V and the anodic peak  $A_2$  at  $-0.10$  V were the result of the adsorption and desorption of hydrogen on Pd, respectively.

Galvanostatic techniques (i.e., CP) for electrodeposition are carried out by means of a constant current. Porous tubular Pd nanostructures were produced by Bai et al.<sup>107</sup> with an applied current density of  $0.4 \text{ mA cm}^{-2}$  for 10 h, where a three-electrode cell was used in conjunction with an electrolyte, which consisted of  $1.5 \text{ g L}^{-1} \text{ H}_2\text{PdCl}_4$  and  $25 \text{ g L}^{-1} \text{ H}_2\text{BO}_3$ , with a pH of 6.5–7.0. The morphology of the Pd nanostructures was obtained through the use of a CdS-modified porous anodic alumina (PAA) membrane template.

The control of two primary modes of particle evolution, namely, nucleation and growth, is central in the creation of shape-controlled nanoparticles. Limiting the growth of nucleation, which may be accomplished by controlling the current/voltage, or by altering the electrolyte conditions, may yield shape-controlled nanoparticles.<sup>102,111,112</sup> Sun and co-workers electrochemically prepared Pd tetrahedahedral nanocrystals and 5-fold twinned nanorods with high-index facets using the square-wave potential technique.<sup>116,117</sup> The electrochemical preparation of nanorods was carried out in a standard three-electrode cell with a platinum foil counter electrode and a saturated calomel electrode (SCE) at room temperature. As shown in Figure 12,<sup>117</sup> the Pd nanorods were electrodeposited onto the glassy carbon (GC) substrate in a 5 mM  $\text{PdCl}_2$  + 0.1 M  $\text{HClO}_4$  solution using the square-wave potential method at 100 Hz for 20 min, where the lower potential ( $E_L$ ) was set at  $-0.15$  V and the upper potential ( $E_U$ ) potential was fixed at  $0.65$  V. The average diameter measured at the middle portion of the nanorods was  $\sim 190$  nm, whereas the average length was  $\sim 2.0$  mm. A high-magnification scanning electron microscopy (SEM) image (Figure 12b,c) revealed that the formed Pd nanorods were highly faceted and possessed a pentagonal cross

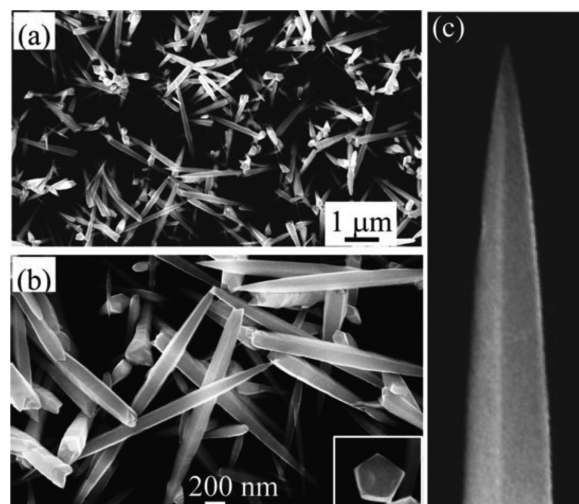


**Figure 12.** (a) Low- and (b) high-magnification SEM images of Pd nanorods (type I) prepared at  $E_L = -0.15$  V and  $E_U = 0.65$  V. The inset in (b) shows the pentagonal projection of a Pd nanorod. (c) SEM image of a tip of a Pd nanorod. Reprinted with permission from ref 117. Copyright 2009 Royal Society of Chemistry.

section (inset in Figure 12b). The electrodeposited Pd nanorods exhibited high catalytic activity toward the electro-oxidation of ethanol due to the presence of high-index facets. For the production of tetrahedahedral nanocrystals, Sun et al.<sup>116</sup> employed a similar step electrodeposition technique; however, Pd nanocrystals were electrodeposited directly onto a GC electrode in a 0.2 mM  $\text{PdCl}_2$  + 0.1 M  $\text{HClO}_4$  solution at a potential step from  $+1.20$  V (vs SCE) to  $-0.10$  V for 20 ms to generate nuclei. The Pd nuclei were then grown into tetrahedahedral nanocrystals through the application of a square-wave potential of 100 Hz with lower and upper potential limits of 0.30 and 0.70 V, respectively. The resulting tetrahedahedral Pd nanocrystals were enclosed by {730} high-index facets and exhibited high catalytic activity toward the oxidation of ethanol in alkaline media. Comparably, Meng et al.<sup>111</sup> synthesized Pd nanothorns on carbon paper using a two-step potential square-wave electrodeposition process. The initial step involved the growth of the nuclei (electronucleation step) followed by crystal growth (electrochemical growth step). The nanothorns were fabricated on a  $1 \text{ cm}^2$  segment of round carbon paper (working electrode) in a three-electrode cell system that contained 2 mM  $\text{K}_2\text{PdCl}_6$  in a 0.5 M  $\text{H}_2\text{SO}_4$  solution. The counter electrode consisted of Pt foil, and the reference electrode was an SCE. The initial deposition steps  $E_1$ ,  $E_2$ ,  $T_1$ , and  $T_2$  were 0.8 V,  $-0.7$  V, 0.05 s, and 0.02 s, respectively, and the number of square waves was 600. The second steps  $E_1$ ,  $E_2$ ,  $T_1$ , and  $T_2$  were 0.6 V, 0.25 V, 0.005 s, and 0.005 s, respectively, and the number of square waves was 18000. The resulting Pd nanothorns, depicted in Figure 13, were  $\sim 1 \mu\text{m}$  in length, with the smallest diameter of 2 nm at the tip. These Pd nanothorns were comprised of fcc crystals with a growth orientation of {220}.

An additional technique for achieving the desired morphologies and/or crystallography of electrodeposited Pd nanomaterials is through template-assisted growth. Template-assisted growth may be performed by chemical or physical means to produce geometries such as nanowires or nanorods. Chemically assisted templating involves the use of chemical species in the deposition bath that are capable of directing material growth

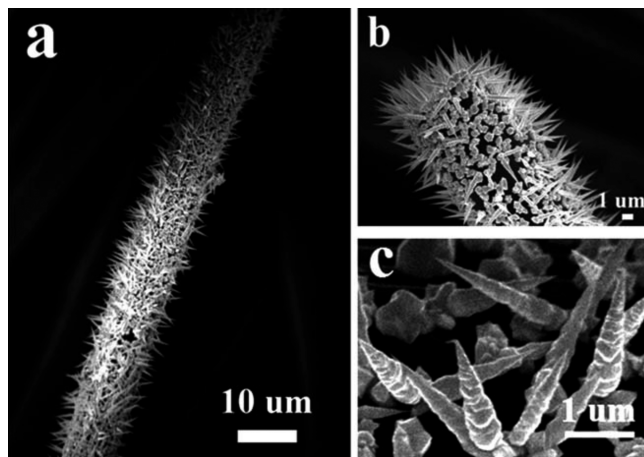


**Figure 13.** SEM micrographs of Pd-nanothorn-covered carbon paper fibers. Reprinted with permission from ref 111. Copyright 2011 Royal Society of Chemistry.

and therefore properties such as shape and/or crystallography.<sup>113</sup> More commonly, as relates to Pd template-assisted growth, physical templates serve as molds that specifically define where nucleation and growth may occur. Physical templates serve to alter the diffusion layer, and therefore the reduction kinetics, for the electrodeposition process, and following physical template-assisted growth, the template is removed.<sup>93,104,105,107,109,114</sup> The most common method of physical templating is the use of anodized aluminum oxide (AAO) templates. The AAO membrane possesses a uniform and parallel porous structure that may be readily controlled through the monitoring of the preparation conditions, which makes it ideal for the creation of highly ordered nanowire arrays.<sup>93,104,105,109</sup> Although not as widely utilized, PAA membranes are well recognized for their capacity to produce 1D metal nanostructures. As aforementioned, Bai et al.<sup>107</sup> reported the facile synthesis of porous tubular Pd nanostructures via the electrodeposition of Pd into a CdS-modified PAA template.

With regard to the growth of nanowire arrays, electrodeposition comprises one of the most efficient methods. Wang et al.<sup>93</sup> fabricated Pd nanowire arrays by a template-electrodeposition method using an AAO template. Porous AAO templates with an average pore diameter of 80 nm (Figure 14a) were fabricated via a two-step anodization method on high-purity aluminum foils. A small amount of silver glue was used to affix a section of AAO film onto a polished glassy carbon electrode (GCE). To prepare the Pd nanowires, electrodeposition was carried out in an aqueous solution of  $0.5 \text{ g}\cdot\text{L}^{-1}$   $\text{Pd}(\text{NH}_3)_4\text{Cl}_2$  and  $0.8 \text{ g}\cdot\text{L}^{-1}$   $\text{Na}_2\text{EDTA}$ . Under constant stirring, a potential of  $-0.6 \text{ V}$  was applied for 40 min. To ensure the complete removal of the AAO template, the Pd nanowire arrays were dipped into 2 M NaOH for 1 h and rinsed several times with distilled water. Figure 14b,c shows typical SEM images of the Pd nanowire arrays once the AAO template was completely dissolved. The inset in Figure 14b displays the energy-dispersive X-ray (EDX) analysis of the Pd nanowire arrays. The major peaks correspond to Pd, further confirming the complete removal of the AAO template. The resulting ordered Pd nanowire arrays were uniform in diameter with lengths of 80 and 800 nm, respectively.

In work by Cui et al.,<sup>104</sup> unsupported PdAu bimetallic nanoparticle heterostructured tubes (BHTs) with 50–100

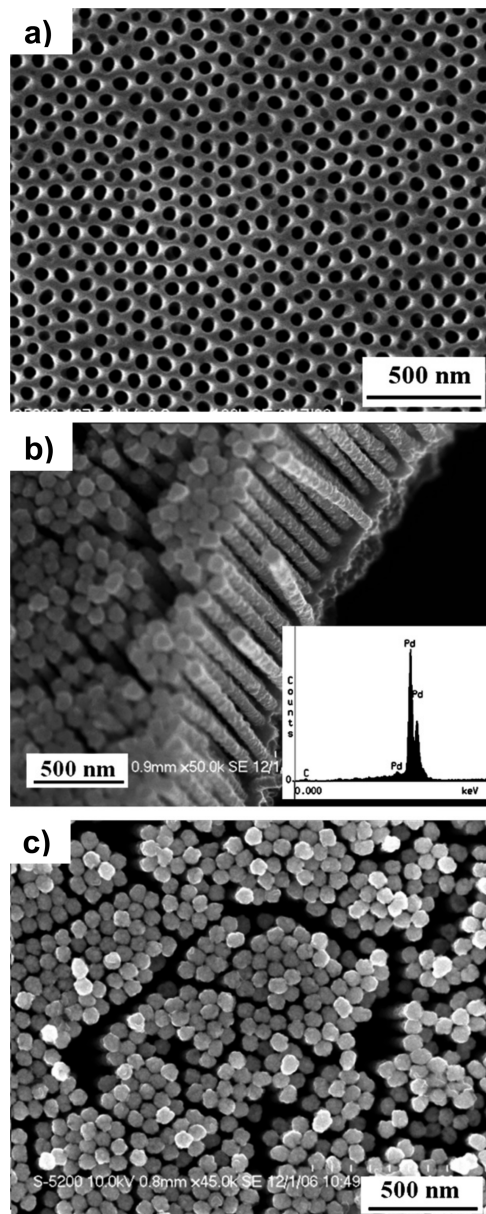


**Figure 14.** SEM images of (a) AAO and (b, c) Pd nanowire arrays (the inset in (b) is the EDX analysis of Pd nanowire arrays). Adapted with permission from ref 93. Copyright 2007 Elsevier.

atom % Pd were synthesized by a one-step electrodeposition route. The PdAu BHTs (Figure 15) were grown on a commercially available AAO template (Anodisc 47, Whatman Co., United Kingdom) with a channel diameter of  $\sim 300 \text{ nm}$ , sputtered with a thin ( $\sim 40 \text{ nm}$ ) layer of Au. This thin layer of Au was employed as the working electrode for the subsequent electrodeposition of the desired PdAu BHTs. The PdAu BHTs were produced by potentiostatic deposition at  $-1.3$  to  $-1.6 \text{ V}$  vs Ag/AgCl (3 M) in 100 mM  $\text{NaNO}_3$  with anhydrous dimethyl sulfoxide (DMSO) solvent mixed with 10 mM  $\text{PdCl}_2$  and different concentrations of  $\text{AuCl}_3\cdot\text{HCl}\cdot 4\text{H}_2\text{O}$  as the supporting electrolyte. Subsequent to electrodeposition, the AAO template was removed by immersing the PdAu BHTs in a 1.0 M NaOH solution for 1 h, followed by multiple rinsing with doubly deionized water and ethanol. The tubular length was controlled by the reaction time, with the maximum length

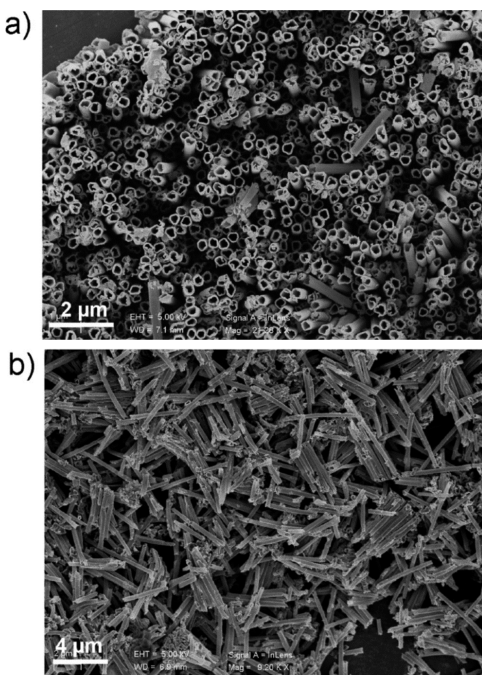


**Figure 15.** SEM images reveal the tubular (a) and well-dispersed (b) features. The well-dispersed unsupported Pd–Au BHTs were obtained under ultrasound treatment following the complete removal of the AAO template with NaOH (1.0 M). Reprinted from ref 104. Copyright 2011 American Chemical Society.

being determined by the length of the template channel. The resulting PdAu BHTs had an average diameter of  $\sim 300$  nm.

The morphologies of nanomaterials influence their chemical and physical properties, which has created a demand for more structurally complex nanomaterials. Recently, electrodeposition followed by chemical etching has been proposed as a means of creating coiled nanosprings or lattices.<sup>109,115</sup> Liu et al.<sup>109</sup> reported on the successful fabrication of Pd nanosprings with tunable diameters and lengths (Figure 16). The experiments were performed in a solution containing 25 mM  $\text{PdCl}_2$ , 20 mM  $\text{CuCl}_2 \cdot 2\text{H}_2\text{O}$ , and 0.1 M HCl with an applied potential of  $-0.1$  V (vs Ag/AgCl). The electrochemical cell consisted of an AAO

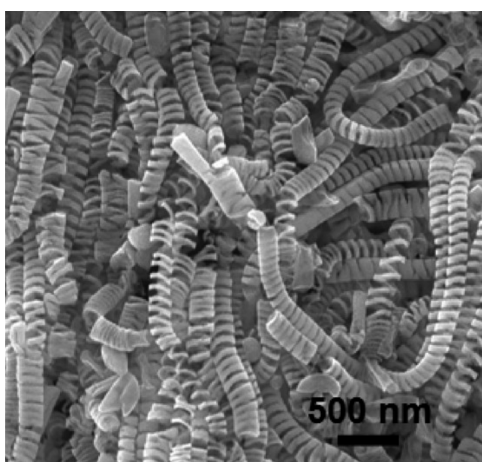


**Figure 16.** SEM image of a large quantity of Pd nanosprings synthesized using the  $\sim 250$  nm nanochannels of a commercial AAO template. Reprinted from ref 109. Copyright 2011 American Chemical Society.

disk, which was sandwiched between a section of glassy carbon and an O-ring, assembled in a Teflon cell. Au nanoparticles were employed as glue to attach the custom-made AAO template to the glassy carbon substrate. The solution was then cast into the electrochemical cell where the applied potential simultaneously reduced Cu and Pd ions on the predeposited bottom Au cathode to produce the nanorods. Using 30% (volume ratio) nitric acid, the Cu was etched away from the PdCu nanorods to reveal Pd nanosprings. The nanosprings were removed from the AAO template through immersion in 3 M NaOH for 20 min followed by copious rinsing with deionized water. Differences in the nanospring diameters (as can be seen in Figure 16) were caused by the nonhomogeneous nanochannel diameters of the AAO template. The inner diameters and wire diameters of the Pd nanosprings were estimated to be between 60 and 130 nm for the larger samples and between 25 and 30 nm for the smaller samples, respectively. It was experimentally confirmed that the concentrations of Pd and Cu ions within the nanochannels were a key factor in the synthesis of the Pd nanosprings. The mechanism of nanospring growth was believed to be the result of a failure to construct an effective depletion layer. The Pd atoms were able to grow along the walls of the nanochannels, while the Cu atoms were not. This allowed for the accumulation of nucleated Pd clusters and their growth into grains in close proximity to the walls of the AAO template.

The advantages of electrodeposition include high particle purity, greater control over dimensions through the use of templates, lower particle size distribution, and increased control over distribution densities. The use of electrochemical deposition methods has broadened the variety of nanoscale metals with interesting geometries through facile synthesis conditions that may be easily tuned. Not only can electrodeposition be performed over a much shorter timeline than other available methods, it is also considered a green, simple, and inexpensive method for the preparation of nanometric materials. The advantages described above make electrochemical deposition techniques ideal for a diverse range of applications, as well as for industrial production and large-scale synthesis.

## 2.5. Chemical Reductions and Other Methods

Various other methods such as electroless deposition, micro-emulsions, and photochemical synthesis have been employed to synthesize Pd and Pd-based nanoparticles, nanocrystals, nanocubes, nanospheres, nanowires, nanodendrites, nanorods, and nanotubes. These synthesis methods typically involve the use of a photoreductant or chemical reducing agents or the presence of a stabilizer to generate the desired results.

Among the most frequently utilized deposition methods, electroless deposition remains a straightforward and efficient method for the production of a wide variety of nanostructures. Electroless deposition is a purely chemical process that involves the deposition of solid-phase coatings or metallic powders, alloys, or compounds from aqueous or nonaqueous solutions without an external current source.<sup>119</sup> Electroless deposition may be categorized as being of two primary types: displacement deposition<sup>120–124</sup> and autocatalytic deposition.<sup>18,85,91,125–152</sup>

Displacement deposition (also referred to as galvanic replacement) is reliant on the reduction potential of metallic precursors. For example, in work done by Qiu et al., bimetallic Pd–Fe thin films were prepared using a galvanic replacement reaction between  $\text{PdCl}_4^{2-}/\text{Pd}$  and  $\text{Fe}^{2+}/\text{Fe}$ , with

standard redox potentials (vs SHE (standard hydrogen electrode)) of 0.95 and  $-0.44$  V, respectively. The thin films were prepared by placing  $25\ \mu\text{L}$  of a  $10\ \text{mM}$  acidic  $\text{H}_2\text{PdCl}_2$  precursor onto prepared Fe thin films for 30 min, followed by thorough rinsing with ultrapure water. Similarly, Lu et al.<sup>121</sup> fabricated PdAg nanotubes (NTs), denoted as PdAg-25 (Figure 17), via a galvanic replacement technique. To synthesize PdAg-

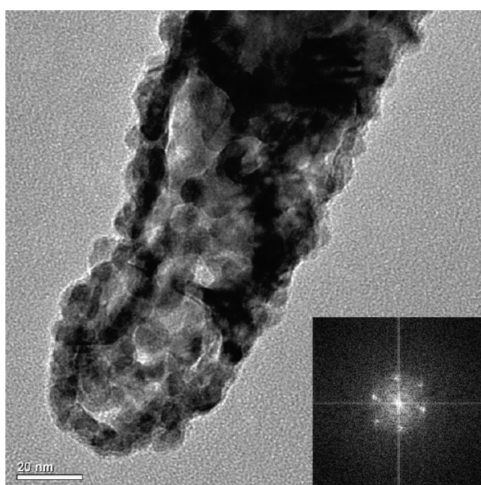


**Figure 17.** HRTEM images of PdAg-25 nanotubes. The inset depicts the corresponding two-dimensional fast Fourier transform (FFT) pattern. Adapted from ref 121. Copyright 2010 American Chemical Society.

25 nanotubes, 5 mg of prepared Ag nanorods was dispersed in  $\sim 10\ \text{mL}$  of pure water under magnetic stirring. Subsequently, 2 mg of  $\text{PdCl}_2$  dissolved in 10 mL of water was added in sequential drops and the resulting solution allowed to stir for 30 min. The final products were dried and stored under vacuum at room temperature. Figure 17 displays a high-resolution transmission electron microscopy (HRTEM) image of the resulting nanotubes, which were decorated with Pd nanocrystals, having dimensions of 5–8 nm. This simple reduction method may be employed to generate a diverse range of metallic nanostructures under the restriction of a required favorable difference in the reduction potentials of the two metals. Although galvanic replacement offers a facile and versatile route for the synthesis of a variety of nanostructures, it is limited by the reaction that proceeds exclusively at the surface of the less noble metal, which acts as a reducing agent.<sup>119,124</sup>

Autocatalytic deposition proceeds by means of chemical reducing agents, including, but not limited to, ascorbic acid, citric acid, sodium borohydride, and ethylene glycol. The nature of the reducing agent may heavily impact the deposition kinetics, which can, in turn, alter the morphological and physicochemical surface properties. Lim et al.<sup>18</sup> investigated the nature of reducing agents to create Pt branches that emerged from a Pd nanocrystal core. Uniform, truncated octahedral Pd nanocrystal cores were synthesized by reducing  $\text{Na}_2\text{PdCl}_4$  in an aqueous solution, and heating PVP, L-ascorbic acid, and citric acid to  $100\ ^\circ\text{C}$  under magnetic stirring for 3 h. A TEM image of the as-prepared Pd nanocrystals (NCs) is shown in Figure 18A, which reveals truncated octahedral shapes with an average size of 9.1 nm. An HRTEM image of a single Pd nanocrystal (Figure 18B) indicated a crystal surface enclosed by eight {111} and six {100} facets. As relates to the synthesis of the Pd–Pt

nanodendrites, 1 mL of the as-prepared Pd nanocrystals was suspended in an aqueous solution (6 mL) containing PVP and ascorbic acid. In a three-necked flask, the aqueous suspension was heated to  $90\ ^\circ\text{C}$  in ambient air under magnetic stirring. An aqueous solution of  $\text{K}_2\text{PtCl}_4$  (in deionized water) was rapidly injected into the flask and heated at  $90\ ^\circ\text{C}$  for 3 h. Once cooled to room temperature, the product was collected by centrifugation and rinsed several times with pure water. TEM images of the product (Figure 18C,D) revealed that a number of Pt branches grew from the Pd core into dendritic tendrils, with the Pd–Pt nanodendrites averaging 23.5 nm in size. The dendritic growth of Pt branches was believed to be attributed to the high rate of Pt reduction as mediated by an autocatalytic process in the presence of L-ascorbic acid, which was enhanced by the multiple nucleation sites provided by truncated octahedral Pd seeds.

As noted in the example above, parameters influencing the reaction rate such as temperature, pressure, solution concentrations, and complexing agents may be easily altered to achieve differing properties. To assemble Pd nanocubes enclosed by {100} planes,<sup>149</sup>  $500\ \mu\text{L}$  of a  $0.01\ \text{M}$   $\text{H}_2\text{PdCl}_4$  aqueous solution was added to 10 mL of a  $1.25 \times 10^{-2}\ \text{M}$  hexadecyltrimethylammonium bromide (CTAB) solution at a fixed temperature of  $95\ ^\circ\text{C}$ . Under continuous stirring, 0.1 M ascorbic acid was gradually introduced into the mixture to obtain a dark brown slurry. Figure 19 shows a TEM image of the cubic nanoparticles, with a mean edge length of  $\sim 27.2$  nm. For comparative purposes, Ye et al.<sup>149</sup> produced Pd nanoparticles using the same synthesis method as above, while substituting  $\text{NaBH}_4$  for ascorbic acid as the reducing agent. In comparison to ascorbic acid, the relatively more robust reducing power of  $\text{NaBH}_4$  plausibly increased the rate of nucleation and particle growth, which led to the formation of nanoparticles, rather than nanocubes. As well, CTAB and  $\text{Br}^-$  ions have been noted to preferentially block {100} facets of Pd to promote the formation of Pd{100} planes. With the slow growth process initiated by ascorbic acid, CTAB and  $\text{Br}^-$  may engulf the Pd{100} plane to thus produce Pd nanocubes. The rapid particle growth rate using  $\text{NaBH}_4$  interrupted any adequate adsorption of CTAB or  $\text{Br}^-$  onto the Pd{100} plane, which resulted in the formation of Pd nanoparticles.

Sodium borohydride is a commonly used reducing agent for autocatalytic deposition.<sup>127–136,138,139,141,143,146,147,149</sup> Nanoparticles composed of Pd, Pt, and PdPt supported on  $\text{HNO}_3$ -treated carbon black were prepared by Adams et al.<sup>143</sup> using a room temperature  $\text{NaBH}_4$  impregnation method. The metal precursors ( $\text{PdCl}_2$  and  $\text{H}_2\text{PtCl}_6$ ), water, and carbon were appropriately combined to obtain a coating load percentage of 20 wt % metal in all cases, and sonicated for 20 min. The pH of the solution was adjusted to between 9.5 and 10 using 0.5 M NaOH, and the solution was stirred for 5 min. This was followed by the dropwise addition of 20 mL of 0.125 M  $\text{NaBH}_4$  under continuous stirring, after which the solution was left to react for 1 h before being centrifuged and rinsed with pure water. The resulting catalysts (Figure 20) were dried in an oven at  $60\ ^\circ\text{C}$  for 12 h to reveal particle size distributions from 2.5 to 4.0 nm, from 1.5 to 8.5 nm, and from 1 to 12 nm for  $\text{Pd}_{0.25}\text{Pt}_{0.75}$ , Pt, and Pd, respectively.

In contrast to galvanic deposition, autocatalytic deposition proceeds at the surface and bulk of the metals, which allows for greater control of the properties of the final end product. Polyol synthesis (the synthesis of metal-containing compounds in polyethylene glycols) employs ethylene glycol, which serves as

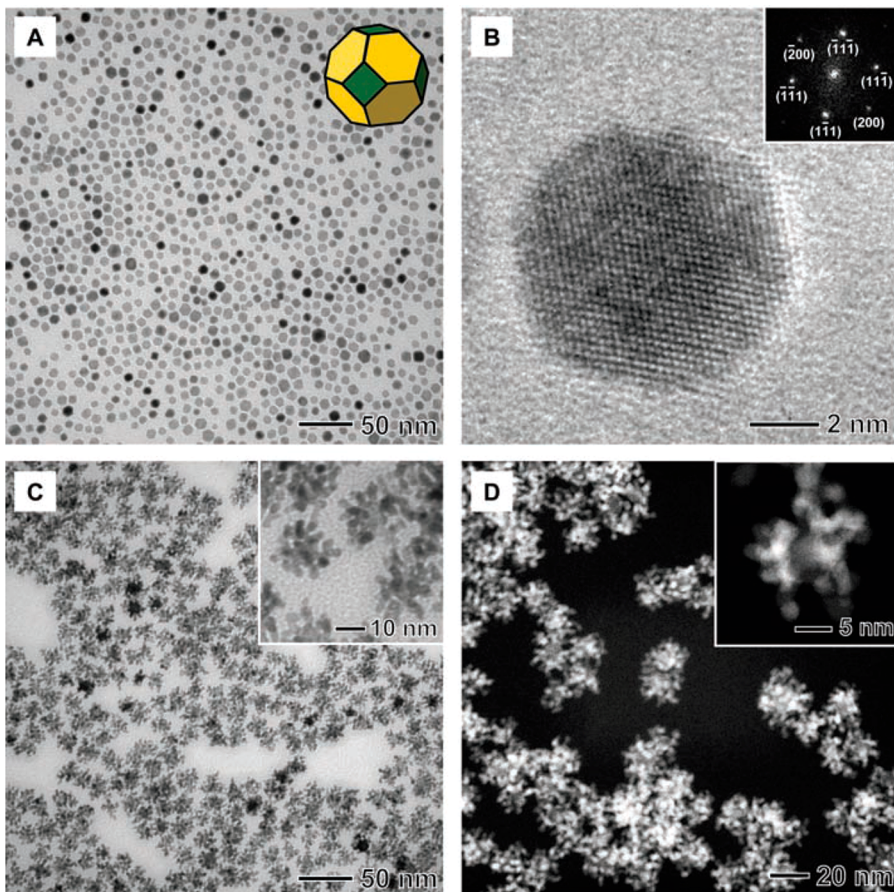


**Figure 18.** (A) TEM image of truncated octahedral Pd NCs synthesized by reducing  $\text{Na}_2\text{PdCl}_4$  with L-ascorbic acid in an aqueous solution. The inset shows a geometrical model of the truncated octahedron, where green and yellow denote the  $\{100\}$  and  $\{111\}$  facets, respectively. (B) HRTEM image of a single truncated octahedron of Pd recorded along the  $[011]$  zone axis and the corresponding FT pattern (inset). (C) TEM image of Pd–Pt nanodendrites synthesized by reducing  $\text{K}_2\text{PtCl}_4$  with L-ascorbic acid in the presence of truncated octahedral Pd NC seeds in an aqueous solution. (D) HAADF-STEM image of Pd–Pt nanodendrites. Reprinted with permission from ref 18. Copyright 2009 American Association for the Advancement of Science.

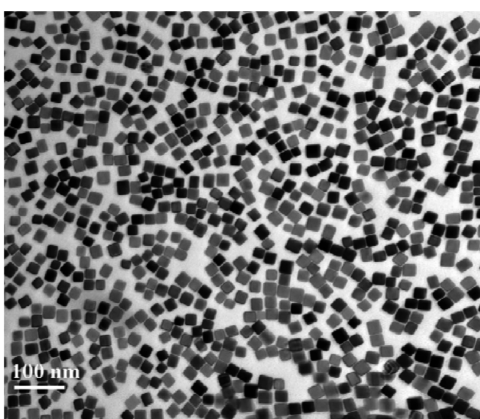


**Figure 19.** TEM image of nanocubes. Reprinted with permission from ref 149. Copyright 2015 Elsevier.

both the solvent and reducing agent. A study designed by Wang et al.<sup>151</sup> was inspired by the variable outcomes of a polyol synthesis, which typically involves the reduction of sodium tetrachloropalladate(II) ( $\text{Na}_2\text{PdCl}_4$ ) by EG or diethylene glycol (DEG) in the presence of PVP. In a typical procedure, 30 mg of PVP and 2 mL of EG or DEG were introduced into a glass vial and heated to the desired temperature (140 °C for single-

crystal, truncated octahedral and multiply twinned icosahedral Pd in EG and DEG; 75 °C for stacking fault-lined nanoplates in DEG) in an oil bath under magnetic stirring. An injection of 15 mg of dissolved  $\text{Na}_2\text{PdCl}_4$  in 1 mL of 60 °C EG or DEG was quickly introduced into the glass vial and allowed to react for the required time (3 or 30 h). This work showed that Pd nanocrystals with distinct dual structures and shapes might be synthesized by simply manipulating the reduction rate through the use of different polyols and temperatures. In other work by Wang et al.,<sup>152</sup> polyol synthesis was utilized to obtain ultrathin wavy Pd nanowires without the use of a template, which aimed to study the relationship between the reaction kinetics and the tendency of attachment by using Pd as a model system. A colloidal stabilizer, PVP, and  $(\text{CF}_3\text{COO})_2\text{Pd}$  precursor were dissolved separately in DEG. The  $(\text{CF}_3\text{COO})_2\text{Pd}$  solution was then rapidly injected into the PVP solution at 140 °C under magnetic stirring, and they were allowed to react for 3 h, producing nanowires with  $2.0 \pm 0.06$  nm in width and tens to hundreds of nanometers in length. The success of this nanowire synthesis was contingent on the use of a suitable precursor material. When  $\text{Na}_2\text{PdCl}_4$  was substituted for  $(\text{CF}_3\text{COO})_2\text{Pd}$ , the nucleation and growth of Pd polyhedrons took place. Figure 21 summarizes how the precursor-determined reaction kinetics affected the nucleation, growth, attachment, and final morphology of the Pd nanostructures during polyol synthesis.

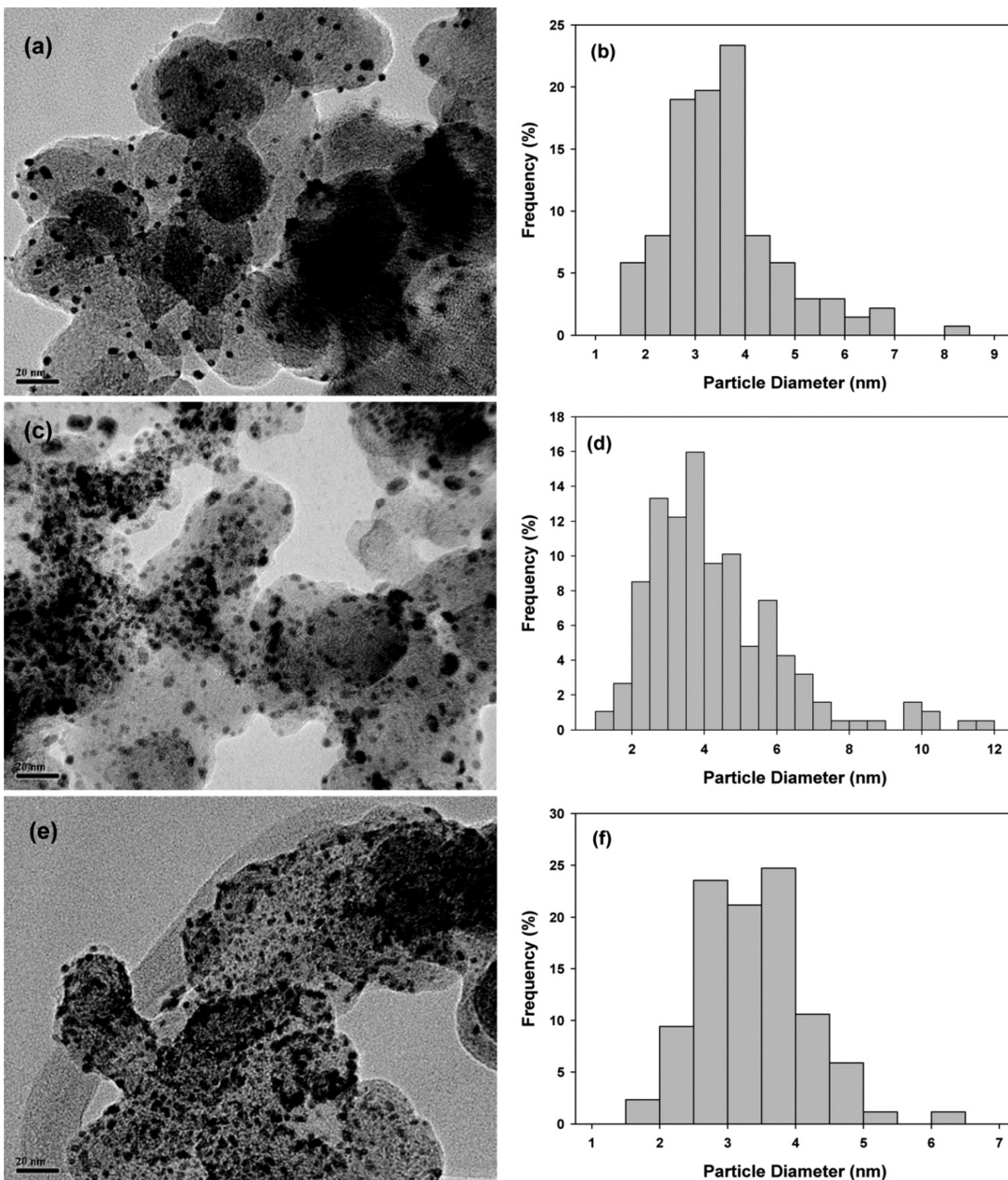


**Figure 20.** Typical TEM images of the prepared carbon-supported catalysts with the corresponding particle size histograms: (a, b) Pt/C, (c, d) Pd/C, and (e, f) Pd<sub>0.25</sub>Pt<sub>0.75</sub>/C. Reprinted with permission from ref 143. Copyright 2011 The Electrochemical Society.

(CF<sub>3</sub>COO)<sub>2</sub>Pd (top trace) allowed for a rapid reduction rate, generating diminutive clusters of Pd nuclei. Due to the consumption of essentially all of the precursors, the Pd nuclei grew into relatively small Pd nanoparticles, which in turn tended to adhere to each other to form wavy nanowires. In comparison, the use of Na<sub>2</sub>PdCl<sub>4</sub> (bottom trace) as the precursor initiated a relatively slow reaction rate, which allowed the nucleation and particle growth to proceed over a longer period of time. This caused the continuous deposition of Pd onto the Pd seeds, thus showing that attachment-based growth was promoted via the manipulation of the reaction kinetics during nucleation.

Microemulsion techniques (water-in-oil microemulsions) have the ability to easily control the particle size by varying the synthesis conditions. Acting as an attractive approach in the preparation of multimetallic alloy compositions with a high

degree of homogeneity, surfactant-stabilized reverse micelles serve as microreactors and as steric stabilizers to inhibit particle growth.<sup>127,153,154</sup> Raghubeer et al.<sup>127</sup> synthesized Pd–Co–Au/C catalysts by the reverse microemulsion method with enhanced degrees of alloying at lower temperatures, while maintaining small particle sizes and large surface areas, in contrast to the conventional borohydride method. Sodium diethylsulfosuccinate (AOT) served as the surfactant, while heptane acted as the oil phase. The catalysts were prepared through two microemulsion stages. Microemulsion I was carried out by mixing ammonium hexachloropalladate, cobalt nitrate, dihydrogen tetrachloraurate, AOT, deionized water, and heptane under continuous stirring, followed by 20 min of ultrasonication. Microemulsion II was achieved by mixing sodium borohydride, AOT, deionized water, and heptane under constant stirring followed by ultrasonication for 20 min, where

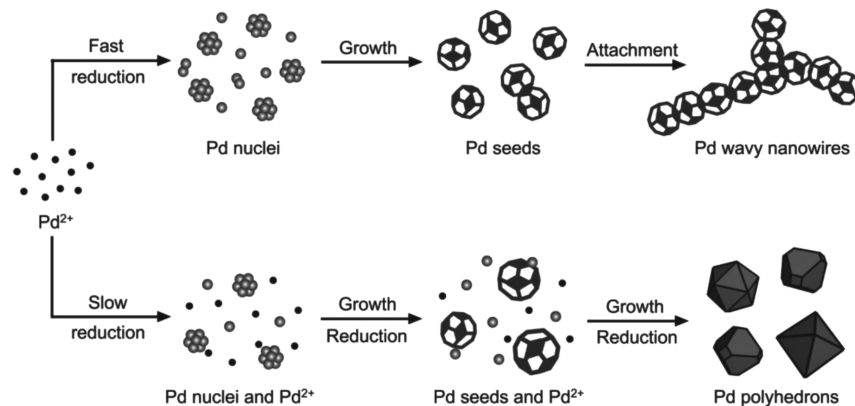


**Figure 21.** Schematic illustration of how the reaction kinetics (as mediated by a precursor) affects the nucleation, growth, and attachment and thus the final morphology of Pd nanostructures in the polyol synthesis. Reprinted with permission from ref 152. Copyright 2013 Wiley-VCH Verlag GmbH & Co.

the molar ratio of water to AOT was maintained at 10:1. Microemulsions I and II were subsequently combined and ultrasonicated for 2 h, after which the appropriate volume of carbon (Vulcan XC 72R) was introduced into the mixture to give a metal:C weight ratio of 20:80. The resulting slurry was continually stirred for 2 h, filtered, rinsed with acetone and deionized water, and then dried in an oven for 2 h at 100 °C. The as-synthesized Pd–Co–Au/C catalysts were subjected to various types of heat treatment and examined for their properties. The higher degree of alloying at lower temperatures, as well as the enhanced chemical homogeneity through the microemulsion method (compared to that obtained by the conventional borohydride method), had the capacity to augment catalytic activity in electrochemical applications.

Ultrathin Pd nanosheets are newly emerging synthesized materials. Siril et al.<sup>155</sup> prepared hexagonal Pd nanosheets using an emulsion made of water, oil, surfactant (CTAB), and a cosurfactant (toluene). The resulting nanosheets consisted of single overlapped and slightly disoriented monocrystals. Furthermore, Pd nanosheets have also been successfully fabricated using CO as a surface-confining agent to control the morphology of the Pd nanocrystals.<sup>156–158</sup> The surface-energy-controlled growth in the formation of Pd nanosheets by CO was facilitated by the strong binding of CO on Pd(111).<sup>157,158</sup> CO surface confinement was employed in work by Huang et al.<sup>157</sup> to prepare corolla-like Pd mesocrystals consisting of ultrathin (1.8 nm thick) Pd nanosheets. The ultrathin Pd sheets possessed the unique properties of a well-defined surface plasmon resonance absorption feature in the near-infrared region, a high electrochemically active surface area, and a photothermal effect in response to a near-infrared region laser.

Photochemical deposition offers a simple and cost-effective method for the creation of ultrathin films and nanoparticles.<sup>159–162</sup> TiO<sub>2</sub>-nanotube-supported PdAu nanoparticles were successfully prepared by Tian et al.<sup>160</sup> via photoassisted deposition. A pregrown TiO<sub>2</sub> nanotube plate was immersed in a solution that contained the appropriate amounts of 0.04 M Pd and Au precursors [Pd(NO<sub>3</sub>)<sub>2</sub> and AuCl<sub>3</sub>], as well as 5 mL of 50% (v/v) methanol. The solution was exposed to UV radiation for 30 min, after which the resulting stable PdAu nanoparticles were easily synthesized to reveal ~20 nm alloyed structures. The ease of the controlled synthesis of multimetallic Pd-based materials was contingent on the variation in reduction potentials of the desired metals. Large differences in the

reduction potentials limited the desired control, making fine-tuning an area of concern for some multimetallic catalysts.

Other methods, such as electroless deposition, microemulsions, and photochemical synthesis, offer the potential to manipulate the morphologies of Pd and Pd-based nanomaterials. The synthesis conditions, reagent concentrations, presence of stabilizers, and precursor selectivity may be employed to control or tune the resulting products through the manipulation of reaction rates and/or nucleation.

### 3. ELECTROCHEMICAL APPLICATIONS OF PD AND PD-BASED NANOMATERIALS

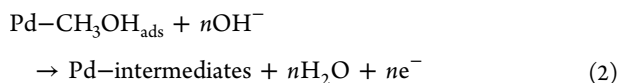
#### 3.1. Direct Alcohol Fuel Cells

The current interest in fuel cell technologies continues to flourish due to their potential for the elimination of unwanted environmental contaminants. Direct alcohol fuel cells (DAFCs) have garnered much attention for their use as power sources for portable applications, such as electronic devices and electric cars. Alcohols, such as methanol,<sup>39,136,141,145,150,163–169</sup> ethanol,<sup>90,93,129,134,136,137,150,170–178</sup> ethylene glycol,<sup>5,133,179,180</sup> and glycerol,<sup>5,133</sup> are appealing as a result of their high energy density, ease of transportation, and storage, in contrast to H<sub>2</sub>-fueled polymer electrolyte membrane fuel cells (PEMFCs). For decades, Pt-based electrodes have been dominant for their use as electrocatalysts in the oxidation of alcohols. However, the high cost, limited supply, and slow kinetics of alcohol oxidation on Pt have sparked notable efforts toward the design of new catalytic structures for DAFCs that contain little or no platinum. Pd-based nanomaterials have emerged as an attractive replacement for Pt in DAFCs, exhibiting higher activity and improved steady-state behavior than Pt over a large assortment of substrates in alkaline media.

**3.1.1. Electrochemical Oxidation of Methanol.** Direct methanol fuel cells (DMFCs) comprise the most common DAFCs, which boast the advantages of high energy conversion efficiencies, system simplicity, low pollution, and environmental compatibility. Considering that widely used Pt-based catalysts suffer from reduced efficiency due to poor anode kinetics, methanol crossover, and CO adsorbate poisoning, materials based on other metals such as Pd have been investigated to improve kinetics and to mitigate CO poisoning. The most significant challenge for DMFCs, much like for other fuel cells, is the development of active, robust, and low-cost electrocatalysts. Although remarkable progress has already been made

with respect to power density and fuel efficiency, improved methanol oxidation catalysis at the anode and the reduction of the methanol crossover effect remain as two primary aspects that require further improvement.<sup>168</sup>

It is well recognized that Pd is completely inactive for the electrooxidation of methanol in acidic solutions.<sup>181</sup> Interestingly, methanol may be completely oxidized at Pd in alkaline media according to the following proposed mechanism:<sup>5,179,182–187</sup>



where the intermediates of methanol oxidation are organic species such as  $-\text{CH}_3\text{O}_{\text{ads}}$ ,  $-\text{CH}_2\text{O}_{\text{ads}}$ ,  $-\text{CHO}_{\text{ads}}$ ,  $-\text{CO}_{\text{ads}}$ ,  $-\text{COOH}$ , etc., which can be dissociated from the Pd surface sites by  $\text{OH}^-$  species, with the ideal final products being  $\text{H}_2\text{O}$  and  $\text{CO}_2$ . According to the proposed mechanism, the final step may involve the poisoning of the Pd surface with CO species, which inhibits catalytic activity toward the methanol oxidation reaction (MOR). Additional surface chemical reactions may be employed to remove surface-adsorbed species and to regenerate the Pd metal.<sup>182,185</sup>

The activity of pure Pd in comparison to platinum is remarkably lower for methanol oxidation in alkaline media. However, the MOR activity may be enhanced by the presence of a second or third metal, binary and ternary metal compounds, developed in the form of Pd alloys and Pd overlayer structures. Combinations such as PdAg, PdAu, PdCu, PdNi, PdPt, etc.<sup>99,118,141,145,164,165,183–185,188–195</sup> have been reported with properties that mimic or rival those of the leading Pt-based materials. The tuning of Pd reactivity via modifications with inexpensive metals is based on the d-band theory, which states that the trend of reactivity follows d-band center values of overlayer and impurity atoms. When metals of varying lattice constants (small vs large) are overlaid or alloyed, the d-band center shifts up, and vice versa, which subsequently affects the reaction rate. The shift up of the d-band center creates a stronger capacity for the metal to adsorb, leading to the enhanced electrooxidation of alcohol at the surface of metals.<sup>196–198</sup> Under the presumption of the d-band effect, Wang et al.<sup>165</sup> produced Pd–Ag/C and Pd–Ag/CNT catalysts through the reduction of  $\text{NaBH}_4$ , which exhibited heightened performance over Pd/C toward methanol oxidation, with more negative onset potentials, enhanced CO tolerance, and increased stability. In addition to the increased kinetics, the second metal (Ag) acted under the bifunctional mechanism to activate water at lower potentials, which may oxidize adsorbed CO or other poisoning species, thereby liberating the Pd active sites.

The electrooxidation of methanol in alkaline media on bimetallic PdAu nanoparticles was investigated by Yin et al.<sup>188</sup> using an emulsion-assisted synthetic strategy to produce unique Pd-rich shell and Au-rich core PdAu nanoparticles. The measured compositions of the PdAu nanoparticles were  $\text{Pd}_{30}\text{Au}_{70}$ ,  $\text{Pd}_{45}\text{Au}_{55}$ , and  $\text{Pd}_{64}\text{Au}_{36}$  with metal loadings of 10–20 wt % on carbon black. The most active  $\text{Pd}_{30}\text{Au}_{70}$  nanoparticles demonstrated remarkably higher activities than commercial Pt/C catalysts, as seen in Figure 22a. The chronoamperometric curves (Figure 22b) indicated that the initial limiting currents of  $\text{Pd}_{30}\text{Au}_{70}/\text{C}$  were much higher than

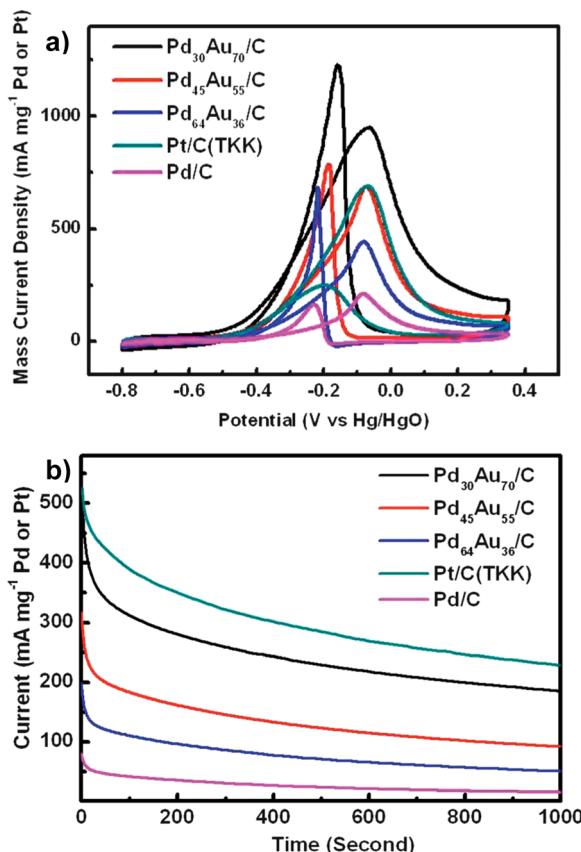


**Figure 22.** (a) Cyclic voltammograms of room temperature methanol oxidation on the heat-treated Pd/C, PdAu/C, and commercial Pt/C (TKK) catalysts in 1 M KOH + 1 M  $\text{CH}_3\text{OH}$  at  $50 \text{ mV s}^{-1}$ . (b) Chronoamperometry measurements of methanol oxidation in 1 M  $\text{CH}_3\text{OH}$  and 1 M KOH solution with PdAu/C, Pd/C, and commercial Pt/C (TKK) catalysts at  $-0.2 \text{ V}$  vs  $\text{Hg}/\text{HgO}$ . Adapted with permission from ref 188. Copyright 2013 The Royal Society of Chemistry.

those of the Pd/C catalyst, signifying a strong tolerance for intermediate species and enhanced electrocatalytic activity in contrast to Pd/C. In comparison to the PdAu nanoparticles prepared using a simple  $\text{NaBH}_4$  reduction technique, the PdAu nanoparticles prepared by emulsion-assisted synthesis displayed enhanced activity, which emphasized the importance of structure in electrocatalytic performance.<sup>188,190,199</sup>

Similarly, in an effort to synthesize different Pd–Au structures, Zheng and co-workers prepared Pd-decorated AuPd core–shell nanostructures (AuPd@Pd) using Good's buffer (4-(2-hydroxyethyl)-1-piperazineethanesulfonic acid, HEPES) as a reducing and shape-directing agent.<sup>164</sup> It has been observed that nanoparticles tend to agglomerate during repeated use in catalysis;<sup>200,201</sup> therefore, catalyst supports such as carbon,<sup>145,202</sup> CNTs,<sup>141,165,203</sup> graphene,<sup>99,118,150,204,205</sup> etc. may be employed to enhance dispersion. For instance, in work by Zheng et al.,<sup>164</sup> the synthesized graphene-supported AuPd@Pd exhibited enhanced specific activity and stability in contrast to graphene–Pd and commercial Pd black catalysts.

Taken together, enhancements obtained by multimetal catalysts may be attributed to one or more of the following contributions: (i) synergistic effects between metals—the incorporation of a second (or third) metal that can oxidize intermediates adsorbed onto the Pd active sites (e.g., Pd– $\text{CO}_{\text{ads}}$ ) at relatively lower potentials, thus increasing the rate of Pd active site regeneration, (ii) enlarged surface area provided

via a particular synthesis method (morphological variations offer the opportunity for additional active sites made available through atomic steps, edges, and corner atoms), and (iii) support materials, which may offer augmented surface areas, facilitate electron transfer, and reduce the risk of nanoparticle agglomeration.

It should also be noted that when Pd is modified with various oxides, including  $\text{CeO}_2$ ,  $\text{NiO}$ ,  $\text{Co}_3\text{O}_4$ , and  $\text{Mn}_3\text{O}_4$ , it demonstrates improved activity and stability over the leading PtRu/C catalysts for the oxidation of alcohol in alkaline media. The effects of oxide content on methanol oxidation were investigated by Xu et al.<sup>133</sup> for Pd– $\text{CeO}_2$  (1.3:1, w/w)/C, Pd– $\text{NiO}$  (4:1, w/w)/C, Pd– $\text{Co}_3\text{O}_4$  (2:1, w/w)/C, and Pd– $\text{Mn}_3\text{O}_4$  (2:1, w/w)/C, revealing a parabolic dependence on the oxide content in Pd electrocatalysts. The amount of metal oxide affects the catalytic activity and electrode stability, indicating that a high metal oxide content reduces electronic conductivity due to its semiconductor behavior.<sup>5</sup> Similar work by Ye et al.<sup>202</sup> further confirmed that the incorporation of oxides generated a higher activity than Pd/C for methanol oxidation. Additionally, as indicated in linear sweep voltammetry (LSV) curves (Figure 23a), the activity of methanol oxidation on Pd– $\text{NiO}$ /C and Pd– $\text{Co}_3\text{O}_4$ /C electrodes was much higher than that on Pd– $\text{Mn}_3\text{O}_4$ /C and Pd– $\text{CeO}_2$ /C electrodes. Ye et al.<sup>202</sup> observed through cyclic voltammograms (Figure 23b) that, during the forward scan, the adsorption of intermediate species occurred on the surface of the electrode, which poisoned the electrocatalysts. During the reverse sweep, the reoxidation of CO and other adsorbed species occurred with palladium oxides, exhibiting an increased resistance to poisonous species, when compared to that of Pd. This was believed to be the result of lattice oxygen within the oxides, which was considered as active oxygen that removed the CO intermediates of methanol oxidation.<sup>5,133,181</sup>

During the operation of a DMFC, methanol enters the system at the anode, where it is oxidized to carbon dioxide. However, the undesirable transport of methanol from the anode side through the electrolyte membrane to the cathode has been observed. Methanol reduction that occurs at the cathode dramatically reduces the overall performance by lowering the cell voltage and increasing the required oxygen stoichiometric ratio.<sup>181,206,207</sup> To address concerns of methanol crossover, extensive research has been carried out on the modification of Nafion-based membranes, which focused on blocking methanol transport while maintaining proton conductivity. Pd has been incorporated into Nafion membranes as a filler to decrease methanol permeability while maintaining high proton permeability.<sup>39,167,168,206–208</sup> Methanol crossover may be reduced through techniques such as sandwiching a thin film of Pd between Nafion membranes, the deposition of a Pd or Pd-based alloy thin film, or the deposition of Pd nanoparticles through ion exchange. Choi et al.<sup>167</sup> investigated the plasma modification of a Nafion surface along with Pd sputtering. Through this strategy, they were able to decrease the extent of methanol crossover by decreasing the pore diameters, increasing the methanol permeation length, and decreasing the hydrophilicity of the membrane surface. To lower methanol crossover, Hejze et al.<sup>168</sup> prepared a crack-free single-side Pd-plated Nafion membrane using electroless plating; however, only small current densities could be achieved. In more recent work, Iwai et al.<sup>206</sup> explored the preparation of Pd/Nafion composite membranes via a supercritical  $\text{CO}_2$  impregnation method using various Pd

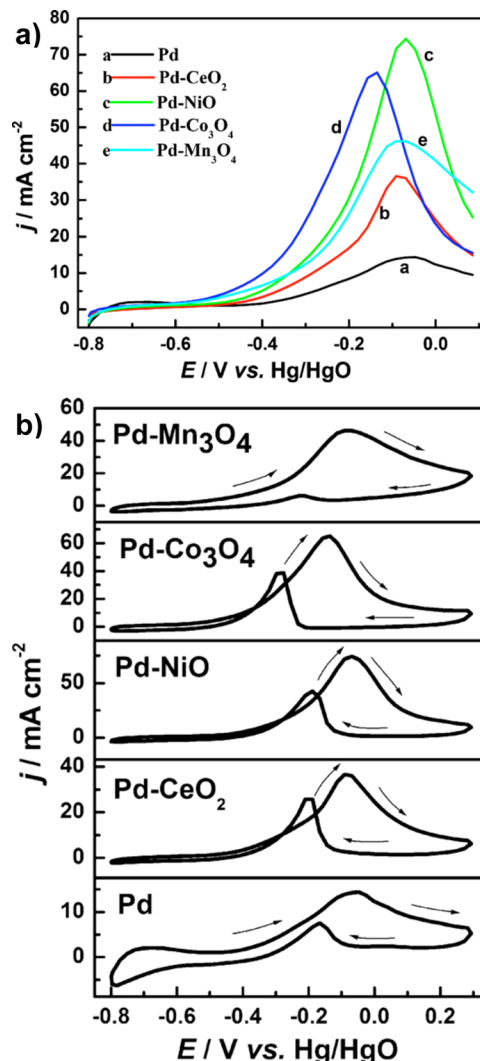


**Figure 23.** (a) LSV curves of methanol oxidation on the Pd/C, Pd– $\text{CeO}_2$ /C, Pd– $\text{NiO}$ /C, Pd– $\text{Co}_3\text{O}_4$ /C, and Pd– $\text{Mn}_3\text{O}_4$ /C electrodes. (b) Cyclic voltammograms of methanol oxidation on the Pd/C, Pd– $\text{CeO}_2$ /C, Pd– $\text{NiO}$ /C, Pd– $\text{Co}_3\text{O}_4$ /C, and Pd– $\text{Mn}_3\text{O}_4$ /C electrodes in 1.0 M KOH solution containing 1.0 M methanol with a sweep rate of 50 mV s<sup>-1</sup> and Pd loading of 0.30 mg cm<sup>-2</sup> at 303 K. Adapted with permission from ref 202. Copyright 2012 Elsevier.

complexes: palladium(II) acetylacetone [ $\text{Pd}(\text{acac})_2$ ], palladium(II) hexafluoroacetylacetone [ $\text{Pd}(\text{hfa})_2$ ], and palladium(II) bis(2,2,6,6-tetramethyl-3,5-heptanedionato) [ $\text{Pd}(\text{thd})_2$ ], where the supercritical fluid allowed for high diffusivity, which initiated high implantation penetration. Subsequent to the Pd complexes being impregnated into Nafion membranes, they were reduced by  $\text{NaBH}_4$  to produce membranes with decreased methanol permeability in comparison to pristine Nafion. The proton conductivity of the Nafion membranes was reliant on the particle size, where large particles acted as proton barriers, while small well-dispersed particles served to increased proton conductivities.  $\text{Pd}(\text{thd})_2$ /Nafion demonstrated the best membrane cell performance, where the loading amount of the Pd complex was dependent on the complex type.

In the short term, DMFCs represent the most promising technology for commercialization. However, challenges such as cost and durability continue to hinder their large-scale commercialization. In comparison to that on Pt-based electrocatalysts, minimal studies have focused on the oxidation of

methanol on Pd-based electrocatalysts. The further development and study of Pd-based nanomaterials will have positive impacts on future practical DMFC applications.

**3.1.2. Electrochemical Oxidation of Ethanol.** The harmful chemical toxicity and crossover of methanol limit its widespread commercial application in fuel cells. This has attracted considerable attention toward alternative fuel sources, such as ethanol, and its application in direct alkaline alcohol fuel cells (DAAFCs). Ethanol boasts the advantage of reduced toxicity and higher theoretical energy density ( $8.1 \text{ kW}\cdot\text{h}\cdot\text{kg}^{-1}$  for ethanol vs  $6.1 \text{ kW}\cdot\text{h}\cdot\text{kg}^{-1}$  for methanol), and its production is less dependent on fossil fuels.<sup>5,209</sup>

The ethanol oxidation reaction (EOR) in alkaline electrolyte is a complex reaction with multiple pathways, resulting in 2-, 4-, or 12-electron transfer. In direct ethanol fuel cells (DEFCs), ethanol was selectively converted to acetate on Pd-based electrocatalysts under the condition that they did not contain Pt, and that the solution was strongly alkaline (Figure 24).<sup>172,209</sup> In electrolytes with high  $\text{OH}^-$  concentrations, the

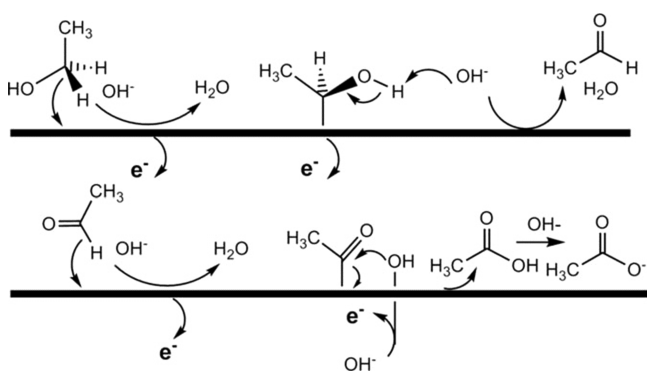


**Figure 24.** Proposed mechanism for the selective conversion of ethanol into acetate on Pd-based electrocatalysts in alkaline media. Reprinted with permission from ref 172. Copyright 2009 Elsevier.

reaction is predominantly a 4-electron transfer, with acetate as the final product. By lowering the pH and effectively limiting the concentration of  $\text{OH}^-$ , the reaction may continue to complete oxidation and the production of  $\text{CO}_2$ .<sup>173,209</sup> The completion of ethanol oxidation is determined by the degree of  $\text{CH}_3\text{CO}_{\text{ads}}$  and  $\text{OH}_{\text{ads}}$  coverage, which suggests that the kinetics of the ethanol oxidation reaction is improved via the availability of  $\text{OH}^-$  ions in solution and/or the  $\text{OH}^-$  coverage of the electrode surface.<sup>90</sup>

Research pertaining to the investigation of Pd-based catalysts as a replacement for Pt-based catalysts has emphasized a higher catalytic activity and improved steady-state behavior for ethanol oxidation on Pd, in contrast to Pt.<sup>90,93,129,150,170,210–213</sup> In situ FTIR spectroscopy was employed by Fang et al.<sup>213</sup> to gain insight into the mechanism of ethanol electrooxidation on Pd under exposure to different pH values (Figure 25). The selectivity of ethanol oxidation on Pd in strong alkaline media was observed at NaOH concentrations higher than 0.5 M, displaying only characteristic bands of acetate ions (1558 and  $1415 \text{ cm}^{-1}$ ). This behavior was in contrast to Pt-based electrocatalysts in acidic media, which invariably oxidized ethanol into mixtures of acetic acid, aldehyde, and  $\text{CO}_2$ . A further understanding of the FTIR spectra revealed that at pH values equal to or lower than 13  $\text{CO}_2$  was formed ( $\text{CO}_2$  formation band at  $2343 \text{ cm}^{-1}$ ), indicating that the efficacy of the catalyst was decreased with increasing pH.

Pd-based materials have demonstrated a marked superiority in comparison to Pt-based materials, in terms of reactivity, poison tolerance, and cost, toward ethanol electrooxidation. However, Pd has a low natural tendency to cleave C–C bonds. To improve the electrocatalytic activity of Pd, ethanol oxidation on adatom-modified, alloyed, and oxide-promoted Pd-based electrocatalysts has been investigated in alkaline media. Nguyen et al.<sup>214</sup> reported the shifting of the d-band center when alloying Pd with Ag to form PdAg/C catalysts with enhanced activity for ethanol oxidation in alkaline media, as compared to Pt/C and Pd/C. As well, they observed that the addition of Ag facilitated the removal of the common poisoning intermediate (CO) from the surface of PdAg/C to further improve the catalytic efficiency of Pd. In more recent work, Kakaei et al.<sup>178</sup> compared the electrocatalytic activity of PdAg/GO to that of Pd/GO in the oxidation of ethanol. Once again, the incorporation of Ag revealed improved electrocatalytic activity for ethanol electrooxidation, as described by the d-band center theory. Work with Pd–Au has also been reported by many groups as a means to improve the electrocatalytic activity of Pd.<sup>104,134,137,177,215</sup>

It has been noted that Au may catalyze reactions such as CO oxidation and the partial oxidation of hydrocarbons with high efficiency. Coupled with the ability to stabilize neighboring metal catalysts due to their inherent unique electron-withdrawing properties, Pd–Au catalysts appear very promising for ethanol oxidation reactions.<sup>177</sup> Cui et al.<sup>104</sup> synthesized and studied unsupported Pd–Au nanoparticle tubes with a tunable interface and demonstrated the enhanced effects of Pd and Au nanoparticles in the electro-oxidation of ethanol. Cyclic voltammograms of the catalysts in 1.0 M KOH with (b–e) and without (a) 1.0 M  $\text{C}_2\text{H}_5\text{OH}$  are displayed in Figure 26. Regarding the activity of Pd surface sites modified by Au, the catalytic activity of the catalysts initially increased with elevated Au content, and then decreased, when the Au atom percentage was further increased from 20 to 50 atom % (Figure 26b). Concerning the catalytic activity when the mass of Pd was normalized (Figure 26c), a continuous improvement was shown, pending an excess increase of the Au component up to 35 atom %. Further examination of the long-term catalytic performance was performed using CA (Figure 26f), which showed initial increases in the ethanol oxidation current with decreasing Pd content, followed by sharp decays at the electrodes that contained less than 80 atom % Pd. These results indicated that the electrocatalytic activity had no direct relation to individual metal components in the Pd–Au system. Comparable work conducted by Qin et al.<sup>177</sup> focused on the degree of alloying between Pd and Au nanoparticles, in which it was determined that low alloyed Pd–Au/C catalysts demonstrated increased electrocatalytic activities, versus their highly alloyed counterparts.

Various other Pd-based alloyed materials, such as PdCu,<sup>175</sup> PdAgTe,<sup>174</sup> PdSn,<sup>134</sup> and PdNi,<sup>171–173,176,216</sup> have been investigated over the past decade. Of these, PdNi showed promising electrocatalytic activity, as well as exhibited increased corrosion resistance.<sup>176,216</sup> Shen et al.<sup>171</sup> synthesized carbon-supported PdNi catalysts and compared their performance to that of Pd/C toward EOR. Figure 27 presents the polarization and power density curves of Pd/C and  $\text{Pd}_2\text{Ni}_3/\text{C}$  measured in 3.0 M ethanol + 5.0 M KOH solutions, revealing that  $\text{Pd}_2\text{Ni}_3/\text{C}$  exhibited improved performance over Pd/C, in terms of both open-circuit voltage (OCV) and power density. With  $\text{Pd}_2\text{Ni}_3/\text{C}$  as the anode, the OCV was 0.89 V and the peak power density was  $90 \text{ mW}\cdot\text{cm}^{-2}$ , while Pd/C had an OCV of 0.79 V and a

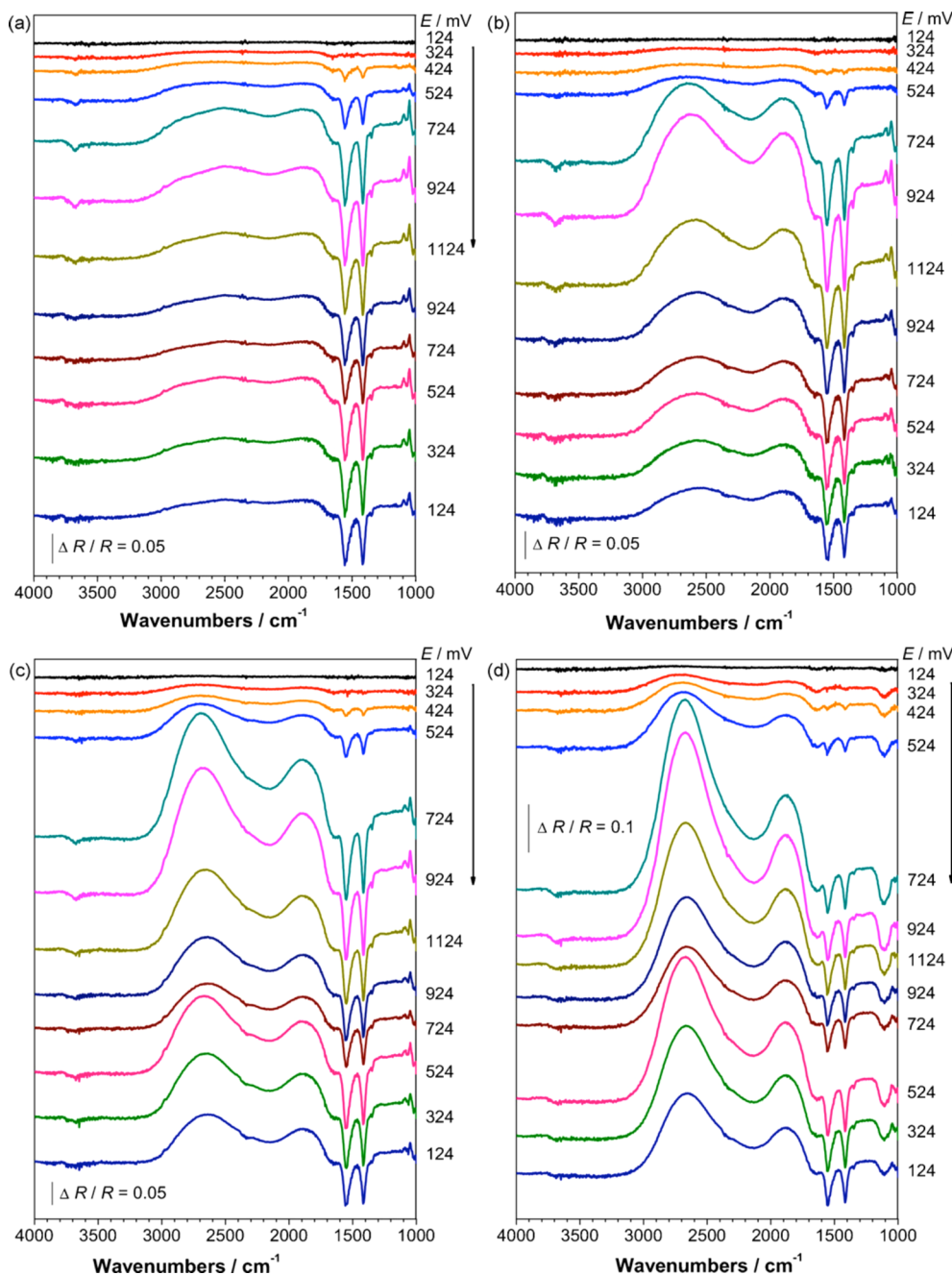


**Figure 25.** In situ FTIR spectra obtained under potential step polarization in 1 M ethanol with different NaOH concentrations of (a) 5 M, (b) 2 M, (c) 1 M (pH 14), (d) 0.5 M NaOH + 0.5 M NaClO<sub>4</sub> (pH 13.3), (e) 0.1 M NaOH + 0.9 M NaClO<sub>4</sub> (pH 13), and (f) 0.05 M NaOH + 0.95 M NaClO<sub>4</sub> (pH 12.7).  $E_t = 24$  mV, scan number 128. The arrows indicate the potential polarization direction. Reprinted with permission from ref 213. Copyright 2009 Elsevier.

peak power density of 67 mW·cm<sup>-1</sup>. These results further confirmed that incorporation of a second metal to Pd may improve its catalytic activity toward EOR in alkaline media. Analogous to the case of methanol oxidation on Pd-based materials, the incorporation of a second metal activated water, which oxidized the adsorbed CO- and CHO-type species, thereby liberating the active sites of the surface. Furthermore, the second metal served to increase the amount of adsorbed water on the surface, which might inhibit CO chemisorption.<sup>178</sup>

The effect of some common metal oxides, including ZrO<sub>2</sub>, SnO<sub>2</sub>, Co<sub>3</sub>O<sub>4</sub>, NiO, Fe<sub>3</sub>O<sub>4</sub>, and MnO<sub>2</sub>,<sup>129,133,173,209</sup> on the electrocatalytic activity of Pd for EOR has been investigated.

The enhancement of the electrocatalytic performance of Pd by metal oxides may be primarily attributed to (i) the stabilization of nanoparticles against sintering during the catalytic process, (ii) the strong metal–support interactions, where metal oxides may alter the electronic structure of Pd nanoparticles through interfacial bonding or electron transfer between Pd and metal oxides, and (iii) the increase of OH<sup>-</sup> at the electrode surface by the oxide phase, which facilitates the oxidation/removal of intermediates that are adsorbed onto the Pd sites during the electrochemical oxidation of ethanol.

Nickel oxide has proven to be a highly efficient cocatalyst for the stimulation of Pd electrocatalytic activity in the oxidation of

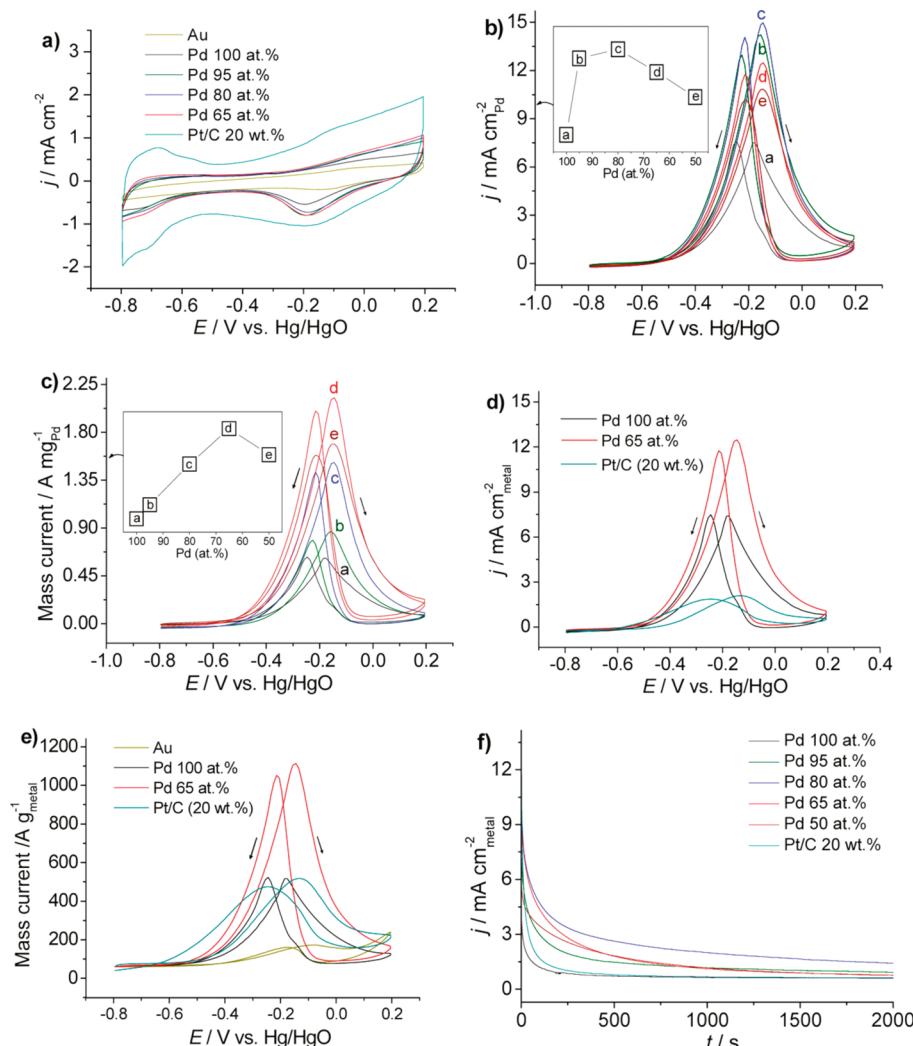


**Figure 26.** Cyclic voltammograms for determining the relative ECSA change of Pd and electrocatalytic activity. (a) Cyclic voltammograms recorded in a  $\text{N}_2$ -purged 1.0 M KOH solution at room temperature. Pseudoarea activity (b) and mass activity (c) of unsupported PdAu BHTs with different Pd atom percentages for ethanol oxidation in 1.0 M KOH + 1.0 M  $\text{C}_2\text{H}_5\text{OH}$ . The insets show the peak current variation by increasing the Au atom percentage. (d) Pseudoarea activity and (e) mass activity of Pd NP tubes, unsupported PdAu BHTs, and Pt/C catalyst. (f) Chronoamperometric curves for ethanol electrooxidation at  $-0.3 \text{ V}$  versus Hg/HgO on Pd NP tubes, unsupported Pd–Au BHTs, and Pt/C catalyst. Scan rate 50 mV s<sup>-1</sup>. Reprinted from ref 104. Copyright 2011 American Chemical Society.

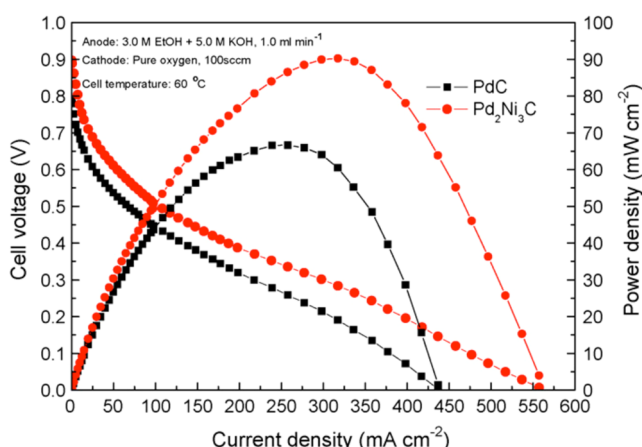


**Figure 27.** Polarization and power density curves of alkaline DEFCs with different anode catalysts (the anode was 3.0 M ethanol and 5.0 M KOH aqueous solution). Reprinted with permission from ref 171. Copyright 2009 Elsevier.

ethanol.<sup>133,172</sup> Combined with  $\text{CoO}_x$ , Wang et al.<sup>173</sup> synthesized a hybrid  $\text{NiCoO}_x$  adjacent to a Pd catalyst (Pd– $\text{NiCoO}_x$ /C) through the epitaxial growth of Pd into an oxidized NiCo alloy. The intimate proximity of  $\text{NiCoO}_x$  to the Pd nanoparticles led to strong metal–support interactions, demonstrating higher conductivity and improved electrochemical activity for the oxidation of ethanol in alkaline media. An experimental understanding of the difference between an intrinsic effect gained from an alloyed system and a synergistic effect resulting from the presence of an oxide phase was pursued by Martinez et al.<sup>209</sup> Two different methods, spray pyrolysis (SP) and a sacrificial support method (SSM), were employed for the preparation of the  $\text{SnO}_2$  phase, which was subsequently followed by the chemical reduction of Pd onto the oxide phase. XRD analysis revealed the presence of both Pd and  $\text{SnO}_2$  phases in the synthesized Pd– $\text{SnO}_2$ (SP) and Pd– $\text{SnO}_2$ (SSM) samples. To understand the mechanism of the electrochemical oxidation of ethanol, *in situ* IRRAS (infrared reflection absorbance spectroscopy) spectra of the highly active Pd– $\text{SnO}_2$ (SP) electrocatalyst were recorded in a 1.0 M KOH +

1.0 M ethanol electrolyte. The characteristic peaks centered at 1045, 1086, 1410, and 1549 cm<sup>-1</sup> were observed (Figure 28a),

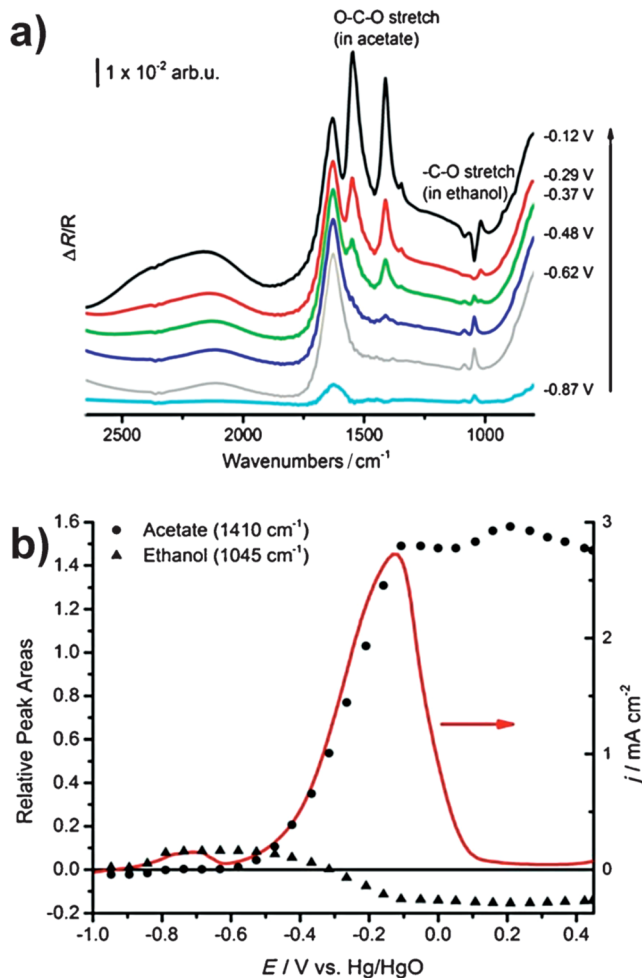


**Figure 28.** (a) IRRAS spectra of the ethanol electrooxidation reaction by Pd–SnO<sub>2</sub>(SP) catalyst in a 1 M KOH electrolyte. (b) Forward sweep voltammogram of the oxidation reaction. Conditions: 1 M ethanol, 1 mV s<sup>-1</sup>, 228 °C, 0 rpm. Reprinted with permission from ref 209. Copyright 2014 Wiley-VCH Verlag GmbH & Co.

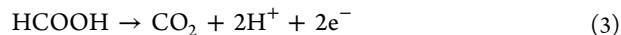
confirming the absorption of ethanol at the surface and the formation of acetate. A comparison of the forward sweep voltammogram for the corresponding oxidation of ethanol and the integrated areas for characteristic peaks of ethanol ( $\tilde{\nu} = 1045\text{ cm}^{-1}$ ) and acetate ( $\tilde{\nu} = 1410\text{ cm}^{-1}$ ) is presented in Figure 28b. It was revealed that the acetate species appeared exactly at the onset potential of the ethanol oxidation and that the amount of acetate produced was increased with an increase of the potential and reached a maximum at the peak potential ( $-0.10\text{ V}$ ). The same experiments were repeated with a 0.1 M KOH + 1 M ethanol electrolyte, showing that the generated intermediates and products were different from those produced at the higher pH (1.0 M KOH). It was concluded that, at high hydroxide ion concentrations, SnO<sub>2</sub> acted as a cocatalyst to provide OH<sup>-</sup> to the interfacial layer, increase the turnover rate, and effectively limit the final product to acetate. Conversely, at limited OH<sup>-</sup> concentrations, the OH<sup>-</sup> ions in close proximity to the reaction surface were consumed by the partial dehydrogenation of ethanol, thereby limiting the formation of

acetate, which allowed the adsorbed ethanol species to proceed to complete oxidation.

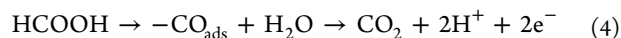
For ethanol oxidation on Pd-based materials, improved results were obtained by means of environmental adaptations (e.g., concentration and pH dependencies), adatom modifications, alloy formation, and oxide promotion. All of these factors may be applied to the rational design of next-generation electrocatalysts for the oxidation of other fuels. Furthermore, the attributes of Pd underline the potential of Pd-based materials in the future use of DEFCs as power sources for portable applications and motor vehicles.

### 3.2. Electrochemical Oxidation of Formic Acid

The increased interest in alternative fuel sources has led to the use of formic acid in polymer electrolyte membrane (PEM)-based fuel cells, which are referred to as direct formic acid fuel cells (DFAFCs). In comparison to DMFCs, the advantages of formic acid oxidation over that of methanol include decreased crossover effects through the proton exchange membrane, increased electrooxidation rates, low toxicity, and low-temperature operation.<sup>1</sup> The disadvantage of formic acid is associated with its low volumetric energy density; however, this limitation may be overcome by increasing the concentration of formic acid. The mechanism involved with formic acid electro-oxidation is typically thought to occur via a parallel or dual pathway. Direct oxidation, also referred to as the dehydrogenation pathway, occurs without the formation of CO as a reaction intermediate:<sup>217–219</sup>

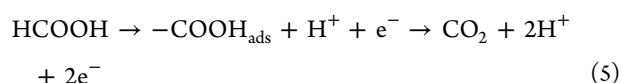


Indirect oxidation, also referred to as the dehydration pathway, forms adsorbed CO as a reaction intermediate:



The dehydrogenation pathway in eq 3 is the preferred pathway due to the complete oxidation of formic acid to CO<sub>2</sub>. The formation of surface-adsorbed CO species during the dehydration reaction pathway in eq 4 is undesirable and leads to the requirement for higher electrode potentials for oxidation to CO<sub>2</sub>. An ideal DFAFC catalyst would operate under the dehydrogenation pathway to produce enhanced overall cell efficiency, while avoiding the poisoning of the catalyst.

It is widely accepted that the electrooxidation of formic acid on Pd surfaces occurs predominantly through the direct pathway, which avoids the formation of the catalyst poisoning intermediate (CO). However, in comparison to that for the oxidation of formic acid on Pt, the mechanism for the oxidation of formic acid on Pd has been less studied. A proposed mechanism for Pd-mediated formic acid oxidation involves a multistep reaction that is similar to that required for Pt. In addition to the aforementioned direct and indirect oxidation mechanisms, the electrochemical oxidation of formic acid through adsorbed formate species has also been reported:<sup>81,219–221</sup>



On the contrary, it is believed that formate is a short-lived reactive intermediate that is derived from the oxidation of formic acid, which is detected only when its decomposition, yielding CO<sub>2</sub>, is suppressed.<sup>219,222</sup>

It has been demonstrated that Pd-based catalysts have superior performance when compared with those comprised of Pt. Nonetheless, DFAFCs with Pd catalysts continue to exhibit significant decay subsequent to discharging for several hours. Originally, it was believed that adsorbed CO-like species could explain the decay of Pd, similar to that of Pt. However, CO-like species have not been definitively detected during the oxidation of formic acid.<sup>221,223</sup> The mechanism of decay remains particularly unclear, giving rise to the proposal of adsorbed formate ( $\text{HCOO}^-$ ) ion species or hydroxyl ( $\text{OH}^-$ ) ions or other adsorbed anions as the poisoning species on the Pd surface.<sup>220,222,224,225</sup>

Although the nature of poisoning species remains subject to controversy, methods for the recovery of the poisoned Pd catalysts have been explored. Techniques such as anodic polarization might recover catalyst activity by oxidizing the adsorbed poisoning species; however, Pd oxidation or dissolution is a concern at anodic potentials.<sup>226</sup> Another approach, as described by Zhou et al.,<sup>221</sup> introduced a nonelectrochemical technique for the regeneration of Pd using pure water, yet extended regeneration times of over an hour have deterred proficiency. An alternative approach is the use of cathodic polarization, which takes advantage of the inability of low potentials to corrode Pd and short regeneration recovery times. Jeon et al.<sup>227</sup> were able to reactivate Pd/C catalysts in formic acid oxidation through the application of a pulsed cathodic potential of  $-0.2$  V, for 10 s, every 60 s. Figure 29 compares the current density of Pd under a constant

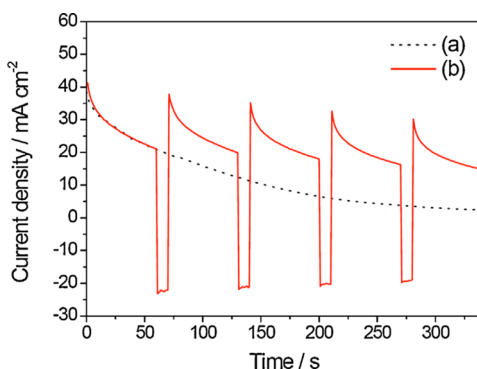


**Figure 29.** Current density vs time profiles of Pd (a) under a constant potential of 0.5 V and (b) in the pulsed potential method (0.5 V for 60 s,  $-0.2$  V for 10 s) in 2 M  $\text{HCOOH}$  and 0.5 M  $\text{HClO}_4$ . Reprinted with permission from ref 227. Copyright 2014 Elsevier.

potential of 0.5 V and that in the pulsed cathodic potential method, showing that periodically applied cathodic polarization delayed the deactivation of the Pd electrocatalyst considerably.

Toward the goal of understanding the mechanism of formic acid electrooxidation on Pd-based surfaces, a variety of nanocatalysts with high catalytic activity, durability, and lower cost have been produced. As is relatively well-known, the electronic properties of nanoparticles may be adjusted by controlling their dimensions. In general, the smaller the nanoparticle, the lower its d-band center, which in turn results in a decrease in its adsorption energy. With respect to the oxidation of formic acid, lowering of the d-band center reduces the binding energy of hypothetical intermediates, thereby enhancing the rate of reaction.<sup>220,228</sup> Nanoparticle size effects in formic acid electrooxidation were investigated by Zhou and Lee<sup>229</sup> using a series of carbon-supported Pd nanoparticles,

with sizes ranging from 2.7 to 9.0 nm. Their results suggested that the oxidation of formic acid is a surface structure-sensitive reaction, where the strong size effect of Pd nanoparticles may be attributed to the geometric requirements of the active adsorption sites.

Catalytic activity is not only size-dependent, but also facet-dependent. During formic acid oxidation on single-crystal Pd, the current is greatly affected by the crystallographic orientation of the surface.<sup>218,229</sup> The structural effects of formic acid oxidation were examined by Hoshi et al.<sup>230,231</sup> on well-defined Pd single-crystal electrodes with low- and high-index planes. The low-index planes presented the following activity series according to the maximum current density of the positive-going scan:  $\text{Pd}(110) < \text{Pd}(111) < \text{Pd}(100)$ . For the high-index planes, the maximum current density increased in the order  $\text{Pd}(S)-[n(111) \times (111)] < \text{Pd}(S)-[n(111) \times (100)] < \text{Pd}(S)-[n(100) \times (110)] < \text{Pd}(S)-[n(100) \times (111)]$ , with  $\text{Pd}(511) (=5(100) \times (111))$  having the highest catalytic activity overall. To enhance the catalytic properties for formic acid, different preferred facets may be obtained by controlling the shape of the nanocrystals. Lee et al.<sup>232</sup> prepared shape-controlled polygonal Pd nanostructured catalysts with dominant {111} facets. The polygonal Pd/C resulted in a much higher current density for formic acid electrooxidation compared to that of Pd/C, at 1.908 and 0.478  $\text{mA cm}^{-2}$ , respectively. Alternatively, dendritic structures have been employed for their bifurcating branches, which provide numerous high-index facets.<sup>106,210</sup> Morphologies such as Pd nanoflowers offer improvements similar to those seen with dendrites. Flower-like Pd nanostructures display drastically enhanced activity over conventional Pd nanoparticles toward the electrooxidation of formic acid.<sup>233,234</sup>

Various binary Pd-based catalysts have been synthesized, giving enhanced electrocatalytic activity for ethanol electro-oxidation. Incorporated metals include, but are not limited to, Pt, Au, Ag, Cu, Cd, Ni, Pb, Sn, Fe, and Ir.<sup>70,81,84,88,121,122,132,140,146,160,235,236</sup> Winjobi et al.<sup>140</sup> compared the activities of Pt, Pd, and PtPd alloyed nanoparticles supported on CNTs. The cyclic voltammograms presented in Figure 30 showed that increases in the amount of Pd within the

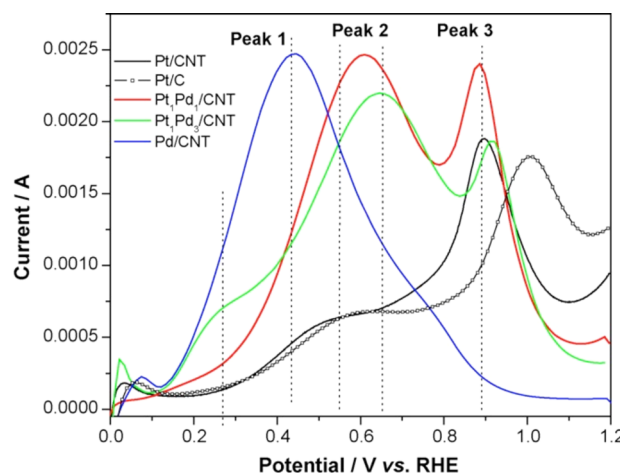


**Figure 30.** Cyclic voltammograms of formic acid oxidation on Pt/CNT,  $\text{Pt}_1\text{Pd}_1/\text{CNT}$ ,  $\text{Pt}_1\text{Pd}_3/\text{CNT}$ , Pd/CNT, and Pt/C (E-TEK) in 0.5 M  $\text{H}_2\text{SO}_4$  + 0.5 M  $\text{HCOOH}$  at a sweep rate of 50  $\text{mV s}^{-1}$  and at room temperature. Only the positive-going potential scans are reported. Reprinted with permission from ref 140. Copyright 2010 Elsevier.

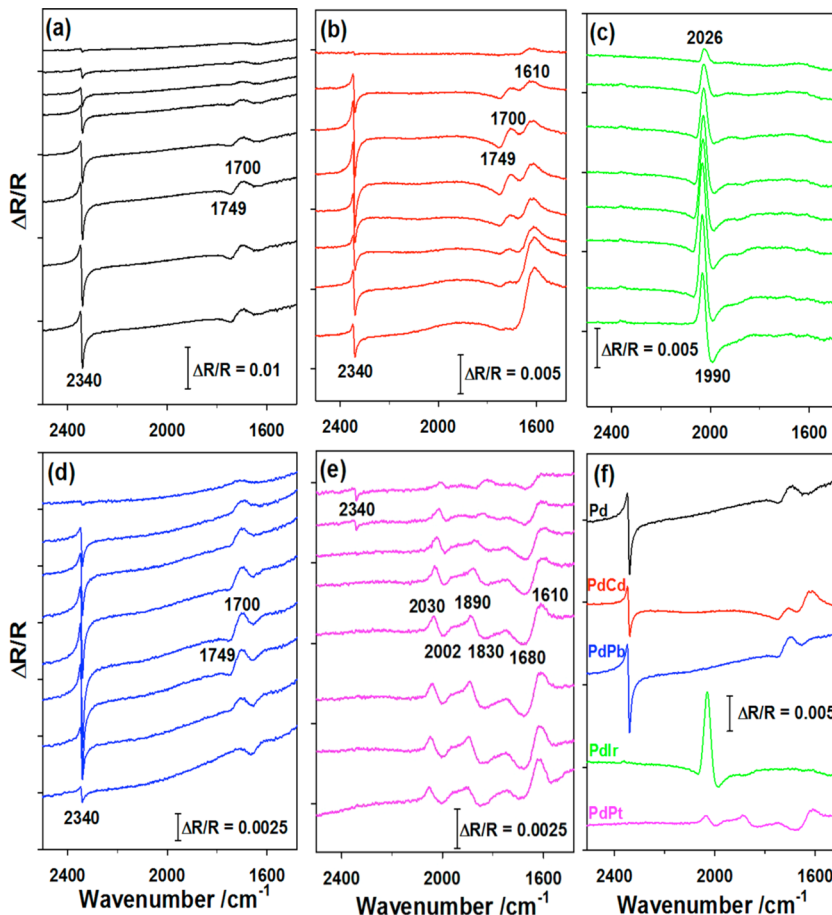


**Figure 31.** FTIR spectra of the formic acid oxidation in 0.1 M  $\text{H}_2\text{SO}_4$  + 0.1 M HCOOH on (a) Pd, (b) PdCd, (c) PdIr, (d) PdPb, and (e) PdPt from  $-0.1$  V (top) to  $+0.6$  V (bottom) taken at 0.1 V intervals and (f) of all catalysts at  $+0.3$  V. Reprinted from ref 81. Copyright 2014 American Chemical Society.

catalyst exhibited a preference for the direct formic acid oxidation pathway. Au serves as an attractive element for PdAu-based binary catalysts due to its ability to suppress the dissolution of Pd under highly oxidizing conditions. These properties were exploited by Zhang et al.,<sup>146</sup> who prepared Pd–Au/C catalysts with both low and high degrees of alloying. It was found that PdAu catalysts with a high degree of alloying demonstrated enhanced electrocatalytic activity and more stability than PdAu/C catalysts with low-level alloying. This may be attributed to the enhancement of CO tolerance and possible dehydration pathway suppression in the course of formic acid electrooxidation.

More recently, Adams et al.<sup>81</sup> investigated the catalytic activity of nanoporous Pd and four binary Pd–M catalysts with an atomic ratio of 90:10 (where M = Cd, Pb, Ir, and Pt) toward the electrochemical oxidation of formic acid. Chronoamperometric measurements indicated that the initial electrochemical performance of the nanoporous Pd–M electrodes toward formic acid oxidation was almost independent of the alloying materials; however, the second incorporated metal strongly affected the stability of the Pd-based electrocatalysts. In situ electrochemical attenuated total reflection Fourier transform infrared (ATR-FTIR) spectroscopic studies were carried out to decipher the origin of the degradation of electrocatalytic activity for particular catalysts and the mechanisms of the electrochemical oxidation of formic acid at the Pd-based nanoporous electrodes. The FTIR spectra (Figure 31) revealed that

oxidation on the nanoporous Pd, PdCd, and PdPb catalysts proceeded predominantly through the direct mechanism to produce  $\text{CO}_2$  peaks at  $2349\text{ cm}^{-1}$ , showing the complete oxidation of formic acid, while alternatively the indirect mechanism with major CO poisoning ( $\text{CO}_L$  stretch between  $2030$  and  $1990\text{ cm}^{-1}$ ; set of bipolar  $\text{CO}_B$  peaks between  $1890$ – $1830$  and  $1680$ – $1610\text{ cm}^{-1}$ ) was observed for the PdIr and PdPt electrodes. The incorporation of even diminutive amounts of Pt and Ir was found to inhibit the oxidation of formic acid, with a large quantity of CO produced, which initiated a rapid decay in catalytic activity. On the other hand, the addition of the inexpensive Pb and Cd promoted the direct mechanism, which facilitated further decreases in the cost of the Pd-based catalysts. In summary, Pd has proven to not only exhibit high catalytic activity for the oxidation of formic acid, but also overcome the CO poisoning effect. Consequently, research into the synthesis of advanced Pd-based electrocatalysts for formic acid oxidation will be essential for the development of DFAFCs.

### 3.3. Electrochemical Reduction of Oxygen

One of the primary challenges for the use of electrocatalysts in fuel cells is the development of high-performance cathode catalysts to reduce the high overpotential that is present during the oxygen reduction reaction (ORR). Researchers have made considerable progress in the elucidation of ORR on Pt and Pt-based bimetallic alloy electrocatalysts;<sup>237,238</sup> however, Pt catalyst materials are scarce and expensive. Pd exhibits

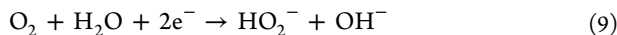
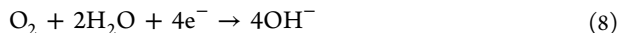
considerable catalytic activity toward ORR, which promotes Pd alloys as feasible alternatives in the development of non-platinum catalysts with catalytic activity similar to that of Pt.

The mechanism of electrochemical ORR is rather complex, involving catalyst, electrode material, and electrolyte dependency, which may produce a variety of intermediates. Nevertheless, ORR in aqueous solutions may be summed up to occur primarily through two pathways: the direct four-electron reduction pathway and the two-electron reduction pathway. In fuel cell processes, the four-electron pathway is highly preferred due to its enhanced power generation. Dependent on the aqueous electrolyte (acidic vs alkaline), the ORR mechanism occurs as follows:<sup>91,239,240</sup>

acidic aqueous solution



alkaline aqueous solution



In acidic media, pure Pd activity is higher than that of all other noble metals except for Pt; however, the tendency of Pd toward dissolution in acidic media decreases the electrode stability, which prevents it from being directly utilized in fuel cells. The examination of ORR in alkaline solutions has revealed that Pd exhibits higher activity than in acidic solutions due to a decrease in the anion poisoning effect in alkaline solutions.<sup>74,97,240–242</sup> A desired ORR catalyst is one that forms a moderate bond with the adsorbates to balance the kinetics of O–O bond breaking and the removal of oxygen-containing species.<sup>6</sup>

It is known that ORR strongly depends on the crystallographic orientation of the electrodes. Facet-dependent ORR activities for Pd single crystals have been examined by Kondo et al.<sup>243</sup> in acidic media. The low-index planes of Pd gave the following order of activity in ORR: Pd(110) < Pd(111) < Pd(100). This is completely the opposite of that on low-index Pt planes. In addition, Pd(100) surfaces exhibit much higher activity compared to that of any of the Pt planes (Figure 32). To better understand why pure Pt may serve as an ORR electrocatalyst, whereas Pd cannot, Ou et al.<sup>244</sup> conducted detailed density functional theory (DFT) calculations on the geometric structures and minimum energy pathways for the adsorption and dissociation of O<sub>2</sub> on Pt(111) and Pd(111) surfaces in the presence of hydrated hydronium ions. Their results indicated that, in the presence of hydrated protons, only the dissociated mechanism of O<sub>2</sub> molecules occurred on the Pd(111) surface, whereas, on the Pt(111) surface, the dissociated mechanism of O<sub>2</sub> molecules and OOH species occurred. It was found that the rate-determining step (rds) on both the Pd(111) and Pt(111) surfaces was the protonation of adsorbed O atoms to form OH. Given that the adsorption and dissociation processes of O<sub>2</sub> molecules occur more easily on Pt(111) surfaces, the rds can explain why Pt may better serve as an ORR electrocatalyst.

Hoshi et al.<sup>245</sup> studied the facet dependence of ORR with a monolayer dispersed Pt film on bare Pd(111), Pd(100), and Pd(110) surfaces in acidic media. Their work showed that, on bare Pd(hkl) electrodes, the activity for ORR was strongly contingent on the surface structure. However, voltammograms of ORR on the Pt/Pd(hkl) electrodes do not rely on the crystal

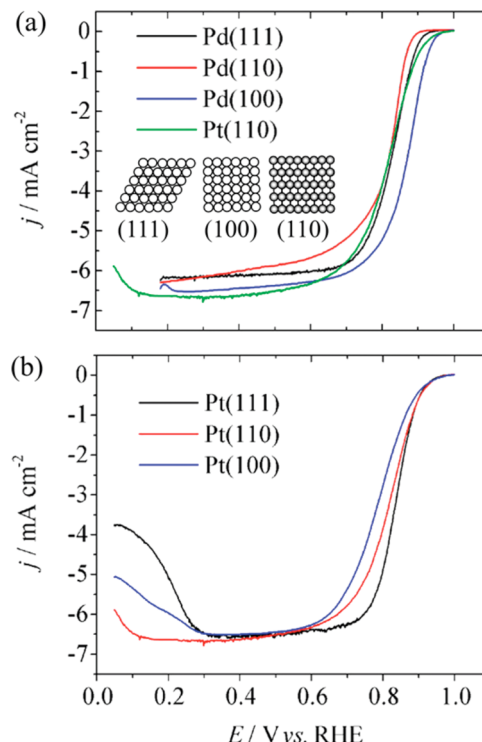


**Figure 32.** Voltammograms of the oxygen reduction reaction using a rotating disk electrode in 0.1 M HClO<sub>4</sub> saturated with O<sub>2</sub>. Rotation rate 2000 rpm. Scanning rate 0.010 V s<sup>-1</sup>. (a) Low-index planes of Pd. The result for Pt(110) is also shown for comparison. The inset shows the hard sphere models of the low-index planes. (b) Low-index planes of Pt. Reprinted from ref 243. Copyright 2009 American Chemical Society.

orientation. No Pt/Pd(hkl) electrode exceeded the activity for ORR on bare Pd(100), but their current densities exceeded that of Pt(110), which was the highest in the low-index planes of Pt. Similar studies were carried out by Zhang et al.,<sup>246</sup> whose work involved mixed-metal Pt monolayer electrocatalysts deposited on Pd(111), showing enhanced ORR kinetics.

The ORR activity of Pd-based catalysts is reliant on material morphologies.<sup>18,82,100,101,242,247,248</sup> Xiao et al.<sup>100</sup> examined the structure–activity relationships of Pd catalysts, which showed a strong correlation between their morphologies and activities toward ORR. The surface specific activity of Pd nanorods toward ORR was found to be 10-fold higher than that of Pd nanoparticles. Furthermore, Erikson et al.<sup>247</sup> prepared cubic Pd-based nanoparticles with a large fraction of (100) surface sites that exhibited superior electrocatalytic activity toward ORR in comparison to spherical Pd nanoparticles and bulk Pd. Most recently, Huang et al.<sup>248</sup> compared the specific activities of truncated Pd nanocubes with (100) planes on six facets and (111) planes that appeared on the corners of the nanocubes and those of nanoparticles in alkaline media. As previously seen in acidic media, the Pd nanocubes exhibited enhanced activity for ORR.

The ORR activities of well-defined triangular Pd nanorods supported on Au were reported by Choi et al.<sup>101</sup> Figure 33 displays the cyclic voltammograms obtained from the triangular Pd rod and bare Pd and Pt surfaces in O<sub>2</sub>-saturated 0.1 M HClO<sub>4</sub>. The Pd nanorods exhibited much higher electrocatalytic activity than the bare Pt and Pd surfaces. Further structural analysis revealed that the Pd nanorods had a significant presence of Pd(100) over Pd(110) and Pd(111)

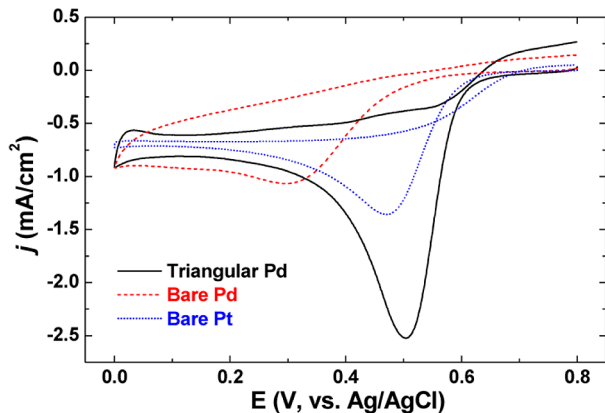


**Figure 33.** Cyclic voltammograms obtained on bare Pd, bare Pt, and triangular Pd rod surfaces in  $O_2$ -saturated 0.1 M  $HClO_4$ . Scan rate 50 mV s<sup>-1</sup>. Adapted from ref 101. Copyright 2014 American Chemical Society.

crystalline domains on their surfaces in comparison to the bare Pd surface.

The exploration of particle size effects has played an important role in the development of the desired catalytic properties, where it has been suggested that metal–oxygen interactions may be altered as a function of particle size at the nanoscale.<sup>6,130,240,249</sup> In work by Zhou et al.,<sup>249</sup> the specific mass activity in ORR of Pd nanoparticles, with a particle size range of 2.7–8.7 nm, increased monotonically with decreases in Pd particle size and increases in electrochemically active surface area. These strong particle size effects were attributed to a combination of the ORR activities on different low-index planes, surface site types, and electronic effects in catalysis. The most favorable Pd nanoparticle dimensions were suggested to be in the range of 5.0–6.0 nm.

Highly active Pd-based alloys (e.g., Pd–Co) without Pt for ORR in an acid medium were reported by Savadogo et al.,<sup>36</sup> which inspired the design and synthesis of appropriate Pd-based alloys with specific compositions to develop novel catalysts for fuel cell applications.<sup>74,91,127,164,241,242,250–252</sup> The improvement of ORR kinetics on Pd surfaces requires the reduction of oxygen binding energies by lowering its d-band center.<sup>6</sup> Pd–Co–Au electrocatalysts were fabricated by Raghubeer et al.<sup>127</sup> via conventional borohydride and microemulsion methods for ORR. Samples prepared via the microemulsion method fared better than those prepared via borohydride reduction for the catalytic activity of ORR due to the higher degree of alloying, smaller nanoparticle sizes, and larger surface areas. Compared to Pt/C catalysts at 60 °C, the activities of the prepared Pd–Co–Au samples via the microemulsion method were comparable, or slightly improved. In a similar manner, Pd–Co catalysts of various compositions were prepared and tested for ORR activity by Rahul et al.<sup>252</sup> The Pd–Co catalysts were subjected to heat treatment in an oxygen-containing atmosphere that allowed oxides to form (denoted by OHT). On exposure to electrochemical conditions, the oxides were reduced in the potential range of 0.05–0.4 V, and the activity of the resulting ORR catalysts followed the order  $Pd \ll Pd_{1.5}Co < Pd_{6.3}Co < PdCo < Pd_2Co < Pd_3Co$ . Figure 34 depicts a comparison of ORR voltammograms of Pd, Pt,  $Pd_3Co$ , and  $Pd_3Co(OHT)$  catalysts recorded in oxygen-saturated 0.1 M  $HClO_4$  at a scan rate of 20 mV s<sup>-1</sup>.

Among the Pd-based catalysts, the  $Pd_3Co(OHT)$  catalyst was

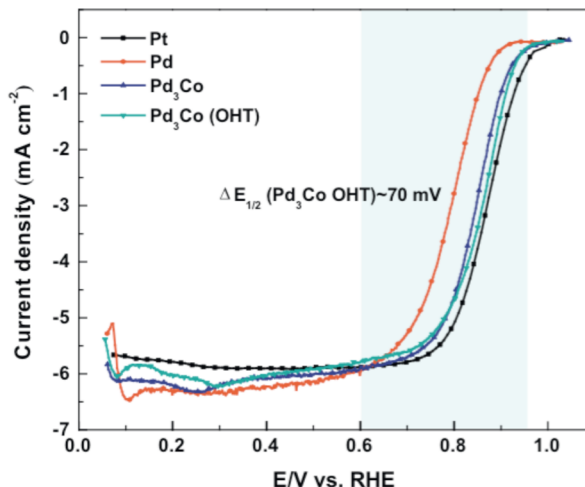


**Figure 34.** ORR voltammograms of as-prepared carbon-supported Pd, Pt,  $Pd_3Co$ , and  $Pd_3Co(OHT)$  catalysts in oxygen-saturated 0.1 M  $HClO_4$  at a scan rate of 20 mV s<sup>-1</sup> at 1600 rpm. Reprinted with permission from ref 252. Copyright 2014 Elsevier.

the closest to that of Pt. The increased activity of Pd–Co(OHT) catalysts may be attributed to changes in the degree of alloying, segregation of alloy components, particle composition changes, the formation of a chemically ordered alloy phase, and the larger dimensions of the Pd nanoparticles.

In summary, great progress has been made in the development of Pd-based ORR catalysts for alkaline and acidic fuel cells as a replacement for costly Pt-based materials. Coinciding with the intensive research efforts on the development of the ORR catalysts with a low precious metal loading, a new class of metal-free catalysts based on carbon materials has been discovered. A brief comparison of precious metal (Pt and Pd) based and metal-free catalysts for the ORR is presented in Table 2. It is worthy to note that activity discrepancies among Pd-based catalysts arise chiefly from their dependence on the synthesis methods and post-treatments, which define their properties. The work performed to date on ORR catalysts emphasizes the necessity to guide the design of more active Pd-based catalysts, which may consist of a large fraction of (100) facets, or Pd–M alloys for fuel cell applications.

### 3.4. Electrochemical Reduction of Hydrogen Peroxide

In low-temperature fuel cells, the typical anodic reaction is derived from either the direct oxidation of hydrogen or a hydrogen-containing fuel (e.g., methanol, ethanol, formic acid, or sodium borohydride), while the cathodic reaction normally involves the reduction of oxygen, as discussed in the previous section. However, the high overpotential of ORR reduces the efficacy of a fuel cell. Hydrogen peroxide ( $H_2O_2$ ) has received considerable attention for use as an alternative to  $O_2$ . The reduction of  $H_2O_2$  entails a two-electron transfer process, which allows for a fuel cell system to provide higher performance than systems that employ oxygen.<sup>37,143</sup> Precious metals, such as Pd, have shown high catalytic activity for the electrochemical reduction of  $H_2O_2$ ; however, further studies are necessary to fully assess the potential increases in fuel cell power density. Prepared electrocatalysts for the reduction of  $H_2O_2$  must provide excellent stability against corrosion and possess good electrical conductivity as required to minimize resistive loss. Although studies on electrocatalysts for  $H_2O_2$  reduction are sparse, cathodes such as Pd,<sup>253–255</sup> Pd–Ir,<sup>256</sup> Pd–Ag,<sup>257</sup> Pd–

Table 2. ORR Activity Comparison between Precious Metal and Metal-Free Catalysts<sup>a</sup>

catalyst		electrolyte	ORR onset potential (V) (Ag/AgCl)	ORR $E_{1/2}$ potential (V) (Ag/AgCl)	ref
Pt-based materials	Pt/C	0.1 M HClO <sub>4</sub>	0.713	0.503	181
	Pt/C	0.1 M NaOH	0.0674	-0.0906	242
	Pt/C	0.1 M KOH	-0.03	-0.075	358
	Pt/C	0.1 M KOH	-0.13	-0.40	359
	Pt/C	0.5 M H <sub>2</sub> SO <sub>4</sub>	0.663	0.623	45
	Pt/CP	0.5 M H <sub>2</sub> SO <sub>4</sub>	0.80	0.54	360
	Pt/CSC	0.5 M H <sub>2</sub> SO <sub>4</sub>	0.80	0.62	360
	Pt/CNF	0.5 M H <sub>2</sub> SO <sub>4</sub>	0.86	0.66	360
	Pt/CNT	0.5 M H <sub>2</sub> SO <sub>4</sub>	0.83	0.67	360
Pd-based materials	Pd bulk	0.05 M H <sub>2</sub> SO <sub>4</sub>	0.703	0.513	97
	Pd bulk	0.5 M H <sub>2</sub> SO <sub>4</sub>	0.713	0.523	45
	Pd bulk	0.1 M KOH	0.663	0.593	97
	Pd black	0.5 M H <sub>2</sub> SO <sub>4</sub>	-0.11	-0.15	164
	Pd/C	0.1 M KOH	-0.24	-0.3075	74
	Pd/C	0.1 M HClO <sub>4</sub>	0.673	0.455	181
	graphene-Pd	0.5 M H <sub>2</sub> SO <sub>4</sub>	-0.09	-0.14	164
	Pd/PPY	0.5 M H <sub>2</sub> SO <sub>4</sub>	0.643	0.361	153, 154
	PdPt (tetrapod)	0.5 M H <sub>2</sub> SO <sub>4</sub>	~1	0.583	82
metal-free catalysts	Pd <sub>3</sub> -Co	0.5 M H <sub>2</sub> SO <sub>4</sub>	0.543	0.451	91
	Pd <sub>2</sub> Co/carbon	0.1 M HClO <sub>4</sub>	0.751–0.801	0.641	120
	AuPd/C	0.1 M NaOH	0.0824	-0.0496	242
	Au@Pd	1 M KOH	-0.22	-0.303	74
	graphene-AuPd@Pd	0.5 M H <sub>2</sub> SO <sub>4</sub>	-0.01	-0.09	164
	N-doped CNT	0.1 M KOH	~0	-0.15	361
	N-doped CNT	0.5 M H <sub>2</sub> SO <sub>4</sub>	0.5	0.18	361
	N-doped CNC	0.1 M KOH	-0.13	-0.175	358
	B-doped CNT	0.1 M KOH	-0.133	-0.253	361
	graphene	0.1 M KOH	-0.15	-0.34	361
	N-doped graphene	0.1 M KOH	-0.017	-0.167	361
	B-doped graphene	0.1 M KOH	-0.13	-0.30	361
	BCN-doped graphene	0.1 M KOH		-0.203	361

<sup>a</sup>Abbreviations are as follows: CP = carbon paper, CSC = carbon sphere chain, CNF = carbon nanofiber, CNT = carbon nanotube, CNH = carbon nanohorn, CNC = carbon nanocage, RGO = reduced graphene oxide, PPY = polypyrrole. Reference electrode conversion equations: Ag/AgCl = NHE – 0.197 V; Ag/AgCl = SCE + 0.0474 V.

Co,<sup>258</sup> Pd–Ru,<sup>259</sup> Pd–Ni,<sup>260</sup> Pd–Pt,<sup>143,240</sup> and Pd–Au<sup>261,262</sup> have been explored.

Shim et al.<sup>240</sup> synthesized Pd and Pt nanoparticles and tested their activity for H<sub>2</sub>O<sub>2</sub> reduction under neutral conditions. Voltammogram comparisons for bulk Pt, Pt nanoparticles, and Pd nanoparticles are depicted in Figure 35A (based on geometric surface area) and Figure 35B (based on actual surface area). It may be seen that, for the case of bulk Pt,  $j_{GSA}$  did not achieve plateaus, which is indicative of sluggish H<sub>2</sub>O<sub>2</sub> oxidation/reduction, whereas, for Pt and Pd nanoparticles, well-defined anodic/cathodic limiting currents were obtained, suggesting good activity for the electrochemical reduction of H<sub>2</sub>O<sub>2</sub>. It was observed that Pd nanoparticles outperformed those composed of Pt, which was believed to be the result of their different microstructures (Pd having both nano- and microporosity vs Pt having nanoporosity only).

In general, noble metal catalysts were loaded onto carbon to form powder catalysts with increased stability. Dendritic Pd particles were reported by Yang et al.,<sup>254,263</sup> which were deposited onto carbon fiber cloth (CFC). The unique open dendritic structure of the electrodes allowed for the easy transportation of reactants to the catalyst and rapid removal of gaseous products, thereby increasing the catalytic activity and stability for the electrochemical reduction of H<sub>2</sub>O<sub>2</sub> in alkaline

and acidic media. Work by Yang et al.<sup>261,262</sup> focused on Pd and Au nanoparticles supported on CFC. Flower-like Au–Pd nanoparticles were electrodeposited on CFC at different molar ratios of 5:1, 2:1, 1:1, 1:2, and 1:5. The reduction of H<sub>2</sub>O<sub>2</sub> in a H<sub>2</sub>SO<sub>4</sub> solution was investigated, revealing that the catalytic performance was improved with increasing Pd content. The nanoflower-like surfaces of the Au–Pd/CFC electrodes exhibited excellent catalytic properties and good stability, which outperformed pure Au or Pd catalysts supported on CFC. Further work by this group explored structural variations toward the achievement of multifunctional catalytic properties through Au@Pd-decorated Pd nanodendrites. These novel open 3D structures exhibited far higher electrocatalytic activity than Pd/CFC in both acidic and alkaline media. This enhanced performance was believed to be the result of the decoration of the Pd surface by more electronegative Au, which promoted the adsorption of H<sub>2</sub>O<sub>2</sub> onto the catalytic surface. Although precious metals are commonly investigated for their high catalytic activity, their extensive utilization is limited by their high cost. Researchers such as Zhang et al.<sup>258</sup> have employed transition metals and their oxides (e.g., Co, Co<sub>3</sub>O<sub>4</sub>) as low-cost H<sub>2</sub>O<sub>2</sub> reduction catalysts. In their work, the prepared 3D paper substrate/graphite–Co film–Pd electrode provided high

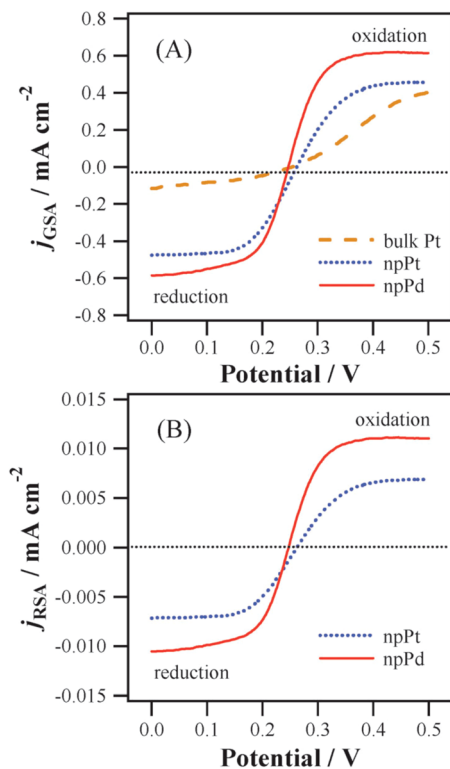


**Figure 35.** (A) RDE voltammograms based on  $j_{GSA}$  obtained with bulk Pt, Pt NPs, and Pd NPs in a deaerated 0.05 M PBS solution containing 1.0 mM  $H_2O_2$  (scan rate 1 mV s<sup>-1</sup>, rotation speed 100 rpm). (B) RDE voltammograms for Pt NPs and Pd NPs based on  $j_{RSA}$  corresponding to (A). Reprinted with permission from ref 240. Copyright 2012 Owner Societies.

electrocatalytic activity and superior stability in the electro-reduction of  $H_2O_2$ .

Due to the significant difference in energy required to break the single dioxygen bond of  $H_2O_2$  (146 kJ/mol) and the double bond of the  $O_2$  molecule (494 kJ/mol), the reduction of  $H_2O_2$  has a much lower activation barrier. Additionally, the reduction of  $H_2O_2$  at the cathode occurs at a solid/liquid interface, which provides more reliability than does a solid/liquid/gas three-phase region, which is typically seen for gas-diffusion electrodes.<sup>259</sup> In consideration of the above attributes, the use of  $H_2O_2$  as a fuel cell oxidant may provide a simpler route toward the commercialization of fuel cells with Pd-based catalysts, by providing a viable alternative to the costly Pt noble metal. Cathode performance is a key factor in selecting the particular application of a fuel cell, wherein the electrode material has a great impact on the electrochemical reaction rate in the electroreduction of  $H_2O_2$ .

### 3.5. Toward a Hydrogen Economy

Pd-based nanomaterials play a significant role in the purification and storage of hydrogen for fuel cell applications. The purification of hydrogen is essential for the performance of fuel cells since catalyst poisoning may occur at very low contaminant concentrations. Furthermore, the storage of hydrogen is essential if it is to be utilized as a source of energy for commercial applications. The unique properties of Pd, including its ability to absorb large volumetric quantities of hydrogen at room temperature under ambient atmospheric pressure, with the subsequent formation of palladium hydride

( $PdH_x$ ), make it an ideal candidate for hydrogen fuel cell applications.

**3.5.1. Hydrogen Production and Purification.** The production of hydrogen may be achieved by several means from logical sources, such as hydrocarbon fuel or water. Currently, the majority of  $H_2$  is produced via thermochemical methods by processing hydrocarbons such as natural gas, coal, biomass, or wastes to produce “syngas” composed of  $H_2$ , CO,  $CO_2$ ,  $H_2O$ , and  $CH_4$ . Through the environmentally and energy taxing process of gas reforming, the desired content of pure hydrogen may be achieved. By augmenting the production of hydrogen with more renewable and environmentally compatible resources, the ecological repercussions of gas reforming can be mitigated.

Hydrogen can be easily generated from water by electrolysis, a process that uses electricity to break the bonds between the constituent elements of water, and releases them as gas. However, presently only a small percentage (ca. 4%) of global hydrogen production is attained through water electrolysis.<sup>224,264,265</sup> Challenges for widespread applications of hydrogen production using water electrolysis require significant improvements in energy efficiency, safety, durability, operability, portability, and, above all, operational cost reduction.<sup>264,266</sup> Historically, Pd was the first metal to be identified as having a high capacity for hydrogen absorption. It has the ability to absorb large quantities of hydrogen not only from the gas phase, but from electrolytes as well. When hydrogen is electrochemically absorbed, the  $H^+$  ions occupy the octahedral voids within the Pd crystal lattice to form nonstoichiometric  $PdH_x$ . The unique properties of Pd-based nanomaterials promise low overpotentials and high reversibility that promotes the clean generation of sustainable energy.<sup>72,266–268</sup>

The production of hydrogen from inexpensive and renewable resources is essential for the application of  $H_2$  energy under real world conditions. As well, a high-purity gas stream is crucial for the performance of a hydrogen fuel cell as certain species may poison the catalysts at very low concentrations.<sup>6</sup> An inherent affinity and selectivity for hydrogen, rapid sorption kinetics, and hydride formation reversibility enable Pd-based materials to achieve an excellent hydrogen gas quality of up to 99.99999% purity. The adsorption of hydrogen into bulk Pd occurs via two distinct  $\alpha$ - and  $\beta$ -phases. The  $\alpha$ -phase occurs at low concentrations of hydrogen (solid solution of hydrogen in Pd), for which the atomic ratio of H to Pd is typically below 0.03–0.05 at room temperature, whereas the  $\beta$ -phase forms at high concentrations of hydride (metal hydride), corresponding to a H/Pd ratio above ca. 0.6. The schematic phase diagram for  $PdH_x$  is displayed in Figure 36 with superimposed isotherms (solid red lines). The area located inside the inverted parabolic phase boundary represents the region of coexistence between the dilute  $\alpha$ -phase and the concentrated  $\beta$ -phase. A critical temperature,  $T_c = 570$  K, exists as the maximum temperature at which the  $\alpha$ - and  $\beta$ -phases may coexist.<sup>269</sup>

Toward the improvement of current commercial hydrogen purification and production processes, membrane-based separation strategies have been implemented. Metallic separation membranes based on Pd offer the ability to dissociate molecular hydrogen into monatomic form, which is amenable for rapid diffusion through their lattices.<sup>265</sup> The major shortcoming of pure Pd membranes is hydrogen embrittlement, which causes the cracking of membranes due to the expansion of the face-centered cubic crystal lattice that is associated with the  $\alpha/\beta$  phase transition. Modifications, such as nanoscale preparation,

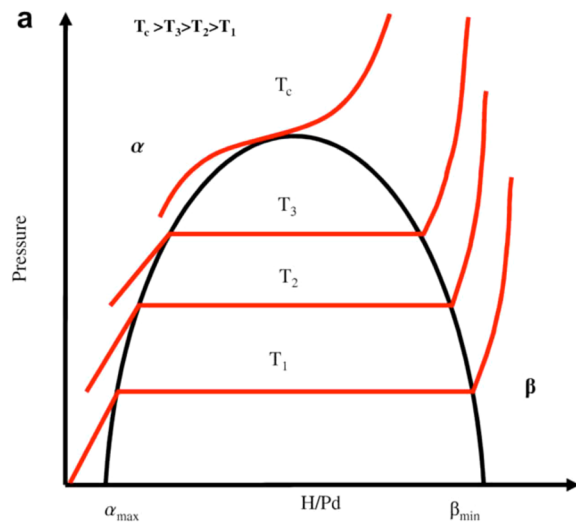


**Figure 36.** Schematic of the phase diagram for bulk  $\text{PdH}_x$  with superimposed isotherms (solid red lines). Reprinted with permission from ref 269. Copyright 2008 Elsevier.

the alloying of Pd with metals of larger atomic sizes, and the deposition of Pd membranes on a porous substrate to form composite membranes, have been shown to decrease embrittlement.<sup>72,270–273</sup>

PdAg is the most commonly used hydrogen extraction metal in industry, where the alloying of Pd with Ag lowers the  $T_c$  of the miscibility gap, which eliminates the requirement of purging hydrogen from the membrane prior to thermal cycling.<sup>263,274</sup> However, PdAg catalysts exhibit short life cycles due to substantial lattice expansion upon hydrogen adsorption and undergo coarsening at high temperatures. As substitutes, alloys such as PdY<sup>275</sup> and PdCu<sup>276,277</sup> have been proposed, which offer mechanical superiority in durability and stability. Work on phase transition and lattice expansion during hydrogen loading of nanometric Pd clusters suggests that lattice dilation strongly depends on the hydrogen partial pressure and cluster size.<sup>278</sup> Unconventional alloys, such as PdCd, have been investigated and verified that the  $\alpha$ - to  $\beta$ -phase transition may be practically eliminated when an optimal foreign atom is employed as a dopant.<sup>72</sup> As shown in Figure 37, the  $\text{H}/(\text{Pd} + \text{Cd})$  ratio strongly depended on the applied electrode potential and the composition of the PdCd alloys. The maximum  $\text{H}/(\text{Pd} + \text{Cd})$  ratio was found to be the highest for pure Pd (0.66), but the ratio decreased with an increasing amount of Cd. Two distinct phases ( $\alpha$  and  $\beta$ ), with a sharp phase transition between  $-225$  and  $-250$  mV, were observed for pure Pd; however, this phase transition was diminished with increasing amounts of Cd. In particular, the compositions of PdCd alloys with a higher Cd content (i.e., 10 and 15 atom %) displayed minimal phase transition, and were capable of electrosorbing much more hydrogen at higher potentials (in the  $\alpha$  phase) than pure Pd.

As an alternative to the electrolysis of water or gas reforming, formic acid electrolysis has been suggested for pure hydrogen production.<sup>217,279</sup> Formic acid possesses a lower decomposition energy ( $\Delta H \approx 32 \text{ kJ mol}^{-1}$ ) compared to that required for water decomposition ( $\Delta H \approx 286 \text{ kJ mol}^{-1}$ ) under standard conditions. However, relatively slow kinetics within the anodic reaction for both processes leads to high anodic overvoltages (Figure 38), which need to be decreased to acceptable values by means of electrocatalyst development. Lamy et al.<sup>217</sup> produced several Pd-based catalysts dispersed on a Vulcan XC-72 carbon

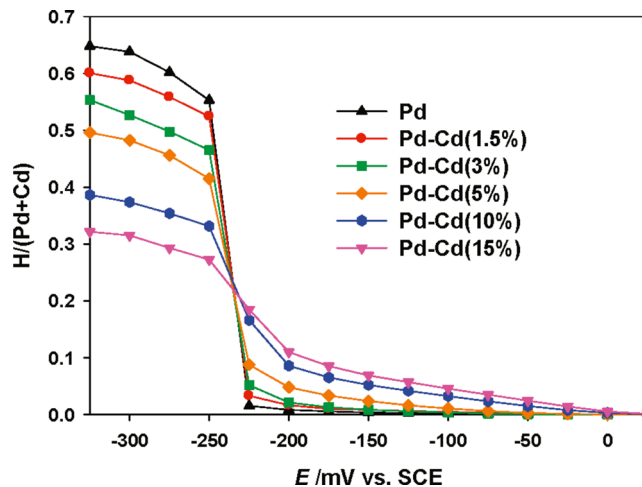


**Figure 37.**  $\text{H}/(\text{Pd} + \text{Cd})$  ratio versus the potential for Pd–Cd nanostructures with various compositions as indicated in the figure. Reprinted from ref 72. Copyright 2010 American Chemical Society.

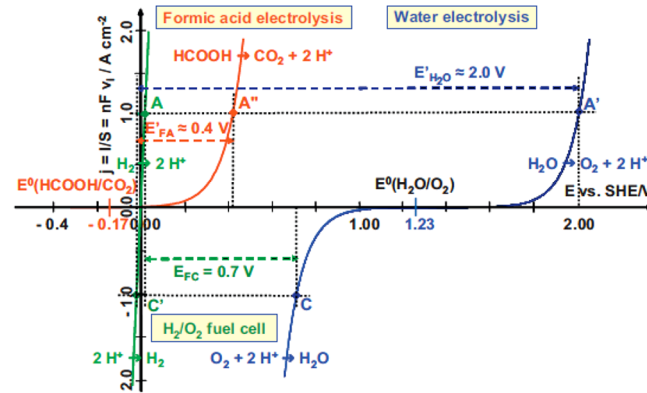


**Figure 38.** Comparison of the theoretical  $E(j)$  electronic characteristics representative of the Butler–Volmer kinetics law for water oxidation, acid formic oxidation, oxygen reduction, and proton reduction.  $E_{\text{H}_2\text{O}}$ ,  $E_{\text{FA}}$ , and  $E_{\text{FC}}$  are the cell voltages for water electrolysis, formic acid electrolysis, and the hydrogen/oxygen fuel cell at a current density of  $1 \text{ A cm}^{-2}$ , respectively.  $E^{\circ}(\text{H}_2\text{O}/\text{O}_2) = 1.23 \text{ V}$  (vs SHE) and  $E^{\circ}(\text{HCOOH}/\text{CO}_2) = -0.17 \text{ V}$  (vs SHE) are the electrochemical reaction standard potentials. Reprinted with permission from ref 217. Copyright 2011 Elsevier.

support (Pd/C,  $\text{Pd}_{x}\text{Au}_{1-x}/\text{C}$ ,  $\text{Pd}_{x}\text{Pt}_{1-x}/\text{C}$ ) and tested their electrochemical activity for the electrooxidation of formic acid to generate clean hydrogen. The Pd-based catalysts offered stable activity with only mild CO poisoning for the anodic oxidation of formic acid, with more than two-thirds of the electrical energy being conserved, in comparison to water decomposition. In a similar fashion, Jia et al.<sup>279</sup> fabricated Pd/C catalysts modified with potassium carbonate for the decomposition of formic acid. A sample containing 10 wt % K had a hydrogen production capacity that was practically free of CO (<30 ppm), with a steady-state turnover frequency at 353 K, which was 65 times higher than that of an undoped material.

**3.5.2. Hydrogen Storage.** One of the restrictions on the generation of electricity via renewable power is that the output requires either immediate use or storage. Through the generation of hydrogen via renewable resources, produced electricity has the potential to be stored and distributed. It is recognized that energy storage is a critical aspect of a hydrogen

system; however, combating hydrogen's poor energy density by volume comes as a challenge.<sup>280</sup> Pd offers a possible solution through the provision of a lightweight material with excellent adsorption kinetics and desorption with acceptable recyclability. Nonetheless, the extensive use of Pd for hydrogen storage currently remains impractical, due to its relatively high expense. Conversely, cost-saving measures, such as alloying with less expensive metals and utilizing nanoscale materials, might serve to offset this drawback.

Kishore et al.<sup>267</sup> investigated the possible benefits of hydrogen storage in nanoparticulate matter with different morphologies (e.g., platelets and spherical). The Pd nanoparticles exhibited an increase in hydrogen uptake of the  $\alpha$ -phase relative to bulk Pd. Similar to the effects imparted via morphology, the interactions between hydrogen and Pd change as the nanoparticle dimensions are altered. Kobayashi et al.<sup>268</sup> investigated the nature of hydrogen trapping within Pd nanoparticles versus that of bulk Pd. Their results concluded that hydrogen atoms became strongly trapped and stabilized within the Pd nanoparticle lattice, resulting in the incomplete recovery of pressure–composition (PC) isotherms. Work by Yamauchi et al.<sup>281</sup> also focused on the nanoscale effects of the storage of hydrogen in Pd. A clear size dependence of the hydrogen PC isotherms for Pd nanoparticles was demonstrated, which implied that the storage properties of metals might be tailored by changing their physical dimensions. It was demonstrated that hydrogen atoms were highly concentrated within Pd nanoparticles that had diameters of only a few nanometers.

The primary drawback of metal nanoparticles pertains to their aggregation during use, which results in the reduction of catalytic activity and capacity of hydrogen sorption. Overcoming this challenge may be possible through the preparation of metal nanoparticles on support materials. Carbon-based materials are among the most commonly used metal supports for hydrogen storage;<sup>83,142,282–289</sup> however, supports such as TiO<sub>2</sub> NTs<sup>290</sup> and metal organic frameworks (MOFs)<sup>291,292</sup> have also been noted. Campesi et al.<sup>284</sup> successfully synthesized nanometric Pd clusters, which were homogeneously dispersed among the pores of an ordered mesoporous carbon template. The carbon template allowed for the realization of a composite with structurally ordered, size-controlled, and well-dispersed Pd clusters to be obtained. At room temperature, the synergy between Pd and the carbon network gave rise to improved hydrogen sorption.

Conventionally, the hydrogen storage capacity of pristine carbon nanomaterials such as CNTs,<sup>287</sup> graphene,<sup>142,285,289</sup> activated carbon fibers (ACFs),<sup>286,293</sup> etc. is rather low. The functionalization of the surfaces of these materials with Pd, however, significantly increases their hydrogen storage capacities.<sup>142,285,289,294–296</sup> In work by Ma et al.,<sup>294</sup> DFT was employed to investigate the hydrogen storage behavior of Pd-decorated nitrogen-doped graphene. Pyridinic and pyrrolic N-doped defects resulted in increased stability and exhibited a hydrogen uptake capacity of up to three H<sub>2</sub> molecules per Pd atom. A single H<sub>2</sub> molecule or two H<sub>2</sub> molecules were molecularly chemisorbed on Pd, while the third absorbed H<sub>2</sub> molecule remained very weakly physisorbed. In related work by Rangel et al.,<sup>295</sup> Pd clusters supported on pyridine-like nitrogen-doped graphene behaved in a fashion similar to that of the hydrogen storage behavior seen in the work of Ma,<sup>294</sup> where the third weakly bound H<sub>2</sub> molecule could potentially diffuse as a hydrogen atom to the graphene support.

The enhancement of hydrogen storage on carbon-based materials has well been documented under the phenomenon termed "hydrogen spillover",<sup>138,144,288,293,297,298</sup> wherein the mechanism occurs as follows: (i) H<sub>2</sub> molecules dissociate on the metal catalyst particles, (ii) H atoms migrate from the metal catalyst nanoparticles to the carbon substrate materials, and (iii) H atoms diffuse across the substrate. To assess the effect of hydrogen spillover, one may simply compare the hydrogen capacity of a combined system (carbon + metal) with that of the individual components.<sup>288</sup> With respect to hydrogen spillover, the use of Pd catalysts increases the potential for the capacity to be higher than that of other nonabsorbing metals, due to its ability to store hydrogen within the catalyst itself.

The hydrogen sorption properties of three Pd-based hydrogen dissociation catalysts (Pd, Pd<sub>0.77</sub>Ag<sub>0.23</sub>, and Pd<sub>0.85</sub>Cd<sub>0.15</sub>) were examined by Adams et al.<sup>138</sup> at room temperature, which were dispersed on activated carbon materials. At room temperature, hydrogen spillover was observed to proceed from the catalyst to the carbon material, as displayed in the hydrogen adsorption isotherms (Figure 39a). It was assumed that, in the absence of spillover hydrogen, at any given pressure, the volumetric hydrogen capacity of the metal dispersed on the carbon materials could be calculated as a combination of the capacities of the metal particulates and that

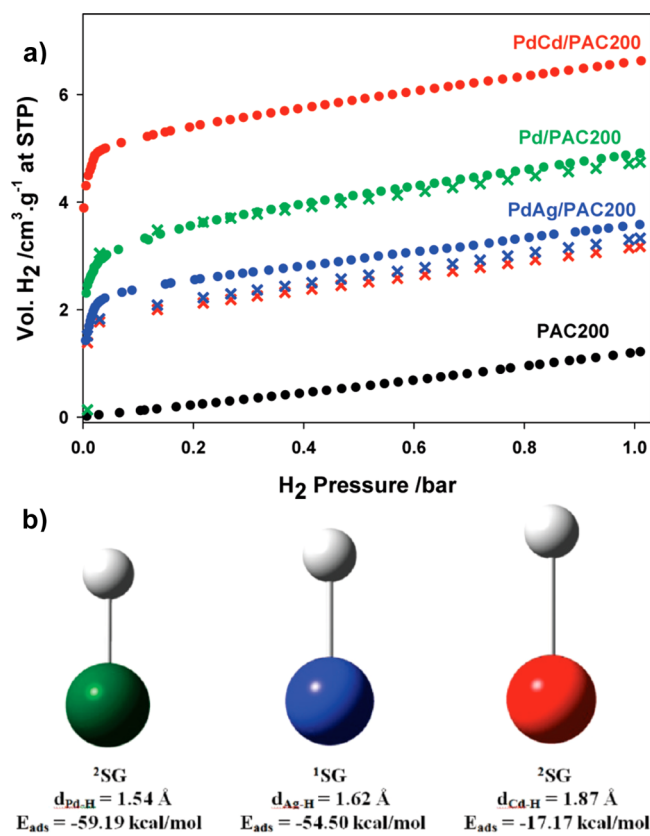


**Figure 39.** (a) Hydrogen adsorption isotherms at room temperature ( $295 \pm 2$  K) for the PAC200, Pd/PAC200, PdCd/PAC200, and PdAg/PAC200 samples. Calculated isotherms are shown with times signs, and experimental isotherms are shown with dots. (b) Optimized molecular geometries and adsorption energies for Pd–H, Ag–H, and Cd–H calculated using DFT. The H atoms are shown in white, Pd atoms in green, Ag atoms in blue, and Cd atoms in red. Adapted from ref 138. Copyright 2010 American Chemical Society.

of PAC200 carbon. In Figure 39a, the calculated isotherms, with the assumption of no hydrogen spillover, are depicted with times signs. To understand the variations in the enhancement of hydrogen capacity for each metal, optimized molecular geometries of the M–H models and corresponding M–H bond distances and adsorption energies were calculated (Figure 39b). The less energetically demanding Cd atoms, in contrast to Pd or Ag, resulted in a much higher spillover enhancement of the PdCd nanoparticles at room temperature. This signified that the nature of hydrogen spillover enhancement is electronic in nature, rather than geometric.

It is understood that hydrogen spillover occurs exclusively in the gas phase, although similar enhancements of dispersed metals on carbon supports have been noted in electrochemical experiments. In our recent work,<sup>299</sup> we focused on activated carbon materials that were modified with different Pd–Ag–Cd trimetallic dissociation catalysts for hydrogen electrosorption at ambient temperatures. The overall hydrogen oxidation/desorption charges ( $Q_H$ ) for each Pd-based PAC200 nanoparticle at different held potentials are displayed in Figure 40a. An atomic percentage of Ag equal to that of Cd, as seen in the PdAg<sub>10</sub>Cd<sub>10</sub> sample, gave rise to the highest  $Q_H$ , indicating improved hydrogen sorption capabilities. We observed a significant synergistic effect on hydrogen storage when comparing the capacity of the supported and nonsupported PdAgCd catalysts (Figure 40b), which may be attributed to the initial electrochemical reduction of hydrogen ions at the Pd-based nanoparticles and the hydrogen surface diffusion subsequent to the activated carbon. Further assessment of the level of enhancement due to the synergistic effect between the PdAg<sub>10</sub>Cd<sub>10</sub> nanoparticles and the activated carbon is displayed in Figure 40c. The corresponding  $Q_{H,\text{supported}}/Q_{H,\text{nonsupported}}$  ratios for the PdAg<sub>10</sub>Cd<sub>10</sub> revealed that the dispersal of the PdAg<sub>10</sub>Cd<sub>10</sub> catalyst onto the surface of the PAC200 was an important factor in facilitating the improved hydrogen storage.

The importance of hydrogen fuel has been recognized and is gaining significance as the extensive use of fossil fuels has accelerated their inevitable depletion. The generation of clean hydrogen offers the potential for non-carbon-based energy systems, which may replace fossil fuels. However, robust and stable catalysts for the production of pure hydrogen from renewable resources are required. Pd-based materials offer a combination of hydrogen production and storage with reasonable adsorption/desorption kinetics. It is suggested that future studies focus on understanding the activity enhancement that allows for the exploitation of the adsorption strengths and hydrogen dissociation properties of Pd-based materials, as well as countermeasures to negate the effects of poisoning species in hydrogen purification processes and hydrogen storage materials.

### 3.6. Gas Sensors

Gas sensors may be employed to identify the presence of a gas, or to measure its concentration. In the case of electrochemical gas sensors, the oxidation or reduction of a target gas with a sensing electrode may lead to changes in charge transport or electrical properties. A transducer is then employed to transform the resulting changes into an electrical signal. Typically, transition metals are employed to modify the selectivity of sensors, which exploit the binding properties of target molecules. The use of Pd in the detection of hydrogen is prevalent among other transition metals; it also demonstrates

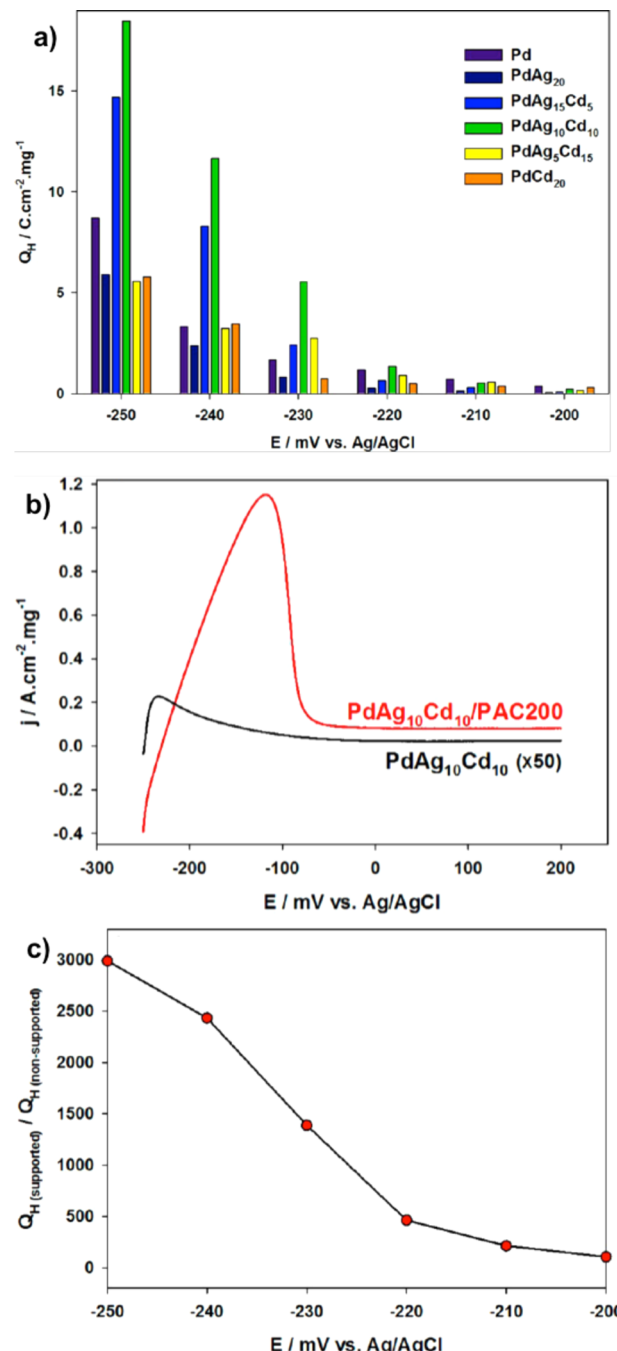


**Figure 40.** (a) Overall hydrogen oxidation charges ( $Q_H$ ) for each Pd-based catalyst at various cathodic limits. (b) Anodic sweeps of PdAg<sub>10</sub>Cd<sub>10</sub> nanoparticles with and without the PAC200 support after the potential was held at  $-250\text{ mV}$  for 1 min in  $0.5\text{ M H}_2\text{SO}_4$  recorded at a scan rate of  $5\text{ mV s}^{-1}$ . Note that the PdAg<sub>10</sub>Cd<sub>10</sub> nonsupported sample current density ( $j$ ) is multiplied by a factor of 50 for viewing purposes. (c) Corresponding ratios of charge due to hydrogen desorption versus potential. Adapted from ref 299. Copyright 2013 American Chemical Society.

applications toward hydrocarbon and volatile organic compounds.<sup>300,301</sup>

Electrochemical hydrogen sensors operate on the basis of transducer devices that detect hydrogen gas molecules to subsequently produce electrical signals with magnitudes that are proportional to hydrogen concentrations. The selectivity of the sensor to hydrogen is essential for the reduction of cross

sensitivity in hydrogen sensors. Palladium's high affinity for hydrogen marks it as a valuable element on the basis of specific catalytic reactivity and solubility toward hydrogen selectivity. However, the extensive use of Pd for hydrogen detection is restricted by its susceptibility to mechanical damage on exposure to hydrogen.

Gupta et al.<sup>302</sup> synthesized ~10 nm Pd nanoparticles for hydrogen sensing to enable a higher response gained from an increase in catalytic surface area within a fixed geometry. For hydrogen sensor applications, lower device detection limits are critical, with the highest concentration of hydrogen not exceeding 1%. At the nanoscale, Gupta and co-workers were able to achieve reproducible and stable hydrogen sensing at significantly low temperatures (35–75 °C). Similar work on size and morphology adaptations have been reported by researchers such as Noh et al.,<sup>303</sup> Zeng et al.,<sup>51</sup> Villanueva et al.,<sup>114</sup> Phan et al.,<sup>304</sup> and Pan et al.,<sup>305</sup> some of which we will expand on below.

An interesting property of Pd is its increased resistivity on hydrogen adsorption, due to the formation of  $\text{PdH}_x$ . A schematic representation of the interface between two Pd nanoparticles prior to and following hydrogen exposure is displayed in Figure 41. Prior to the introduction of hydrogen, a

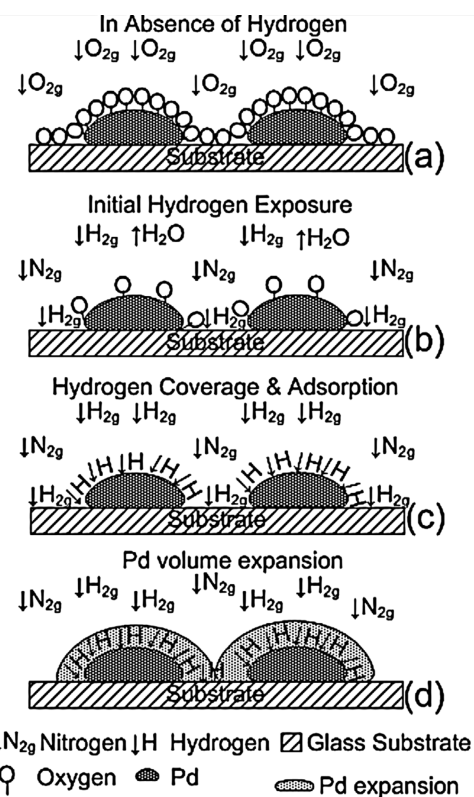


**Figure 41.** Hydrogen sensing mechanism of the palladium nanoparticle sensor. Reprinted with permission from ref 302. Copyright 2014 Elsevier.

layer of charged spilled-over oxygen species covers the surface of Pd, as well as the interface between the two Pd nanoparticles. Once exposed to hydrogen, the oxygen species are slowly removed from the surface by water formation, leaving behind vacant adsorption sites. The vacant surface sites then proceed to fill with hydrogen, leading to the formation of  $\text{PdH}_x$  and the increased resistivity of individual Pd nanoparticles. The Pd

volume expansion, due to hydrogen adsorption, then initiates a drop in resistance, and thus, a variation in resistance is revealed in the transient response.<sup>302</sup>

The effects of the dimensions of the Pd nanocubes comprising Pd nanocube–graphene hybrid electrodes on the hydrogen sensing properties were investigated by Phan et al.<sup>304</sup> A comparison of the response repeatability of the prepared relative resistivity of  $\text{H}_2$  sensors in three testing cycles is shown in Figure 42a, commencing with 10000 ppm  $\text{H}_2$  at room

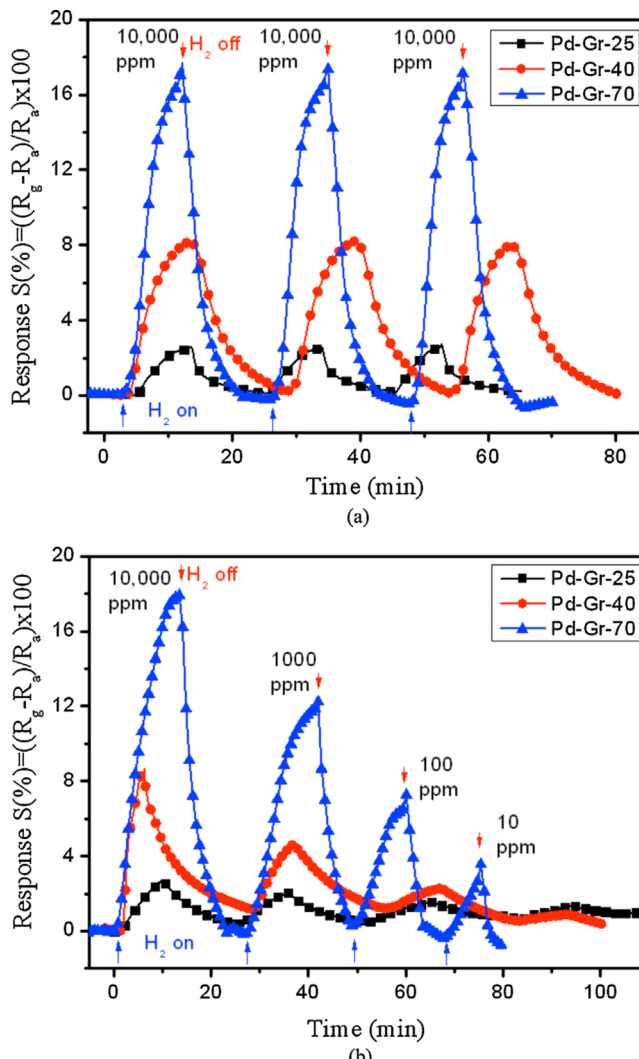


**Figure 42.** Responses of the Pd nanocube–graphene hybrid exposed to (a) 10000 ppm of  $\text{H}_2$  and (b)  $\text{H}_2$  of various concentrations at room temperature. Reprinted with permission from ref 304. Copyright 2014 Elsevier.

temperature, followed by exposure to different  $\text{H}_2$  concentrations, ranging from 10000 to 10 ppm in Figure 42b. The highly uniformly sized 25, 40, 55, 70, and 85 nm Pd nanocubes exhibited good linear responses to  $\text{H}_2$  of 10 and 10000 ppm at room temperature. The response of the  $\text{H}_2$  sensor increased linearly with increasing size of the nanocubes.

In an emerging hydrogen economy, the accurate detection of hydrogen leaks and the measurement of hydrogen concentrations are necessary during production, storage, transportation, and use in both stationary and mobile applications. Nanowires have demonstrated interesting characteristics, such

as high surface-to-volume ratios, ultrasensitivity, enhanced selectivity, low power consumption, and rapid response times.<sup>115,306,307</sup> Gas sensors based on precious metal nanowires such as Pd have been developed and studied by Zeng et al.,<sup>51</sup> who reported on the suitable preparation of H<sub>2</sub> sensors based on networks of ultrasmall (<10 nm) Pd nanowires that were deposited on commercially available filter membranes. The fabricated hydrogen sensor exhibited high sensitivity and rapid response times. However, the resistance change at saturated H<sub>2</sub> concentrations (>3%) proved to seriously hinder the applications. It was proposed that, by replacing pure Pd with Pd alloys, this limitation might be eliminated. Work of this nature was explored by Yang et al.,<sup>115</sup> who revealed that alloyed materials for hydrogen sensor applications exhibited enhanced response and recovery times, along with improved stability.

The application of Pd as a sensor for the detection of hydrocarbons<sup>308–312</sup> and volatile organic compounds<sup>224,313</sup> has not been investigated as extensively as for hydrogen sensors. However, recent interest has been sparked due to the incessant need for gas detection instruments for applications in industrial health and safety, environmental monitoring, and process control. Carbon monoxide (CO) remains a danger in urban environments and for indoor air, as a potentially fatal pollutant, which is produced by the incomplete combustion of organic substances where there is an O<sub>2</sub> deficiency. It is a colorless, tasteless, and odorless gas that requires detection to negate the likelihood of poisoning. With respect to CO detection, the use of Pd as a detection catalyst exploits the binding properties of CO with transition metals. Enhanced CO sensing with Pd has been developed by Rai et al.,<sup>314</sup> who demonstrated both the augmented electronic and chemical interactions with species at Pd surfaces. With regard to electronic contributions, Pd nanoparticles serve as electron acceptors that contribute to an increased depletion layer. From the chemical interaction perspective, Pd catalytically activates the dissociation of molecular oxygen, which accumulates the quantity of oxygen that may react with CO, causing an increased change in resistance to produce an enhanced sensor response.

Further studies into the catalytic applications of Pd for H<sub>2</sub>, hydrocarbon, and volatile organic compound detection are likely to result in the development of highly sensitive, rapid-response, and low-cost sensing materials. To meet future demands in the development of gas sensors (more notably with respect to hydrogen sensors), continued research will be required toward further improvements in sensitivity, selectivity, response times, reduced size, cost, reliability, and power consumption.

### 3.7. Electrochemical Biosensors

Over the past five decades, efforts have been focused on the development of enzyme-based biosensors that exhibit highly sensitive performance. However, their universal application is hindered by drawbacks including complex enzyme immobilization and stabilization, easy environmental enzyme activity degradation (e.g., via temperature, pH, humidity, toxic chemicals, etc.), and high enzyme expense,<sup>135</sup> yet nonenzymatic biosensors offer several advantages, including high stability and ease of fabrication. In recent years, Pd-based nanomaterials have often been selected for the modification of biosensor electrodes, as they are electrocatalytically active, resistant to oxidation, and relatively inexpensive.

Glucose sensing is required for the controlled monitoring of glucose levels both in blood and from sources such as foods and

pharmaceuticals. Commercial glucose sensors rely on general electrochemical enzymatic techniques, which are based on the sensitive and selective reaction between glucose oxidase enzymes and glucose. Hindrances produced through the use of enzymes have created an increased demand for new techniques that will allow for continuous and noninvasive glucose monitoring, with high accuracy at low cost. Fortunately, Pd exhibits long-term stability for glucose sensing, resulting from the weak adsorption of endogenous interfering species during the oxidation process.<sup>4,38,135,315</sup>

Pd composites, known for their high electrocatalytic activity, exhibit superior performance for the determination of H<sub>2</sub>O<sub>2</sub>.<sup>316–319</sup> H<sub>2</sub>O<sub>2</sub> is employed extensively as an oxidizing agent in the chemical and food industries and is an important marker for oxidative stress, acting as a precursor in the formation of highly reactive and potentially harmful hydroxyl radicals. The precise monitoring of H<sub>2</sub>O<sub>2</sub> is of practical significance in biomedical and environmental applications. Similar detection enhancements on Pd have been demonstrated for additional biomedical analytes, including dopamine (DA), uric acid (UA), and ascorbic acid (AA).<sup>315,320–322</sup>

To address concerns related to catalytic activity, research has focused on the use of carbon materials as supports to augment electron transfer and increase surface area. In addition to the aforementioned traits, carbon support materials such as graphene and CNTs are the most widely used in chemical and biological sensing applications, due to their capacity for analyte accumulation and rapid alleviation of surface fouling.<sup>89,135,149,316,317,320,323</sup> As an example, Liu et al.<sup>316</sup> embedded Pd nanoparticles within graphene nanosheets, which were investigated as a nonenzymatic electrochemical sensor for the detection of H<sub>2</sub>O<sub>2</sub>. The negatively charged Pd surface atoms favored the H<sub>2</sub>O<sub>2</sub> reduction process, where contact between the Pd nanoparticles and graphene sheets allowed for a remarkable decrease in the overpotential and enhanced the electron transfer rate.

Further improvements in electrochemical detection sensitivities will require the assembly of enhanced electrode materials. Chen et al.<sup>324</sup> prepared Pd nanoparticles deposited on functional carbon nanotubes (FCNTs) modified with Nafion, which were examined for their high electrocatalytic activity and stability for the determination of glucose. The CV behaviors of the nanostructured electrodes in the presence of 0.1 mM AA and 1.0 mM glucose in 0.1 M NaOH, containing 0.2 M NaCl, revealed that the current density peak at 0.45 V of glucose was 5-fold higher than that of AA (Figure 43). This demonstrated the ability of the Pd catalyst to circumvent the interfering signals contributed by AA. The inset in Figure 43 depicts the amperometric response on the Pd–FCNT–Nafion-modified electrodes with successive additions of UA, AA, acetamidophenol (AP), and glucose. It can be seen that glucose generated significant signals in comparison to the other three interfering species, which indicated that glucose detection on Pd–FCNT–Nafion-modified electrodes could be performed with negligible interference. In a similar manner, Lu et al.<sup>325</sup> produced Pd-functionalized graphene (Nafion–graphene) for the detection of glucose. The Nafion–graphene–Pd nanocomposite exhibited a rapid response time as well as excellent selectivity for glucose in the presence of interfering species. Composite nanomaterials provide potentially larger electrochemically active surface areas for the adsorption of target molecules, and effectively accelerate electron transfer between the electrode and detection molecules. This increase in electron

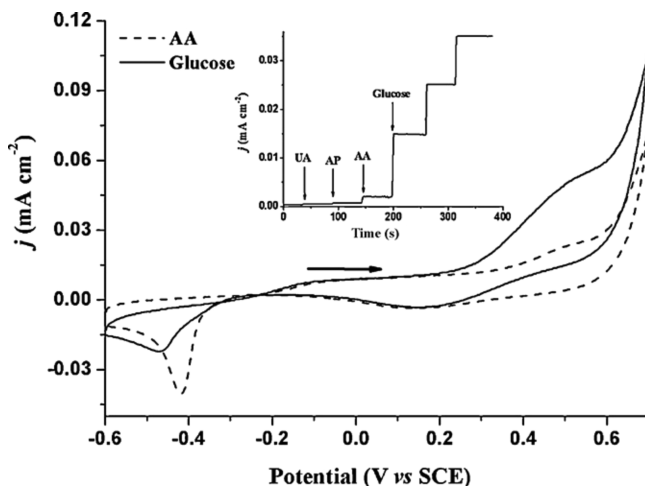


**Figure 43.** CV curves of the Pd NP-FCNT-Nafion electrode in glucose (solid line) and AA (dashed line) solutions. The inset shows chronoamperometry curves of the Pd NP-FCNT-Nafion electrode with the successive addition of 0.02 mM UA, 0.1 mM AP, 0.1 mM AA, and 1.0 mM glucose.  $[\text{NaCl}] = 0.2 \text{ M}$ , and  $[\text{NaOH}] = 0.1 \text{ M}$ . Reprinted with permission from ref 324. Copyright 2010 Elsevier.

transfer results in a more rapid and sensitive current response.<sup>89,324–327</sup>

Continued efforts in the development of biosensors based on bare metal surfaces have reinforced the importance of the control of catalyst morphologies. This was demonstrated by Ye et al.<sup>149</sup> through the fabrication of Pd nanocubes that were enclosed by (100) planes for the oxidation of glucose. A comparison of the specific surface activities, in terms of electrochemical real surface area between Pd(100) nanocubes and Pd nanoparticles dominated by (111) planes, revealed a higher oxidation power of the anodic glucose oxidation process, which was catalyzed by the (100) planes of the nanocubes. However, most pure metals exhibit an unsatisfactory sensitivity to glucose.

Recently, bimetallic-based catalysts have been developed to enhance the sensitivity and selectivity of sensors.<sup>75,318,321,328</sup> Intermetallic combinations of different metals have been observed to bring about interesting physical and chemical properties, which culminated in increasing overall catalyst activity. Catalysts comprised of Pd–Ni, which were synthesized by Zhang et al.,<sup>321</sup> exhibited improved electrochemical sensing that boasted excellent synergistic effects, which enabled high sensitivity, selectivity, and stability for the detection of AA. Alloying Ni with Pd altered the electronic structure in favor of increased electron transfer to provide stability for the minimization of poisoning effects. Ahmadalinezhad et al.<sup>75</sup> incorporated Cd into nanoporous Pd networks to produce a glucose sensor with improved sensitivity. The amperometric response of the PdCd electrode to the interferents in the presence of 3 mM glucose is depicted in Figure 44 for the PdCd electrode. This increased sensitivity may be attributed to the extensive surface area of nanoporous PdCd, in conjunction with the high electrochemical activity of the binary nanostructured system. A few other bimetallic-based catalysts such as PdFe<sup>318</sup> and PdCu<sup>83</sup> have been investigated. However, it is apparent that if nonenzymatic biosensors are to be applied for consumer applications, increased efforts in the area of bimetallic-based sensors will be required to overcome the obstacle of selectivity and high costs.

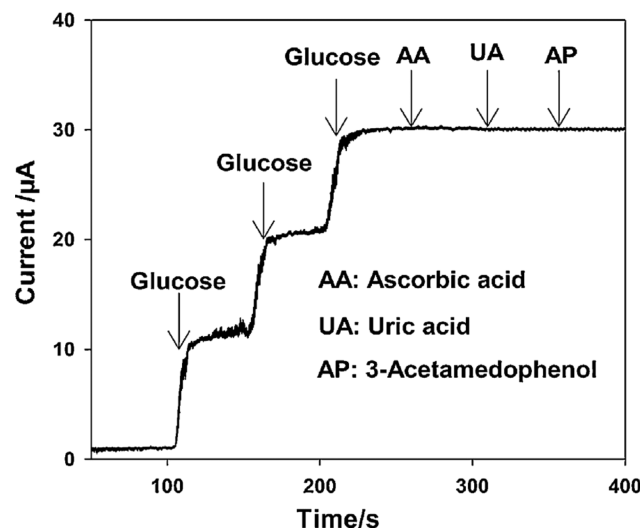


**Figure 44.** Effect of interferents, 0.1 mM ascorbic acid (AA), 0.1 mM acetaminophen, and 0.02 mM uric acid (UA), on the response of the Pd–Cd/GC electrode in the presence of glucose in PBS solution (pH 7) at  $-0.4 \text{ V}$ . Reprinted with permission from ref 75. Copyright 2013 Elsevier.

Analytical sensing devices offer advantages for the detection of various targets which have critical significance in many aspects of environmental pollution, human health, and food safety. They allow for the benefits of onsite, real-time qualitative or semiquantitative detection without the necessity of complicated analytical instrumentation. Challenges include the lack of scalable production and difficulties with the production of monodispersed Pd nanomaterials (which are rich in high-index facets), leaving room for material improvement. Major motivations for improved sensor design encompass the achievement of higher sensitivity, selectivity, speed, stability, reliability, and accuracy.

### 3.8. Other Applications

In addition to the key electrocatalytic roles that Pd facilitates in fuel cells, glucose sensors, and gas sensors, Pd catalysts are garnering additional attention for their use as electrochemical capacitors, as well as in wastewater treatment. These applications are mainly due to the abilities of Pd nanoparticles for hydrogen adsorption and highly efficient electrocatalysis.

The emergence of supercapacitors that exhibit high-capacitance and high-power characteristics have intensively followed the development of two types of electrochemical capacitors: double layer and redox. Double layer capacitors operate on the premise of the separation of electronic and ionic charges at the interface between electrode materials and electrolytes, to form a dependence on the electrolyte material for high-energy storage properties. In contrast, redox capacitors give rise to pseudocapacitance, which is based on a faradic process within the electroactive material itself.<sup>329</sup>

Since hydrogen can be electrochemically inserted into and extracted from Pd-based electrodes, these materials can be considered as phase charging/discharging systems for electrochemical capacitors. For the most part, these devices use the capacitance of the electrical double layer of carbon materials (or pseudocapacitance) connected with reversible redox processes, such as the insertion of atomic species into the crystal structures of bulk solid electrodes.<sup>330,331</sup> Thin films of Pd alloys with Pt, Au, and Rh electrodeposited on reticulated vitreous

carbon have been investigated by Łukaszewski et al.<sup>330,331</sup> for their application as phase charging/discharging systems at 283–313 K. Their findings disclosed that Pd–Rh alloys with 85–95% Pd and Pd–Pt alloys with 90–95% Pd exhibited optimal performance. The approximate maximum value for the specific pseudocapacitance achieved was 4500 F g<sup>-1</sup>, for a specific energy of 150 J g<sup>-1</sup>, and a specific power of up to 750 W g<sup>-1</sup>. The capacitance of the Pd–H system was fundamentally based on pseudocapacitance that resulted from redox processes that occurred within the bulk of the electroactive material, which caused the supercapacitor to behave similarly to a battery.<sup>331</sup> In comparison, C<sub>60</sub>–Pd polymers have received a great deal of attention for their excellent redox reversibility and stability.<sup>329,332–334</sup> Researchers, including Winkler et al.,<sup>329</sup> Grądzka et al.,<sup>334</sup> and Branczewicz et al.,<sup>332,333</sup> have investigated their capacitive performance, and attempted through variations in synthesis techniques to alleviate the limitations on electrochemical behaviors that are brought on by the effects of film composition.

Noble metal nanoparticles are known for their exceptional catalytic properties, which have led to potential applications in organic synthesis, fuel cells, and environmental remediation. In particular, Pd nanomaterials offer unique physiochemical properties and extensive surface areas that lead to enhanced reactivity in the electrochemical treatment of wastewater contaminants, such as nitrophenols and chlorinated organic compounds.<sup>95,123,335–340</sup>

Nitrophenols and chlorinated organic compounds are notorious industrial pollutants that are commonly found in wastewater runoff. Their high toxicity and resistance to degradation pose serious threats to human health and environmental ecosystems. With respect to nitrophenol degradation, the electron-withdrawing effect of the nitro group increases the resistance of nitrophenol compounds to chemical oxidation, biological oxidation, and hydrolysis.<sup>335</sup> Additionally, current dechlorination methods against persistent and bioaccumulative chlorinated organic compounds are limited in advanced water treatment due to high cost and, more specifically, the formation of secondary intractable contaminants.<sup>123</sup> Recently, electrochemical remediation methods have received increased interest for their simplicity of use, rapid degradation, and low environmental strain. Research conducted by Shi et al.,<sup>95</sup> Qiu et al.,<sup>123</sup> Li et al.,<sup>339</sup> and Dong et al.<sup>336</sup> has focused on wastewater remediation at the surfaces of Pd-based electrocatalysts.

Shi et al.<sup>95</sup> reported the direct electrochemical reduction of *m*-nitrophenol on a Pd/GC electrode in aqueous solutions. They observed a slow decay of catalytic activity of the Pd/GC electrode following prolonged electrolysis, which was attributed to the adsorption of the products of nitrophenol reduction onto the surface. Studies conducted by Li et al.<sup>339</sup> involved Pd-decorated CNTs that exhibited ultrahigh catalytic activity toward the reduction of 4-nitrophenol. Further investigations focused on Pd catalyst fabrication techniques, which limited the use of rigorous conditions or toxic agents to generate a rapid, efficient, and green approach for the synthesis of highly active catalysts.<sup>337,338,340</sup>

Pd is considered to be one of the most effective hydrodechlorination catalysts under ambient conditions. The use of bimetallic Pd–Fe thin films for reductive dechlorination was explored by Qiu et al.<sup>123</sup> The synergistic effects between Pd and Fe produced high reactivity toward the electrochemical reduction of chlorinated organic compounds. As relates to these

interactions, Dong et al.<sup>336</sup> were able to effectively reduce the consumption of Pd through the fabrication of Ni@Pd core–shell nanoparticles. The limited use of Pd within the core–shell structure facilitated cost reduction without sacrificing catalytic performance for both dechlorination and nitrophenol degradation.

The increasing accumulation of primary greenhouse gases (e.g., CO<sub>2</sub>) in the ambient atmosphere has attracted attention to the conversion of CO<sub>2</sub> to useful fuels as a carbon source. The electrochemical reduction of CO<sub>2</sub> at Pd not only can decrease CO<sub>2</sub> release but also aids in the production of valuable resources such as fuel and chemical feedstock (HCOOH, CO, CH<sub>4</sub>, CH<sub>4</sub>O, C<sub>2</sub>H<sub>6</sub>O, etc.).<sup>341,342</sup> Gao et al.<sup>341</sup> examined the size-dependent electrocatalytic reduction of CO<sub>2</sub> over Pd nanoparticles, ranging in size from 3.4 to 10.3 nm. Their work revealed unique particle size dependence for catalytic efficiencies, where varying nanoparticle dimensions created ratios of corner (Pd<sub>55</sub> or Pd<sub>38</sub>), edge (Pd(211)), and terrace (Pd(111)) sites that were able to tune CO<sub>2</sub> adsorption, COOH\* formation, and CO\* removal during CO<sub>2</sub> reduction. In summary, Pd nanomaterials possess unique physiochemical properties that offer improvements in electrochemical capacitors, wastewater treatment, and greenhouse gas (CO<sub>2</sub>) reduction.

#### 4. CONCLUSIONS AND OUTLOOK

Pd is well-known for its remarkable capacity for hydrogen absorption/adsorption, and is broadly employed as a primary catalyst for the low-temperature reduction of automobile pollutants, hydrogenation reactions, hydrogen purification, petroleum cracking, and a wide range of electrochemical applications. This review has detailed and compared a number of methods for the synthesis of Pd-based nanomaterials, as well as the impacts of the dimensions, morphologies, and compositions toward various electrochemical applications. The fabrication methods described include physical synthesis techniques, hydrothermal methods, electrochemical deposition, and other methods, such as electroless deposition, micro-emulsions, and photochemically assisted synthesis. Section 3 discussed the chemical and catalytic properties of Pd and Pd-based nanomaterials for electrochemical purposes, including fuel cells, hydrogen purification and storage, gas sensors, biosensors, capacitors, and the degradation of pollutants.

The design and implementation of high-performance Pd-based nanomaterials are anticipated to grow considerably over the next decade. With increasing environmental concerns and the accelerated depletion of fossil fuels, there will be a significant demand for the development of advanced technologies for environmental remediation, as well as for the production of alternative energy conversion and storage devices. In the biomedical sector, the increasing need for point-of-care, real-time quantitative detection and monitoring will drive the emergence of innovative devices. However, a number of challenges remain to be resolved prior to the broad commercial application of Pd-based nanomaterials.

The primary drawback of Pd, much like platinum, is its exorbitant cost. Over the past several years, the price of Pd has increased and is expected to continue to rise as interest in this material expands. Because of this, there is an urgent requirement for the design of advanced catalysts to reduce the required amount of noble metals, while increasing their activity and stability. Issues to consider in the creation of novel Pd-based nanomaterials encompass (i) size control—to achieve

optimal electrochemically active sites, (ii) shape control—to better understand growth mechanisms to effectively tailor the geometries of complex catalysts, (iii) control of high-index facets—for improved catalytic activity, (iv) optimization of bimetallic and trimetallic compositions and architectures—to enhance activity and stability, (v) establishment of the fundamental correlations between composition, structure, and reactivity of Pd nanomaterials—to create highly efficient catalysts by design, (vi) discovery of new substrate materials with high conductivity, chemical and mechanical stability, and surface area, and (vii) enabling the uniform distribution of Pd-based catalysts on support materials—to further improve efficiency.

The shape, size, architecture, composition, and microstructure of Pd-based nanocomposites are the key parameters in the determination and enhancement of their functionality and potential applications. The physical and chemical properties of Pd may be specifically tuned by controlling one or more of the aforementioned parameters. We are hopeful that this review has provided a practical framework to facilitate the emergence of innovations to address the challenges that currently impede the incorporation of Pd nanomaterials in various electrochemical applications, and demarcated the requirements for future development. Further advances in innovative synthesis techniques will undoubtedly lead to the discovery of additional unique properties of Pd-based nanomaterials, and subsequently to applications that will continue to benefit industry, the environment, and society at large.

## AUTHOR INFORMATION

### Corresponding Author

\*Phone: 807-343-8318. Fax: 807-346-7775. E-mail: [aicheng.chen@lakeheadu.ca](mailto:aicheng.chen@lakeheadu.ca).

### Notes

The authors declare no competing financial interest.

### Biographies



Aicheng Chen is a Professor of Chemistry and Canada Research Chair in Materials and Environmental Chemistry at Lakehead University. He received his M.Sc. in physical chemistry from Xiamen University in 1992 under the supervision of Professor S.-G. Sun and his Ph.D. in electrochemistry at the University of Guelph in 1998 under the direction of Professor J. Lipkowski. Chen's research interests span the areas of electrochemistry, biosensors, green chemistry, materials science, and nanotechnology. He has published 7 book chapters and over 150 peer-reviewed journal articles, authored over 80 industrial technical reports, and delivered ~90 invited presentations and lectures. He is a recipient of the Lakehead University Distinguished Researcher

Award, the Canadian Catalysis Lectureship Award, the Fred Beamish Award of the Canadian Society for Chemistry, the Lash Miller Award of The Electrochemical Society Canadian Section, the Keith Laidler Award of the Canadian Society for Chemistry, the RBC Innovation Award, the Japan Society for the Promotion of Science (JSPS) Fellowship, and the Ontario Premier's Research Excellence Award. In addition, he was elected as a Fellow of the Royal Society of Chemistry (United Kingdom) in 2011 and a Fellow of the International Society of Electrochemistry in 2014.



Cassandra Ostrom received her H.B.Sc. and M.Sc. degrees in chemistry from Lakehead University under the supervision of Professor Aicheng Chen in 2011 and 2013, respectively. Following her graduation, Cassandra performed collaborative research, which was supported by the Northern Ontario Heritage Fund Corp. This work encompassed electrochemical studies, metallurgy, nanomaterials development, and nanotechnology. For publication excellence, she was awarded the High Output Publication Excellence (HOPE) Award in 2014 by the Faculty of Graduate Studies, Lakehead University. Her research interests include the synthesis and electrochemical study of Pd-based nanomaterials with a focus on the improvement of the performance of fuel cell electrocatalysts, and hydrogen purification and storage toward the development of a hydrogen economy.

## ACKNOWLEDGMENTS

This work was supported by a Discovery Grant from the Natural Sciences and Engineering Research Council of Canada (NSERC RGPIN-2015-06248). A.C. acknowledges the NSERC and the Canada Foundation for Innovation (CFI) for the Canada Research Chair Award in Materials and Environmental Chemistry.

## REFERENCES

- (1) Yu, X.; Pickup, P. G. Recent Advances in Direct Formic Acid Fuel Cells (DFAFC). *J. Power Sources* **2008**, *182*, 124–132.
- (2) Zhang, H.; Jin, M.; Xia, Y. Enhancing the Catalytic and Electrocatalytic Properties of Pt-Based Catalysts by Forming Bimetallic Nanocrystals with Pd. *Chem. Soc. Rev.* **2012**, *41*, 8035–8049.
- (3) Chen, A. Electrocatalysis and Photoelectrochemistry Based on Functional Nanomaterials. *Can. J. Chem.* **2014**, *92*, 581–597.
- (4) Guo, S.; Wang, E. Noble Metal Nanomaterials: Controllable Synthesis and Application in Fuel Cells and Analytical Sensors. *Nano Today* **2011**, *6*, 240–264.
- (5) Bianchini, C.; Shen, P. K. Palladium-Based Electrocatalysts for Alcohol Oxidation in Half Cells and in Direct Alcohol Fuel Cells. *Chem. Rev.* **2009**, *109*, 4183–4206.
- (6) Shao, M. Palladium-Based Electrocatalysts for Hydrogen Oxidation and Oxygen Reduction Reactions. *J. Power Sources* **2011**, *196*, 2433–2444.

- (7) Zhang, H.; Jin, M.; Xiong, Y.; Lim, B.; Xia, Y. Shape-Controlled Synthesis of Pd Nanocrystals and Their Catalytic Applications. *Acc. Chem. Res.* **2013**, *46*, 1783–1794.
- (8) Suzuki, A. Recent Advances in the Cross-Coupling Reactions of Organoboron Derivatives with Organic Electrophiles, 1995–1998. *J. Organomet. Chem.* **1999**, *576*, 147–168.
- (9) Chinchilla, R.; Nájera, C. The Sonogashira Reaction: A Booming Methodology in Synthetic Organic Chemistry. *Chem. Rev.* **2007**, *107*, 874–922.
- (10) Adams, B. D.; Chen, A. The Role of Palladium in a Hydrogen Economy. *Mater. Today* **2011**, *14*, 282–289.
- (11) Teranishi, T.; Miyake, M. Size Control of Palladium Nanoparticles and Their Crystal Structures. *Chem. Mater.* **1998**, *10*, 594–600.
- (12) Yarulin, A. E.; Crespo-Quesada, R. M.; Egorova, E. V.; Kiwi-Minsker, L. L. Structure Sensitivity of Selective Acetylene Hydrogenation over the Catalysts with Shape-Controlled Palladium Nanoparticles. *Kinet. Catal.* **2012**, *53*, 253–261.
- (13) Xiong, Y.; Xia, Y. Shape-Controlled Synthesis of Metal Nanostructures: The Case of Palladium. *Adv. Mater.* **2007**, *19*, 3385–3391.
- (14) Agostini, G.; Piovano, A.; Bertinetti, L.; Pellegrini, R.; Leofanti, G.; Groppo, E.; Lamberti, C. Effect of Different Face Centered Cubic Nanoparticle Distributions on Particle Size and Surface Area Determination: A Theoretical Study. *J. Phys. Chem. C* **2014**, *118*, 4085–4094.
- (15) Zhu, C.; Zeng, J.; Lu, P.; Liu, J.; Gu, Z.; Xia, Y. Aqueous-Phase Synthesis of Single-Crystal Pd Seeds 3 nm in Diameter and Their Use for the Growth of Pd Nanocrystals with Different Shapes. *Chem. - Eur. J.* **2013**, *19*, 5127–5133.
- (16) Niu, W.; Zhang, L.; Xu, G. Shape-Controlled Synthesis of Single-Crystalline Palladium Nanocrystals. *ACS Nano* **2010**, *4*, 1987–1996.
- (17) Choo, H. P.; Liew, K. Y.; Liu, H. Factors Affecting the Size of Polymer Stabilized Pd Nanoparticles. *J. Mater. Chem.* **2002**, *12*, 934–937.
- (18) Lim, B.; Jiang, M.; Camargo, P. H. C.; Cho, E. C.; Tao, J.; Lu, X.; Zhu, Y.; Xia, Y. Pd-Pt Bimetallic Nanodendrites with High Activity for Oxygen Reduction. *Science* **2009**, *324*, 1302–1305.
- (19) Nikoobakht, B.; El-Sayed, M. A. Preparation and Growth Mechanism of Gold Nanorods (NRs) Using Seed-Mediated Growth Method. *Chem. Mater.* **2003**, *15*, 1957–1962.
- (20) Ortiz, N.; Hammons, J. A.; Cheong, S.; Skrabalak, S. E. Monitoring Ligand-Mediated Growth and Aggregation of Metal Nanoparticles and Nanodendrites by In Situ Synchrotron Scattering Techniques. *ChemNanoMat* **2015**, *1*, 109–114.
- (21) Ortiz, N.; Skrabalak, S. E. Manipulating Local Ligand Environments for the Controlled Nucleation of Metal Nanoparticles and Their Assembly into Nanodendrites. *Angew. Chem., Int. Ed.* **2012**, *51*, 11757–11761.
- (22) Ortiz, N.; Skrabalak, S. E. On the Dual Roles of Ligands in the Synthesis of Colloidal Metal Nanostructures. *Langmuir* **2014**, *30*, 6649–6659.
- (23) Lv, T.; Wang, Y.; Choi, S.-I.; Chi, M.; Tao, J.; Pan, L.; Huang, C. Z.; Zhu, Y.; Xia, Y. Controlled Synthesis of Nanosized Palladium Icosahedra and Their Catalytic Activity towards Formic-Acid Oxidation. *ChemSusChem* **2013**, *6*, 1923–1930.
- (24) Wang, Y.; Xie, S.; Liu, J.; Park, J.; Huang, C. Z.; Xia, Y. Shape-Controlled Synthesis of Palladium Nanocrystals: A Mechanistic Understanding of the Evolution from Octahedrons to Tetrahedrons. *Nano Lett.* **2013**, *13*, 2276–2281.
- (25) Cuenya, B. R. Synthesis and Catalytic Properties of Metal Nanoparticles: Size, Shape, Support, Composition, and Oxidation State Effects. *Thin Solid Films* **2010**, *518*, 3127–3150.
- (26) Chen, M.; Wu, B.; Yang, J.; Zheng, N. Small Adsorbate-Assisted Shape Control of Pd and Pt Nanocrystals. *Adv. Mater.* **2012**, *24*, 862–879.
- (27) Li, H.; Chen, G.; Yang, H.; Wang, X.; Liang, J.; Liu, P.; Chen, M.; Zheng, N. Shape-Controlled Synthesis of Surface-Clean Ultrathin Palladium Nanosheets by Simply Mixing a Dinuclear Pd<sup>1</sup> Carbonyl Chloride Complex with H<sub>2</sub>O. *Angew. Chem., Int. Ed.* **2013**, *52*, 8368–8372.
- (28) Xia, Y.; Xiong, Y.; Lim, B.; Skrabalak, S. E. Shape-Controlled Synthesis of Metal Nanocrystals: Simple Chemistry Meets Complex Physics? *Angew. Chem., Int. Ed.* **2009**, *48*, 60–103.
- (29) Burda, C.; Chen, X.; Narayanan, R.; El-Sayed, M. A. Chemistry and Properties of Nanocrystals of Different Shapes. *Chem. Rev.* **2005**, *105*, 1025–1102.
- (30) Narayanan, R.; El-Sayed, M. A. Catalysis with Transition Metal Nanoparticles in Colloidal Solution: Nanoparticle Shape Dependence and Stability. *J. Phys. Chem. B* **2005**, *109*, 12663–12676.
- (31) Jin, M.; Zhang, H.; Xie, Z.; Xia, Y. Palladium Nanocrystals Enclosed by {100} and {111} Facets in Controlled Proportions and Their Catalytic Activities for Formic Acid Oxidation. *Energy Environ. Sci.* **2012**, *5*, 6352–6357.
- (32) Zhang, J. Z. Ultrafast Studies of Electron Dynamics in Semiconductor and Metal Colloidal Nanoparticles: Effects of Size and Surface. *Acc. Chem. Res.* **1997**, *30*, 423–429.
- (33) Bradley, J. S.; Hill, E. W.; Behal, S.; Klein, C.; Duteil, A.; Chaudret, B. Preparation and Characterization of Organosols of Monodispersed Nanoscale Palladium. Particle Size Effects in the Binding Geometry of Adsorbed Carbon Monoxide. *Chem. Mater.* **1992**, *4*, 1234–1239.
- (34) Kwon, G.; Ferguson, G. A.; Heard, C. J.; Tyo, E. C.; Yin, C.; DeBartolo, J.; Seifert, S.; Winans, R. E.; Kropf, A. J.; Greeley, J.; et al. Size-Dependent Subnanometer Pd Cluster (Pd4, Pd6, and Pd17) Water Oxidation Electrocatalysis. *ACS Nano* **2013**, *7*, 5808–5817.
- (35) Jin, M.; Liu, H.; Zhang, H.; Xie, Z.; Liu, J.; Xia, Y. Synthesis of Pd Nanocrystals Enclosed by {100} Facets and with Sizes < 10 nm for Application in CO Oxidation. *Nano Res.* **2011**, *4*, 83–91.
- (36) Savadogo, O.; Lee, K.; Oishi, K.; Mitsushima, S.; Kamiya, N.; Ota, K.-I. New Palladium Alloys Catalyst for the Oxygen Reduction Reaction in an Acid Medium. *Electrochem. Commun.* **2004**, *6*, 105–109.
- (37) Gu, L.; Luo, N.; Miley, G. H. Cathode Electrocatalyst Selection and Deposition for a Direct Borohydride/hydrogen Peroxide Fuel Cell. *J. Power Sources* **2007**, *173*, 77–85.
- (38) Lee, C.-H.; Wang, S.-C.; Yuan, C.-J.; Wen, M.-F.; Chang, K.-S. Comparison of Amperometric Biosensors Fabricated by Palladium Sputtering, Palladium Electrodeposition and Nafion/carbon Nanotube Casting on Screen-Printed Carbon Electrodes. *Biosens. Bioelectron.* **2007**, *22*, 877–884.
- (39) Yoon, S. R.; Hwang, G. H.; Cho, W. I.; Oh, I.-H.; Hong, S.-A.; Ha, H. Y. Modification of Polymer Electrolyte Membranes for DMFCs Using Pd Films Formed by Sputtering. *J. Power Sources* **2002**, *106*, 215–223.
- (40) RaviPrakash, J.; McDaniel, A. H.; Horn, M.; Pilione, L.; Sunal, P.; Messier, R.; McGrath, R. T.; Schweighardt, F. K. Hydrogen Sensors: Role of Palladium Thin Film Morphology. *Sens. Actuators, B* **2007**, *120*, 439–446.
- (41) Yang, M.; Liu, H.; Zhang, D.; Tong, X. Hydrogen Sensing Performance Comparison of Pd Layer and Pd/WO<sub>3</sub> Composite Thin Film Coated on Side-Polished Single- and Multimode Fibers. *Sens. Actuators, B* **2010**, *149*, 161–164.
- (42) Fedtke, P.; Wienecke, M.; Bunescu, M.-C.; Pietrzak, M.; Deistung, K.; Borchardt, E. Hydrogen Sensor Based on Optical and Electrical Switching. *Sens. Actuators, B* **2004**, *100*, 151–157.
- (43) Ghasempour, R.; Mortazavi, S. Z.; Irajiazad, A.; Rahimi, F. Hydrogen Sensing Properties of Multi-Walled Carbon Nanotube Films Sputtered by Pd. *Int. J. Hydrogen Energy* **2010**, *35*, 4445–4449.
- (44) Mougenot, M.; Caillard, A.; Brault, P.; Baranton, S.; Coutanceau, C. High Performance Plasma Sputtered PdPt Fuel Cell Electrodes with Ultra Low Loading. *Int. J. Hydrogen Energy* **2011**, *36*, 8429–8434.
- (45) Jukk, K.; Alexeyeva, N.; Sarapuu, A.; Ritslaid, P.; Kozlova, J.; Sammelselg, V.; Tammeveski, K. Electroreduction of Oxygen on Sputter-Deposited Pd Nanolayers on Multi-Walled Carbon Nanotubes. *Int. J. Hydrogen Energy* **2013**, *38*, 3614–3620.

- (46) Sarto, F.; Castagna, E.; De Francesco, M.; Dikonomos, T. M.; Giorgi, L.; Lecci, S.; Sansovini, M.; Violante, V. Morphology and Electrochemical Properties of Pd-Based Catalysts Deposited by Different Thin-Film Techniques. *Int. J. Hydrogen Energy* **2014**, *39*, 14701–14711.
- (47) Favaro, M.; Agnoli, S.; Perini, L.; Durante, C.; Gennaro, A.; Granozzi, G. Palladium Nanoparticles Supported on Nitrogen-Doped HOPG: A Surface Science and Electrochemical Study. *Phys. Chem. Chem. Phys.* **2013**, *15*, 2923–2931.
- (48) Sobczak, K.; Dluzewski, P.; Klepka, M. T.; Kurowska, B.; Czerwosz, E. Transmission Electron Microscopy Studies of the Pd–C Films Obtained by Physical and Chemical Vapor Deposition. *Int. J. Hydrogen Energy* **2012**, *37*, 18556–18562.
- (49) Farella, I.; Valentini, A.; Cioffi, N.; Torsi, L. Dual Ion-Beam Sputtering Deposition of Palladium-Fluoropolymer Nano-Composites. *Appl. Phys. A: Mater. Sci. Process.* **2005**, *80*, 791–795.
- (50) Cioffi, N.; Farella, I.; Torsi, L.; Valentini, A.; Sabbatini, L.; Zambonin, P. G. Ion-Beam Sputtered Palladium-Fluoropolymer Nano-Composites as Active Layers for Organic Vapors Sensors. *Sens. Actuators, B* **2003**, *93*, 181–186.
- (51) Zeng, X. Q.; Latimer, M. L.; Xiao, Z. L.; Panuganti, S.; Welp, U.; Kwok, W. K.; Xu, T. Hydrogen Gas Sensing with Networks of Ultrasmall Palladium Nanowires Formed on Filtration Membranes. *Nano Lett.* **2011**, *11*, 262–268.
- (52) Wang, M.; Feng, Y. Palladium–silver Thin Film for Hydrogen Sensing. *Sens. Actuators, B* **2007**, *123*, 101–106.
- (53) Amin-Ahmadi, B.; Idrissi, H.; Galceran, M.; Colla, M. S.; Raskin, J. P.; Pardo, T.; Godet, S.; Schryvers, D. Effect of Deposition Rate on the Microstructure of Electron Beam Evaporated Nanocrystalline Palladium Thin Films. *Thin Solid Films* **2013**, *539*, 145–150.
- (54) Spencer, J. A.; Rosenberg, S. G.; Barclay, M.; Wu, Y.-C.; McElwee-White, L.; Howard Fairbrother, D. Understanding the Electron-Stimulated Surface Reactions of Organometallic Complexes to Enable Design of Precursors for Electron Beam-Induced Deposition. *Appl. Phys. A: Mater. Sci. Process.* **2014**, *117*, 1631–1644.
- (55) Barzola-Quiquia, J.; Schulze, S.; Esquinazi, P. Transport Properties and Atomic Structure of Ion-Beam-Deposited W, Pd and Pt Nanostructures. *Nanotechnology* **2009**, *20*, 165704–165711.
- (56) Bhuvana, T.; Kulkarni, G. U. Highly Conducting Patterned Pd Nanowires by Direct-Write Electron Beam Lithography. *ACS Nano* **2008**, *2*, 457–462.
- (57) Ocola, L. E.; Rue, C.; Maas, D. High-Resolution Direct-Write Patterning Using Focused Ion Beams. *MRS Bull.* **2014**, *39*, 336–341.
- (58) Nánai, L.; Balint, A. M. Laser Induced Chemical Liquid Phase Deposition (LCLD). *AIP Conf. Proc.* **2011**, *1472*, 148–154.
- (59) Muniz-Miranda, M.; Gellini, C.; Canton, P.; Marsili, P.; Giorgetti, E. SERS and Catalytically Active Ag/Pd Nanoparticles Obtained by Combining Laser Ablation and Galvanic Replacement. *J. Alloys Compd.* **2014**, *615*, S352–S356.
- (60) Mortazavi, S. Z.; Parvin, P.; Reyhani, A.; Golikand, A. N.; Mirshadi, S. Effect of Laser Wavelength at IR (1064 nm) and UV (193 nm) on the Structural Formation of Palladium Nanoparticles in Deionized Water. *J. Phys. Chem. C* **2011**, *115*, 5049–5057.
- (61) Cristoforetti, G.; Pitzalis, E.; Spiniello, R.; Ishak, R.; Muniz-Miranda, M. Production of Palladium Nanoparticles by Pulsed Laser Ablation in Water and Their Characterization. *J. Phys. Chem. C* **2011**, *115*, 5073–5083.
- (62) Cristoforetti, G.; Pitzalis, E.; Spiniello, R.; Ishak, R.; Giammanco, F.; Muniz-Miranda, M.; Caporali, S. Physico-Chemical Properties of Pd Nanoparticles Produced by Pulsed Laser Ablation in Different Organic Solvents. *Appl. Surf. Sci.* **2012**, *258*, 3289–3297.
- (63) Nishi, T.; Suzuki, N.; Takahashi, N.; Yano, K. Preparation of Monodispersed Pd Nanoparticles by Laser Ablation at Air–suspension Interface. *J. Nanopart. Res.* **2013**, *15*, 1–7.
- (64) Shatokhin, A. N.; Kudryashov, S. I.; Safanova, O. V.; Gas'kov, A. N.; Demidov, A. V.; Putilin, F. N. Laser Ablation Doping of Poly Crystalline Tin Dioxide Films with Palladium. *High Energy Chem.* **2000**, *34*, 182–187.
- (65) Kim, J.; Amaranatha Reddy, D.; Ma, R.; Kim, T. K. The Influence of Laser Wavelength and Fluence on Palladium Nanoparticles Produced by Pulsed Laser Ablation in Deionized Water. *Solid State Sci.* **2014**, *37*, 96–102.
- (66) Nishi, T.; Takeichi, A.; Azuma, H.; Suzuki, N.; Motohiro, T. Fabrication of Palladium Nanoparticles by Laser Ablation in Liquid. *J. Laser Micro/Nanoeng.* **2010**, *5*, 192–196.
- (67) Semaltianos, N. G.; Petkov, P.; Scholz, S.; Guetaz, L. Palladium or Palladium Hydride Nanoparticles Synthesized by Laser Ablation of a Bulk Palladium Target in Liquids. *J. Colloid Interface Sci.* **2013**, *402*, 307–311.
- (68) Bagmut, A. G.; Shipkova, I. G.; Zhuchkov, V. A. Structure and Magnetic State of the Films Deposited by Laser Ablation of Composite Nickel and Palladium Targets. *Tech. Phys.* **2011**, *56*, 531–539.
- (69) Torrisi, L.; Caridi, F.; Giuffrida, L. Comparison of Pd Plasmas Produced at 532nm and 1064nm by a Nd:YAG Laser Ablation. *Nucl. Instrum. Methods Phys. Res., Sect. B* **2010**, *268*, 2285–2291.
- (70) Yi, Q.; Huang, W.; Liu, X.; Xu, G.; Zhou, Z.; Chen, A. Electroactivity of Titanium-Supported Nanoporous Pd–Pt Catalysts towards Formic Acid Oxidation. *J. Electroanal. Chem.* **2008**, *619*–620, 197–205.
- (71) Adams, B. D.; Wu, G.; Nigro, S.; Chen, A. Facile Synthesis of Pd–Cd Nanostructures with High Capacity for Hydrogen Storage. *J. Am. Chem. Soc.* **2009**, *131*, 6930–6931.
- (72) Adams, B. D.; Ostrom, C. K.; Chen, A. Hydrogen Electrosorption into Pd–Cd Nanostructures. *Langmuir* **2010**, *26*, 7632–7637.
- (73) Guo, P.; Wei, Z.; Ye, W.; Qin, W.; Wang, Q.; Guo, X.; Lu, C.; Zhao, X. S. Preparation and Characterization of Nanostructured Pd with High Electrocatalytic Activity. *Colloids Surf., A* **2012**, *395*, 75–81.
- (74) Kuai, L.; Yu, X.; Wang, S.; Sang, Y.; Geng, B. Au–Pd Alloy and Core–Shell Nanostructures: One-Pot Coreduction Preparation, Formation Mechanism, and Electrochemical Properties. *Langmuir* **2012**, *28*, 7168–7173.
- (75) Ahmadalinezhad, A.; Chatterjee, S.; Chen, A. Synthesis and Electrochemical Study of Nanoporous Palladium–cadmium Networks for Non-Enzymatic Glucose Detection. *Electrochim. Acta* **2013**, *112*, 927–932.
- (76) Wu, M.-C.; Chang, I.-C.; Huang, W.-K.; Tu, Y.-C.; Hsu, C.-P.; Su, W.-F. Correlation between Palladium Chemical State and Photocatalytic Performance of TiO<sub>2</sub>–Pd Based Nanoparticles. *Thin Solid Films* **2014**, *570*, 371–375.
- (77) Chang, Y.; Xu, J.; Zhang, Y.; Ma, S.; Xin, L.; Zhu, L.; Xu, C. Optical Properties and Photocatalytic Performances of Pd Modified ZnO Samples. *J. Phys. Chem. C* **2009**, *113*, 18761–18767.
- (78) Yi, Q.; Niu, F.; Sun, L. Fabrication of Novel Porous Pd Particles and Their Electroactivity towards Ethanol Oxidation in Alkaline Media. *Fuel* **2011**, *90*, 2617–2623.
- (79) Kang, W.; Li, H.; Yan, Y.; Xiao, P.; Zhu, L.; Tang, K.; Zhu, Y.; Qian, Y. Worm-Like Palladium/Carbon Core–Shell Nanocomposites: One-Step Hydrothermal Reduction–Carbonization Synthesis and Electrocatalytic Activity. *J. Phys. Chem. C* **2011**, *115*, 6250–6256.
- (80) Zhang, Z.; Sun, T.; Chen, C.; Xiao, F.; Gong, Z.; Wang, S. Bifunctional Nanocatalyst Based on Three-Dimensional Carbon Nanotube–Graphene Hydrogel Supported Pd Nanoparticles: One-Pot Synthesis and Its Catalytic Properties. *ACS Appl. Mater. Interfaces* **2014**, *6*, 21035–21040.
- (81) Adams, B. D.; Asmussen, R. M.; Ostrom, C. K.; Chen, A. Synthesis and Comparative Study of Nanoporous Palladium-Based Bimetallic Catalysts for Formic Acid Oxidation. *J. Phys. Chem. C* **2014**, *118*, 29903–29910.
- (82) Nguyen, T.-T.; Pan, C.-J.; Liu, J.-Y.; Chou, H.-L.; Rick, J.; Su, W.-N.; Hwang, B.-J. Functional Palladium Tetrapod Core of Heterogeneous Palladium–Platinum Nanodendrites for Enhanced Oxygen Reduction Reaction. *J. Power Sources* **2014**, *251*, 393–401.
- (83) Yuan, M.; Liu, A.; Zhao, M.; Dong, W.; Zhao, T.; Wang, J.; Tang, W. Bimetallic PdCu Nanoparticle Decorated Three-Dimensional Graphene Hydrogel for Non-Enzymatic Amperometric Glucose Sensor. *Sens. Actuators, B* **2014**, *190*, 707–714.

- (84) Yang, L.; Hu, C.; Wang, J.; Yang, Z.; Guo, Y.; Bai, Z.; Wang, K. Facile Synthesis of Hollow Palladium/copper Alloyed Nanocubes for Formic Acid Oxidation. *Chem. Commun.* **2011**, *47*, 8581–8583.
- (85) Wang, J.; Asmussen, R. M.; Adams, B.; Thomas, D. F.; Chen, A. Facile Synthesis and Electrochemical Properties of Intermetallic PtPb Nanodendrites. *Chem. Mater.* **2009**, *21*, 1716–1724.
- (86) Wang, J.; Thomas, D. F.; Chen, A. Direct Growth of Novel Alloyed PtAu Nanodendrites. *Chem. Commun.* **2008**, *40*, 5010–5012.
- (87) Renjith, A.; Lakshminarayanan, V. One Step Preparation of “ready to Use” Au@Pd Nanoparticle Modified Surface Using Deep Eutectic Solvents and a Study of Its Electrocatalytic Properties in Methanol Oxidation Reaction. *J. Mater. Chem. A* **2015**, *3*, 3019–3028.
- (88) Arenz, M.; Stamenovic, V.; Schmidt, T. J.; Wandelt, K.; Ross, P. N.; Markovic, N. M. The Electro-Oxidation of Formic Acid on Pt-Pd Single Crystal Bimetallic Surfaces. *Phys. Chem. Chem. Phys.* **2003**, *5*, 4242–4251.
- (89) Lim, S. H.; Wei, J.; Lin, J.; Li, Q.; KuaYou, J. A Glucose Biosensor Based on Electrodeposition of Palladium Nanoparticles and Glucose Oxidase onto Nafion-Solubilized Carbon Nanotube Electrode. *Biosens. Bioelectron.* **2005**, *20*, 2341–2346.
- (90) Liu, J.; Ye, J.; Xu, C.; Jiang, S. P.; Tong, Y. Kinetics of Ethanol Electrooxidation at Pd Electrodeposited on Ti. *Electrochim. Commun.* **2007**, *9*, 2334–2339.
- (91) Mustain, W. E.; Prakash, J. Kinetics and Mechanism for the Oxygen Reduction Reaction on Polycrystalline Cobalt–Palladium Electrocatalysts in Acid Media. *J. Power Sources* **2007**, *170*, 28–37.
- (92) Safavi, A.; Maleki, N.; Tajabadi, F.; Farjam, E. High Electrocatalytic Effect of Palladium Nanoparticle Arrays Electrodeposited on Carbon Ionic Liquid Electrode. *Electrochim. Commun.* **2007**, *9*, 1963–1968.
- (93) Wang, H.; Xu, C.; Cheng, F.; Jiang, S. Pd Nanowire Arrays as Electrocatalysts for Ethanol Electrooxidation. *Electrochim. Commun.* **2007**, *9*, 1212–1216.
- (94) Łukaszewski, M.; Czerwiński, A. Selected Electrochemical Properties of Pd–Au Alloys: Hydrogen Absorption and Surface Oxidation. *J. Solid State Electrochem.* **2008**, *12*, 1589–1598.
- (95) Shi, Q.; Diao, G. The Electrocatalytical Reduction of M-Nitrophenol on Palladium Nanoparticles Modified Glassy Carbon Electrodes. *Electrochim. Acta* **2011**, *58*, 399–405.
- (96) Jiang, Y.; Lu, Y.; Li, F.; Wu, T.; Niu, L.; Chen, W. Facile Electrochemical Codeposition of “Clean” Graphene–Pd Nanocomposite as an Anode Catalyst for Formic Acid Electrooxidation. *Electrochim. Commun.* **2012**, *19*, 21–24.
- (97) Erikson, H.; Liik, M.; Sarapuu, A.; Kozlova, J.; Sammelselg, V.; Tammeveski, K. Oxygen Reduction on Electrodeposited Pd Coatings on Glassy Carbon. *Electrochim. Acta* **2013**, *88*, 513–518.
- (98) Habibi, B. Aluminum Supported Palladium Nanoparticles: Preparation, Characterization and Application for Formic Acid Electrooxidation. *Int. J. Hydrogen Energy* **2013**, *38*, 5464–5472.
- (99) Liu, A.; Yuan, M.; Zhao, M.; Lu, C.; Zhao, T.; Li, P.; Tang, W. Graphene Modulated Assembly of PtPd Bimetallic Catalysts for Electro-Oxidation of Methanol. *J. Alloys Compd.* **2014**, *586*, 99–104.
- (100) Xiao, L.; Zhuang, L.; Liu, Y.; Lu, J. Activating Pd by Morphology Tailoring for Oxygen Reduction. *J. Am. Chem. Soc.* **2009**, *131*, 602–608.
- (101) Choi, S.; Jeong, H.; Choi, K.; Song, J. Y.; Kim, J. Electrodeposition of Triangular Pd Rod Nanostructures and Their Electrocatalytic and SERS Activities. *ACS Appl. Mater. Interfaces* **2014**, *6*, 3002–3007.
- (102) Maniam, K. K.; Chetty, R. Electrodeposited Palladium Nanoflowers for Electrocatalytic Applications. *Fuel Cells* **2013**, *13*, 1196–1204.
- (103) Salomé, S.; Rego, R.; Querejeta, A.; Alcaide, F.; Oliveira, M. C. An Electrochemical Route to Prepare Pd Nanostructures on a Gas Diffusion Substrate for a PEMFC. *Electrochim. Acta* **2013**, *106*, 516–524.
- (104) Cui, C.-H.; Yu, J.-W.; Li, H.-H.; Gao, M.-R.; Liang, H.-W.; Yu, S.-H. Remarkable Enhancement of Electrocatalytic Activity by Tuning the Interface of Pd–Au Bimetallic Nanoparticle Tubes. *ACS Nano* **2011**, *5*, 4211–4218.
- (105) Cheng, F.; Wang, H.; Sun, Z.; Ning, M.; Cai, Z.; Zhang, M. Electrodeposited Fabrication of Highly Ordered Pd Nanowire Arrays for Alcohol Electrooxidation. *Electrochim. Commun.* **2008**, *10*, 798–801.
- (106) Zhao, Y.; Qin, S.-J.; Li, Y.; Deng, F.-X.; Liu, Y.-Q.; Pan, G.-B. Electrodeposition of Dendritic Pd Nanoarchitectures on N-GaN(0001): Nucleation and Electrocatalysis for Direct Formic Acid Fuel Cells. *Electrochim. Acta* **2014**, *145*, 148–153.
- (107) Bai, H.; Han, M.; Du, Y.; Bao, J.; Dai, Z. Facile Synthesis of Porous Tubular Palladium Nanostructures and Their Application in a Nonenzymatic Glucose Sensor. *Chem. Commun.* **2010**, *46*, 1739–1741.
- (108) Lu, X.; Luo, F.; Song, H.; Liao, S.; Li, H. Pulse Electrodeposition to Prepare Core–shell Structured AuPt@Pd/C Catalyst for Formic Acid Fuel Cell Application. *J. Power Sources* **2014**, *246*, 659–666.
- (109) Liu, L.; Yoo, S.-H.; Lee, S. A.; Park, S. Wet-Chemical Synthesis of Palladium Nanosprings. *Nano Lett.* **2011**, *11*, 3979–3982.
- (110) Schaltin, S.; Brooks, N. R.; Sniekers, J.; Van Meervelt, L.; Binnemanns, K.; Fransaer, J. Electrodeposition of Thick Palladium Coatings from a Palladium(II)-Containing Ionic Liquid. *Chem. Commun.* **2014**, *50*, 10248–10250.
- (111) Meng, H.; Xie, F.; Chen, J.; Shen, P. K. Electrodeposited Palladium Nanostructure as Novel Anode for Direct Formic Acid Fuel Cell. *J. Mater. Chem.* **2011**, *21*, 11352–11358.
- (112) Rezaei, M.; Tabaian, S. H.; Haghshenas, D. F. Electrochemical Nucleation and Growth of Pd/PdCo Core–shell Nanoparticles with Enhanced Activity and Durability as Fuel Cell Catalyst. *J. Mater. Chem. A* **2014**, *2*, 4588–4597.
- (113) Plowman, B. J.; Bhargava, S. K.; O’Mullane, A. P. Electrochemical Fabrication of Metallic Nanostructured Electrodes for Electroanalytical Applications. *Analyst* **2011**, *136*, 5107–5119.
- (114) Villanueva, L. G.; Fargier, F.; Kiefer, T.; Ramonda, M.; Brugger, J.; Favier, F. Highly Ordered Palladium Nanodot Patterns for Full Concentration Range Hydrogen Sensing. *Nanoscale* **2012**, *4*, 1964–1967.
- (115) Yang, D.; Carpena-Núñez, J.; Fonseca, L. F.; Biaggi-Labiosa, A.; Hunter, G. W. Shape-Controlled Synthesis of Palladium and Copper Superlattice Nanowires for High-Stability Hydrogen Sensors. *Sci. Rep.* **2014**, *4*, DOI: [10.1038/srep03773](https://doi.org/10.1038/srep03773).
- (116) Tian, N.; Zhou, Z.-Y.; Yu, N.-F.; Wang, L.-Y.; Sun, S.-G. Direct Electrodeposition of Tetrahedral Pd Nanocrystals with High-Index Facets and High Catalytic Activity for Ethanol Electrooxidation. *J. Am. Chem. Soc.* **2010**, *132*, 7580–7581.
- (117) Tian, N.; Zhou, Z.-Y.; Sun, S.-G. Electrochemical Preparation of Pd Nanorods with High-Index Facets. *Chem. Commun.* **2009**, *12*, 1502–1504.
- (118) Ji, H.; Li, M.; Wang, Y.; Gao, F. Electrodeposition of Graphene-Supported PdPt Nanoparticles with Enhanced Electrocatalytic Activity. *Electrochim. Commun.* **2012**, *24*, 17–20.
- (119) *Electrodeposition*; Djokic, S. S., Ed.; Modern Aspects of Electrochemistry, Vol. 48; Springer: New York, 2010.
- (120) Shao, M. H.; Huang, T.; Liu, P.; Zhang, J.; Sasaki, K.; Vukmirovic, M. B.; Adzic, R. R. Palladium Monolayer and Palladium Alloy Electrocatalysts for Oxygen Reduction. *Langmuir* **2006**, *22*, 10409–10415.
- (121) Lu, Y.; Chen, W. Nanoneedle-Covered Pd–Ag Nanotubes: High Electrocatalytic Activity for Formic Acid Oxidation. *J. Phys. Chem. C* **2010**, *114*, 21190–21200.
- (122) Ojani, R.; Abkar, Z.; Hasheminejad, E.; Raoof, J.-B. Rapid Fabrication of Cu/Pd Nano/micro-Particles Porous-Structured Catalyst Using Hydrogen Bubbles Dynamic Template and Their Enhanced Catalytic Performance for Formic Acid Electrooxidation. *Int. J. Hydrogen Energy* **2014**, *39*, 7788–7797.
- (123) Qiu, C.; Dong, X.; Huang, M.; Wang, S.; Ma, H. Facile Fabrication of Nanostructured Pd–Fe Bimetallic Thin Films and Their

- Electrodechlorination Activity. *J. Mol. Catal. A: Chem.* **2011**, *350*, 56–63.
- (124) Xia, X.; Wang, Y.; Ruditskiy, A.; Xia, Y. 25th Anniversary Article: Galvanic Replacement: A Simple and Versatile Route to Hollow Nanostructures with Tunable and Well-Controlled Properties. *Adv. Mater.* **2013**, *25*, 6313–6333.
- (125) Larsen, R.; Ha, S.; Zakzeski, J.; Masel, R. I. Unusually Active Palladium-Based Catalysts for the Electrooxidation of Formic Acid. *J. Power Sources* **2006**, *157*, 78–84.
- (126) Liu, Z.; Hong, L.; Tham, M. P.; Lim, T. H.; Jiang, H. Nanostructured Pt/C and Pd/C Catalysts for Direct Formic Acid Fuel Cells. *J. Power Sources* **2006**, *161*, 831–835.
- (127) Raghuveer, V.; Ferreira, P.; Manthiram, A. Comparison of Pd–Co–Au Electrocatalysts Prepared by Conventional Borohydride and Microemulsion Methods for Oxygen Reduction in Fuel Cells. *Electrochim. Commun.* **2006**, *8*, 807–814.
- (128) Xu, C.; Cheng, L.; Shen, P.; Liu, Y. Methanol and Ethanol Electrooxidation on Pt and Pd Supported on Carbon Microspheres in Alkaline Media. *Electrochim. Commun.* **2007**, *9*, 997–1001.
- (129) Xu, C.; Shen, P. k.; Liu, Y. Ethanol Electrooxidation on Pt/C and Pd/C Catalysts Promoted with Oxide. *J. Power Sources* **2007**, *164*, 527–531.
- (130) Salvador-Pascual, J. J.; Citalán-Cigarrón, S.; Solorza-Feria, O. Kinetics of Oxygen Reduction Reaction on Nanosized Pd Electrocatalyst in Acid Media. *J. Power Sources* **2007**, *172*, 229–234.
- (131) Yang, S.; Zhang, X.; Mi, H.; Ye, X. Pd Nanoparticles Supported on Functionalized Multi-Walled Carbon Nanotubes (MWCNTs) and Electrooxidation for Formic Acid. *J. Power Sources* **2008**, *175*, 26–32.
- (132) Wang, X.; Tang, Y.; Gao, Y.; Lu, T. Carbon-Supported Pd–Ir Catalyst as Anodic Catalyst in Direct Formic Acid Fuel Cell. *J. Power Sources* **2008**, *175*, 784–788.
- (133) Xu, C.; Tian, Z.; Shen, P.; Jiang, S. P. Oxide ( $\text{CeO}_2$ ,  $\text{NiO}$ ,  $\text{Co}_3\text{O}_4$  and  $\text{Mn}_3\text{O}_4$ )-Promoted Pd/C Electrocatalysts for Alcohol Electrooxidation in Alkaline Media. *Electrochim. Acta* **2008**, *53*, 2610–2618.
- (134) He, Q.; Chen, W.; Mukerjee, S.; Chen, S.; Laufek, F. Carbon-Supported PdM (M = Au and Sn) Nanocatalysts for the Electro-oxidation of Ethanol in High pH Media. *J. Power Sources* **2009**, *187*, 298–304.
- (135) Meng, L.; Jin, J.; Yang, G.; Lu, T.; Zhang, H.; Cai, C. Nonenzymatic Electrochemical Detection of Glucose Based on Palladium–Single-Walled Carbon Nanotube Hybrid Nanostructures. *Anal. Chem.* **2009**, *81*, 7271–7280.
- (136) Singh, R. N.; Singh, A.; Anindita. Electrocatalytic Activity of Binary and Ternary Composite Films of Pd, MWCNT, and Ni for Ethanol Electro-Oxidation in Alkaline Solutions. *Carbon* **2009**, *47*, 271–278.
- (137) Zhu, L. D.; Zhao, T. S.; Xu, J. B.; Liang, Z. X. Preparation and Characterization of Carbon-Supported Sub-Monolayer Palladium Decorated Gold Nanoparticles for the Electro-Oxidation of Ethanol in Alkaline Media. *J. Power Sources* **2009**, *187*, 80–84.
- (138) Adams, B. D.; Ostrom, C. K.; Chen, S.; Chen, A. High-Performance Pd-Based Hydrogen Spillover Catalysts for Hydrogen Storage. *J. Phys. Chem. C* **2010**, *114*, 19875–19882.
- (139) Park, I.-S.; Lee, K.-S.; Yoo, S. J.; Cho, Y.-H.; Sung, Y.-E. Electrocatalytic Properties of Pd Clusters on Au Nanoparticles in Formic Acid Electro-Oxidation. *Electrochim. Acta* **2010**, *55*, 4339–4345.
- (140) Winjobi, O.; Zhang, Z.; Liang, C.; Li, W. Carbon Nanotube Supported Platinum–Palladium Nanoparticles for Formic Acid Oxidation. *Electrochim. Acta* **2010**, *55*, 4217–4221.
- (141) Zhao, Y.; Yang, X.; Tian, J.; Wang, F.; Zhan, L. Methanol Electro-Oxidation on Ni@Pd Core-Shell Nanoparticles Supported on Multi-Walled Carbon Nanotubes in Alkaline Media. *Int. J. Hydrogen Energy* **2010**, *35*, 3249–3257.
- (142) Huang, C.-C.; Pu, N.-W.; Wang, C.-A.; Huang, J.-C.; Sung, Y.; Ger, M.-D. Hydrogen Storage in Graphene Decorated with Pd and Pt Nano-Particles Using an Electroless Deposition Technique. *Sep. Purif. Technol.* **2011**, *82*, 210–215.
- (143) Adams, B. D.; Ostrom, C. K.; Chen, A. Highly Active PdPt Catalysts for the Electrochemical Reduction of  $\text{H}_2\text{O}_2$ . *J. Electrochem. Soc.* **2011**, *158*, B434–B439.
- (144) Parambhath, V. B.; Nagar, R.; Sethupathi, K.; Ramaprabhu, S. Investigation of Spillover Mechanism in Palladium Decorated Hydrogen Exfoliated Functionalized Graphene. *J. Phys. Chem. C* **2011**, *115*, 15679–15685.
- (145) Wang, H.; Wang, R.; Li, H.; Wang, Q.; Kang, J.; Lei, Z. Facile Synthesis of Carbon-Supported Pseudo-Core@Shell PdCu@Pt Nanoparticles for Direct Methanol Fuel Cells. *Int. J. Hydrogen Energy* **2011**, *36*, 839–848.
- (146) Zhang, G.; Wang, Y.; Wang, X.; Chen, Y.; Zhou, Y.; Tang, Y.; Lu, L.; Bao, J.; Lu, T. Preparation of Pd–Au/C Catalysts with Different Alloying Degree and Their Electrocatalytic Performance for Formic Acid Oxidation. *Appl. Catal., B* **2011**, *102*, 614–619.
- (147) Chen, G.; Liao, M.; Yu, B.; Li, Y.; Wang, D.; You, G.; Zhong, C.-J.; Chen, B. H. Pt Decorated PdAu/C Nanocatalysts with Ultralow Pt Loading for Formic Acid Electrooxidation. *Int. J. Hydrogen Energy* **2012**, *37*, 9959–9966.
- (148) Chen, C.-C.; Lin, C.-L.; Chen, L.-C. Functionalized Carbon Nanomaterial Supported Palladium Nano-Catalysts for Electrocatalytic Glucose Oxidation Reaction. *Electrochim. Acta* **2015**, *152*, 408–416.
- (149) Ye, J.-S.; Chen, C.-W.; Lee, C.-L. Pd Nanocube as Non-Enzymatic Glucose Sensor. *Sens. Actuators, B* **2015**, *208*, 569–574.
- (150) Carrera-Cerritos, R.; Fuentes-Ramírez, R.; Cuevas-Muñiz, F. M.; Ledesma-García, J.; Arriaga, L. G. Performance and Stability of Pd Nanostructures in an Alkaline Direct Ethanol Fuel Cell. *J. Power Sources* **2014**, *269*, 370–378.
- (151) Wang, Y.; Peng, H.-C.; Liu, J.; Huang, C. Z.; Xia, Y. Use of Reduction Rate as a Quantitative Knob for Controlling the Twin Structure and Shape of Palladium Nanocrystals. *Nano Lett.* **2015**, *15*, 1445–1450.
- (152) Wang, Y.; Choi, S.-I.; Zhao, X.; Xie, S.; Peng, H.-C.; Chi, M.; Huang, C. Z.; Xia, Y. Polyol Synthesis of Ultrathin Pd Nanowires via Attachment-Based Growth and Their Enhanced Activity towards Formic Acid Oxidation. *Adv. Funct. Mater.* **2014**, *24*, 131–139.
- (153) Góral-Kurbiel, M.; Drelinkiewicz, A.; Kosydar, R.; Dembińska, B.; Kulesza, P. J.; Gurgul, J. Palladium Content Effect on the Electrocatalytic Activity of Palladium–Polypyrrole Nanocomposite for Cathodic Reduction of Oxygen. *Electrocatalysis* **2014**, *5*, 23–40.
- (154) Góral-Kurbiel, M.; Drelinkiewicz, A.; Kosydar, R.; Gurgul, J.; Dembińska, B.; Kulesza, P. J. The Effect of Nafion Ionomer on Electroactivity of Palladium–polypyrrole Catalysts for Oxygen Reduction Reaction. *J. Solid State Electrochem.* **2014**, *18*, 639–653.
- (155) Siril, P. F.; Ramos, L.; Beaunier, P.; Archirel, P.; Etcheberry, A.; Remita, H. Synthesis of Ultrathin Hexagonal Palladium Nanosheets. *Chem. Mater.* **2009**, *21*, 5170–5175.
- (156) Huang, X.; Tang, S.; Mu, X.; Dai, Y.; Chen, G.; Zhou, Z.; Ruan, F.; Yang, Z.; Zheng, N. Freestanding Palladium Nanosheets with Plasmonic and Catalytic Properties. *Nat. Nanotechnol.* **2011**, *6*, 28–32.
- (157) Huang, X.; Tang, S.; Yang, J.; Tan, Y.; Zheng, N. Etching Growth under Surface Confinement: An Effective Strategy To Prepare Mesocrystalline Pd Nanocorolla. *J. Am. Chem. Soc.* **2011**, *133*, 15946–15949.
- (158) Yin, X.; Liu, X.; Pan, Y.-T.; Walsh, K. A.; Yang, H. Hanoi Tower-like Multilayered Ultrathin Palladium Nanosheets. *Nano Lett.* **2014**, *14*, 7188–7194.
- (159) Xie, B.; Xiong, Y.; Chen, R.; Chen, J.; Cai, P. Catalytic Activities of Pd–TiO Film towards the Oxidation of Formic Acid. *Catal. Commun.* **2005**, *6*, 699–704.
- (160) Tian, M.; Malig, M.; Chen, S.; Chen, A. Synthesis and Electrochemical Study of  $\text{TiO}_2$ -Supported PdAu Nanoparticles. *Electrochim. Commun.* **2011**, *13*, 370–373.
- (161) Zhao, R.; Ding, R.; Yuan, S.; Jiang, W.; Liang, B. Palladium Membrane on  $\text{TiO}_2$  Nanotube Arrays-Covered Titanium Surface by Combination of Photocatalytic Deposition and Modified Electroless Plating Processes and Its Hydrogen Permeability. *Int. J. Hydrogen Energy* **2011**, *36*, 1066–1073.

- (162) Ismail, A. A.; Bahnemann, D. W.; Al-Sayari, S. A. Synthesis and Photocatalytic Properties of Nanocrystalline Au, Pd and Pt Photo-deposited onto Mesoporous RuO<sub>2</sub>-TiO<sub>2</sub> Nanocomposites. *Appl. Catal., A* **2012**, *431*–432, 62–68.
- (163) Wang, M.; Guo, D.; Li, H. High Activity of Novel Pd/TiO<sub>2</sub> Nanotube Catalysts for Methanol Electro-Oxidation. *J. Solid State Chem.* **2005**, *178*, 1996–2000.
- (164) Zheng, J.-N.; Li, S.-S.; Ma, X.; Chen, F.-Y.; Wang, A.-J.; Chen, J.-R.; Feng, J.-J. Green Synthesis of Core–shell Gold–Palladium@Palladium Nanocrystals Dispersed on Graphene with Enhanced Catalytic Activity toward Oxygen Reduction and Methanol Oxidation in Alkaline Media. *J. Power Sources* **2014**, *262*, 270–278.
- (165) Wang, Y.; Sheng, Z. M.; Yang, H.; Jiang, S. P.; Li, C. M. Electrocatalysis of Carbon Black- or Activated Carbon Nanotubes-Supported Pd–Ag towards Methanol Oxidation in Alkaline Media. *Int. J. Hydrogen Energy* **2010**, *35*, 10087–10093.
- (166) Zhao, X.; Yin, M.; Ma, L.; Liang, L.; Liu, C.; Liao, J.; Lu, T.; Xing, W. Recent Advances in Catalysts for Direct Methanol Fuel Cells. *Energy Environ. Sci.* **2011**, *4*, 2736–2753.
- (167) Choi, W. C.; Kim, J. D.; Woo, S. I. Modification of Proton Conducting Membrane for Reducing Methanol Crossover in a Direct-Methanol Fuel Cell. *J. Power Sources* **2001**, *96*, 411–414.
- (168) Hejze, T.; Gollas, B. R.; Sauerbrey, R. K.; Schmied, M.; Hofer, F.; Besenhard, J. O. Preparation of Pd-Coated Polymer Electrolyte Membranes and Their Application in Direct Methanol Fuel Cells. *J. Power Sources* **2005**, *140*, 21–27.
- (169) Serov, A. A.; Cho, S.-Y.; Han, S.; Min, M.; Chai, G.; Nam, K. H.; Kwak, C. Modification of Palladium-Based Catalysts by Chalcogenes for Direct Methanol Fuel Cells. *Electrochim. Commun.* **2007**, *9*, 2041–2044.
- (170) Liang, Z. X.; Zhao, T. S.; Xu, J. B.; Zhu, L. D. Mechanism Study of the Ethanol Oxidation Reaction on Palladium in Alkaline Media. *Electrochim. Acta* **2009**, *54*, 2203–2208.
- (171) Shen, S. Y.; Zhao, T. S.; Xu, J. B.; Li, Y. S. Synthesis of PdNi Catalysts for the Oxidation of Ethanol in Alkaline Direct Ethanol Fuel Cells. *J. Power Sources* **2010**, *195*, 1001–1006.
- (172) Bianchini, C.; Bambagioni, V.; Filippi, J.; Marchionni, A.; Vizza, F.; Bert, P.; Tampucci, A. Selective Oxidation of Ethanol to Acetic Acid in Highly Efficient Polymer Electrolyte Membrane-Direct Ethanol Fuel Cells. *Electrochim. Commun.* **2009**, *11*, 1077–1080.
- (173) Wang, W.; Yang, Y.; Liu, Y.; Zhang, Z.; Dong, W.; Lei, Z. Hybrid NiCoOx Adjacent to Pd Nanoparticles as a Synergistic Electrocatalyst for Ethanol Oxidation. *J. Power Sources* **2015**, *273*, 631–637.
- (174) Hong, W.; Wang, J.; Wang, E. Facile Synthesis of PdAgTe Nanowires with Superior Electrocatalytic Activity. *J. Power Sources* **2014**, *272*, 940–945.
- (175) Cai, J.; Zeng, Y.; Guo, Y. Copper@Palladium–Copper Core–Shell Nanospheres as a Highly Effective Electrocatalyst for Ethanol Electro-Oxidation in Alkaline Media. *J. Power Sources* **2014**, *270*, 257–261.
- (176) Mikolajczyk, T.; Turemko, M.; Pierozynski, B. Ethanol Oxidation Reaction at Pd-Modified Nickel Foam Obtained by PVD Method in Alkaline Solution. *J. Electroanal. Chem.* **2014**, *735*, 32–35.
- (177) Qin, Y.-H.; Li, Y.; Lv, R.-L.; Wang, T.-L.; Wang, W.-G.; Wang, C.-W. Pd-Au/C Catalysts with Different Alloying Degrees for Ethanol Oxidation in Alkaline Media. *Electrochim. Acta* **2014**, *144*, 50–55.
- (178) Kakaei, K.; Dorraji, M. One-Pot Synthesis of Palladium Silver Nanoparticles Decorated Reduced Graphene Oxide and Their Application for Ethanol Oxidation in Alkaline Media. *Electrochim. Acta* **2014**, *143*, 207–215.
- (179) Li, Z. Y.; Liang, Y. J.; Jiang, S. P.; Shan, X. D.; Lin, M. L.; Xu, C. W. Electrooxidation of Methanol and Ethylene Glycol Mixture on Platinum and Palladium in Alkaline Medium. *Fuel Cells* **2012**, *12*, 677–682.
- (180) Antolini, E.; Gonzalez, E. R. Alkaline Direct Alcohol Fuel Cells. *J. Power Sources* **2010**, *195*, 3431–3450.
- (181) Antolini, E. Palladium in Fuel Cell Catalysis. *Energy Environ. Sci.* **2009**, *2*, 915.
- (182) Hsieh, C.-T.; Gu, J.-L.; Chen, Y.-C.; Tzou, D.-Y. Pulse Microwave Synthesis of Palladium Catalysts on Graphene Electrodes for Proton Exchange Membrane Fuel Cells. *Electrochim. Acta* **2013**, *98*, 39–47.
- (183) Miao, F.; Tao, B.; Sun, L.; Liu, T.; You, J.; Wang, L.; Chu, P. K. Preparation and Characterization of Novel Nickel–palladium Electrodes Supported by Silicon Microchannel Plates for Direct Methanol Fuel Cells. *J. Power Sources* **2010**, *195*, 146–150.
- (184) Prabhuram, J.; Manoharan, R.; Vasan, H. N. Effects of Incorporation of Cu and Ag in Pd on Electrochemical Oxidation of Methanol in Alkaline Solution. *J. Appl. Electrochem.* **1998**, *28*, 935–941.
- (185) Tao, B.; Zhang, J.; Hui, S.; Chen, X.; Wan, L. An Electrochemical Methanol Sensor Based on a Pd–Ni/SiNWs Catalytic Electrode. *Electrochim. Acta* **2010**, *55*, 5019–5023.
- (186) Borasio, M.; Rodríguez de la Fuente, O.; Rupprechter, G.; Freund, H.-J. In Situ Studies of Methanol Decomposition and Oxidation on Pd(111) by PM-IRAS and XPS Spectroscopy. *J. Phys. Chem. B* **2005**, *109*, 17791–17794.
- (187) Bäumer, M.; Libuda, J.; Neyman, K. M.; Rösch, N.; Rupprechter, G.; Freund, H.-J. Adsorption and Reaction of Methanol on Supported Palladium Catalysts: Microscopic-Level Studies from Ultrahigh Vacuum to Ambient Pressure Conditions. *Phys. Chem. Chem. Phys.* **2007**, *9*, 3541–3558.
- (188) Yin, Z.; Chi, M.; Zhu, Q.; Ma, D.; Sun, J.; Bao, X. Supported Bimetallic PdAu Nanoparticles with Superior Electrocatalytic Activity towards Methanol Oxidation. *J. Mater. Chem. A* **2013**, *1*, 9157–9163.
- (189) Liu, Y.; Chi, M.; Mazumder, V.; More, K. L.; Soled, S.; Henao, J. D.; Sun, S. Composition-Controlled Synthesis of Bimetallic PdPt Nanoparticles and Their Electro-Oxidation of Methanol. *Chem. Mater.* **2011**, *23*, 4199–4203.
- (190) Su, Y.-Z.; Zhang, M.-Z.; Liu, X.-B.; Li, Z.-Y.; Zhu, X.-C.; Xu, C.-W.; Jiang, S. P. Development of Au Promoted Pd/C Electrocatalysts for Methanol, Ethanol and Isopropanol Oxidation in Alkaline Medium. *Int. J. Electrochem. Sci.* **2012**, *7*, 4158–4170.
- (191) Qi, Z.; Geng, H.; Wang, X.; Zhao, C.; Ji, H.; Zhang, C.; Xu, J.; Zhang, Z. Novel Nanocrystalline PdNi Alloy Catalyst for Methanol and Ethanol Electro-Oxidation in Alkaline Media. *J. Power Sources* **2011**, *196*, 5823–5828.
- (192) Liu, Z.; Zhang, X.; Hong, L. Physical and Electrochemical Characterizations of Nanostructured Pd/C and PdNi/C Catalysts for Methanol Oxidation. *Electrochim. Commun.* **2009**, *11*, 925–928.
- (193) Hsieh, M.-W.; Whang, T.-J. Electrodeposition of PdCu Alloy and Its Application in Methanol Electro-Oxidation. *Appl. Surf. Sci.* **2013**, *270*, 252–259.
- (194) Yin, Z.; Zhang, Y.; Chen, K.; Li, J.; Li, W.; Tang, P.; Zhao, H.; Zhu, Q.; Bao, X.; Ma, D. Monodispersed Bimetallic PdAg Nanoparticles with Twinned Structures: Formation and Enhancement for the Methanol Oxidation. *Sci. Rep.* **2014**, *4*, DOI: [10.1038/srep04288](https://doi.org/10.1038/srep04288).
- (195) Gupta, R.; Guin, S. K.; Aggarwal, S. K. Electrocristallization of Palladium (Pd) Nanoparticles on Platinum (Pt) Electrode and Its Application for Electro-Oxidation of Formic Acid and Methanol. *Electrochim. Acta* **2014**, *116*, 314–320.
- (196) Hammer, B.; Nørskov, J. K. Electronic Factors Determining the Reactivity of Metal Surfaces. *Surf. Sci.* **1995**, *343*, 211–220.
- (197) Hammer, B.; Nørskov, J. K. Theoretical Surface Science and Catalysis—Calculations and Concepts. *Adv. Catal.* **2000**, *45*, 71–127.
- (198) Stamenkovic, V.; Mun, B. S.; Mayrhofer, K. J. J.; Ross, P. N.; Markovic, N. M.; Rossmeisl, J.; Greeley, J.; Nørskov, J. K. Changing the Activity of Electrocatalysts for Oxygen Reduction by Tuning the Surface Electronic Structure. *Angew. Chem., Int. Ed.* **2006**, *45*, 2897–2901.
- (199) Yin, Z.; Zheng, H.; Ma, D.; Bao, X. Porous Palladium Nanoflowers That Have Enhanced Methanol Electro-Oxidation Activity. *J. Phys. Chem. C* **2009**, *113*, 1001–1005.
- (200) Zhou, D.; Ji, Z.; Jiang, X.; Dunphy, D. R.; Brinker, J.; Keller, A. A. Influence of Material Properties on TiO<sub>2</sub> Nanoparticle Agglomeration. *PLoS One* **2013**, *8*, e81239.

- (201) Liu, H. H.; Surawanijit, S.; Rallo, R.; Orkoulas, G.; Cohen, Y. Analysis of Nanoparticle Agglomeration in Aqueous Suspensions via Constant-Number Monte Carlo Simulation. *Environ. Sci. Technol.* **2011**, *45*, 9284–9292.
- (202) Ye, K.-H.; Zhou, S.-A.; Zhu, X.-C.; Xu, C.-W.; Shen, P. K. Stability Analysis of Oxide ( $\text{CeO}_2$ ,  $\text{NiO}$ ,  $\text{Co}_3\text{O}_4$  and  $\text{Mn}_3\text{O}_4$ ) Effect on Pd/C for Methanol Oxidation in Alkaline Medium. *Electrochim. Acta* **2013**, *90*, 108–111.
- (203) Singh, R. N.; Singh, A.; Anindita. Electrocatalytic Activity of Binary and Ternary Composite Films of Pd, MWCNT and Ni, Part II: Methanol Electrooxidation in 1M KOH. *Int. J. Hydrogen Energy* **2009**, *34*, 2052–2057.
- (204) Nagaraju, D. H.; Devaraj, S.; Balaya, P. Palladium Nanoparticles Anchored on Graphene Nanosheets: Methanol, Ethanol Oxidation Reactions and Their Kinetic Studies. *Mater. Res. Bull.* **2014**, *60*, 150–157.
- (205) Safavi, A.; Kazemi, H.; Kazemi, S. H. In Situ Electrodeposition of Graphene/nano-Palladium on Carbon Cloth for Electrooxidation of Methanol in Alkaline Media. *J. Power Sources* **2014**, *256*, 354–360.
- (206) Iwai, Y.; Ikemoto, S.; Haramaki, K.; Hattori, R.; Yonezawa, S. Influence of Ligands of Palladium Complexes on palladium/Nafion Composite Membranes for Direct Methanol Fuel Cells by Supercritical  $\text{CO}_2$  Impregnation Method. *J. Supercrit. Fluids* **2014**, *94*, 48–58.
- (207) Thiam, H. S.; Daud, W. R. W.; Kamarudin, S. K.; Mohamad, A. B.; Kadhum, A. A. H.; Loh, K. S.; Majlan, E. H. Performance of Direct Methanol Fuel Cell with a Palladium–silica Nanofibre/Nafion Composite Membrane. *Energy Convers. Manage.* **2013**, *75*, 718–726.
- (208) Brandão, L.; Rodrigues, J.; Madeira, L. M.; Mendes, A. Methanol Crossover Reduction by Nafion Modification with Palladium Composite Nanoparticles: Application to Direct Methanol Fuel Cells. *Int. J. Hydrogen Energy* **2010**, *35*, 11561–11567.
- (209) Martinez, U.; Serov, A.; Padilla, M.; Atanassov, P. Mechanistic Insight into Oxide-Promoted Palladium Catalysts for the Electro-Oxidation of Ethanol. *ChemSusChem* **2014**, *7*, 2351–2357.
- (210) Hong, W.; Fang, Y.; Wang, J.; Wang, E. One-Step and Rapid Synthesis of Porous Pd Nanoparticles with Superior Catalytic Activity toward Ethanol/formic Acid Electrooxidation. *J. Power Sources* **2014**, *248*, 553–559.
- (211) Li, Y.; Xu, Q.; Li, Q.-Y.; Wang, H.; Huang, Y.; Xu, C. Pd Deposited on MWCNTs Modified Carbon Fiber Paper as High-Efficient Electrocatalyst for Ethanol Electrooxidation. *Electrochim. Acta* **2014**, *147*, 151–156.
- (212) Hu, F.; Ding, F.; Song, S.; Shen, P. K. Pd Electrocatalyst Supported on Carbonized TiO<sub>2</sub> Nanotube for Ethanol Oxidation. *J. Power Sources* **2006**, *163*, 415–419.
- (213) Fang, X.; Wang, L.; Shen, P. K.; Cui, G.; Bianchini, C. An In Situ Fourier Transform Infrared Spectroelectrochemical Study on Ethanol Electrooxidation on Pd in Alkaline Solution. *J. Power Sources* **2010**, *195*, 1375–1378.
- (214) Nguyen, S. T.; Law, H. M.; Nguyen, H. T.; Kristian, N.; Wang, S.; Chan, S. H.; Wang, X. Enhancement Effect of Ag for Pd/C towards the Ethanol Electro-Oxidation in Alkaline Media. *Appl. Catal., B* **2009**, *91*, 507–515.
- (215) Xu, J. B.; Zhao, T. S.; Shen, S. Y.; Li, Y. S. Stabilization of the Palladium Electrocatalyst with Alloyed Gold for Ethanol Oxidation. *Int. J. Hydrogen Energy* **2010**, *35*, 6490–6500.
- (216) Maiyalagan, T.; Scott, K. Performance of Carbon Nanofiber Supported Pd–Ni Catalysts for Electro-Oxidation of Ethanol in Alkaline Medium. *J. Power Sources* **2010**, *195*, 5246–5251.
- (217) Lamy, C.; Devadas, A.; Simoes, M.; Coutanceau, C. Clean Hydrogen Generation through the Electrocatalytic Oxidation of Formic Acid in a Proton Exchange Membrane Electrolysis Cell (PEMEC). *Electrochim. Acta* **2012**, *60*, 112–120.
- (218) Jiang, K.; Zhang, H.-X.; Zou, S.; Cai, W.-B. Electrocatalysis of Formic Acid on Palladium and Platinum Surfaces: From Fundamental Mechanisms to Fuel Cell Applications. *Phys. Chem. Chem. Phys.* **2014**, *16*, 20360–20376.
- (219) Mikołajczuk, A.; Borodzinski, A.; Kedzierszawski, P.; Stobinski, L.; Mierzwa, B.; Dziura, R. Deactivation of Carbon Supported Palladium Catalyst in Direct Formic Acid Fuel Cell. *Appl. Surf. Sci.* **2011**, *257*, 8211–8214.
- (220) Zhou, W. P.; Lewera, A.; Larsen, R.; Masel, R. L.; Bagus, P. S.; Wieckowski, A. Size Effects in Electronic and Catalytic Properties of Unsupported Palladium Nanoparticles in Electrooxidation of Formic Acid. *J. Phys. Chem. B* **2006**, *110*, 13393–13398.
- (221) Zhou, Y.; Liu, J.; Ye, J.; Zou, Z.; Ye, J.; Gu, J.; Yu, T.; Yang, A. Poisoning and Regeneration of Pd Catalyst in Direct Formic Acid Fuel Cell. *Electrochim. Acta* **2010**, *55*, 5024–5027.
- (222) Miyake, H.; Okada, T.; Samjeské, G.; Osawa, M. Formic Acid Electrooxidation on Pd in Acidic Solutions Studied by Surface-Enhanced Infrared Absorption Spectroscopy. *Phys. Chem. Chem. Phys.* **2008**, *10*, 3662–3669.
- (223) Baik, S. M.; Han, J.; Kim, J.; Kwon, Y. Effect of Deactivation and Reactivation of Palladium Anode Catalyst on Performance of Direct Formic Acid Fuel Cell (DFAFC). *Int. J. Hydrogen Energy* **2011**, *36*, 14719–14724.
- (224) Şennik, E.; Soysal, U.; Öztürk, Z. Z. Pd Loaded Spider-Web TiO<sub>2</sub> Nanowires: Fabrication, Characterization and Gas Sensing Properties. *Sens. Actuators, B* **2014**, *199*, 424–432.
- (225) Meng, D.; Yamazaki, T.; Kikuta, T. Preparation and Gas Sensing Properties of Undoped and Pd-Doped TiO<sub>2</sub> Nanowires. *Sens. Actuators, B* **2014**, *190*, 838–843.
- (226) Pan, Y.; Zhang, R.; Blair, S. L. Anode Poisoning Study in Direct Formic Acid Fuel Cells. *Electrochim. Solid-State Lett.* **2009**, *12*, B23–B26.
- (227) Jeon, H.; Jeong, B.; Choun, M.; Lee, J. In-Situ Electrochemical Extended X-Ray Absorption Fine Structure Spectroscopy Study on the Reactivation of Pd Electrocatalyst in Formic Acid Oxidation. *Electrochim. Acta* **2014**, *140*, 525–528.
- (228) Corcoran, C. J.; Tavassol, H.; Rigsby, M. A.; Bagus, P. S.; Wieckowski, A. Application of XPS to Study Electrocatalysts for Fuel Cells. *J. Power Sources* **2010**, *195*, 7856–7879.
- (229) Zhou, W.; Lee, J. Y. Particle Size Effects in Pd-Catalyzed Electrooxidation of Formic Acid. *J. Phys. Chem. C* **2008**, *112*, 3789–3793.
- (230) Hoshi, N.; Nakamura, M.; Kida, K. Structural Effects on the Oxidation of Formic Acid on the High Index Planes of Palladium. *Electrochim. Commun.* **2007**, *9*, 279–282.
- (231) Hoshi, N.; Kida, K.; Nakamura, M.; Nakada, M.; Osada, K. Structural Effects of Electrochemical Oxidation of Formic Acid on Single Crystal Electrodes of Palladium. *J. Phys. Chem. B* **2006**, *110*, 12480–12484.
- (232) Lee, Y.-W.; Oh, J.-K.; Kim, H.-S.; Lee, J.-K.; Han, S.-B.; Choi, W.; Park, K.-W. Shape-Controlled Pd Nanostructure Catalysts for Highly Efficient Electrochemical Power Sources. *J. Power Sources* **2010**, *195*, 5896–5901.
- (233) Zhang, B.; Peng, H.; Yang, L.; Li, H.; Nan, H.; Liang, Z.; Song, H.; Su, H.; Li, C.; Liao, S. Three Dimensional Palladium Nanoflowers with Enhanced Electrocatalytic Activity towards the Anodic Oxidation of Formic Acid. *J. Mater. Chem. A* **2015**, *3*, 973–977.
- (234) Ren, M.; Zou, L.; Yuan, T.; Huang, Q.; Zou, Z.; Li, X.; Yang, H. Novel Palladium Flower-like Nanostructured Networks for Electrocatalytic Oxidation of Formic Acid. *J. Power Sources* **2014**, *267*, 527–532.
- (235) Dai, L.; Zou, S. Enhanced Formic Acid Oxidation on Cu–Pd Nanoparticles. *J. Power Sources* **2011**, *196*, 9369–9372.
- (236) Chen, D.; Cui, P.; He, H.; Liu, H.; Yang, J. Highly Catalytic Hollow Palladium Nanoparticles Derived from Silver@Silver–Palladium Core–Shell Nanostructures for the Oxidation of Formic Acid. *J. Power Sources* **2014**, *272*, 152–159.
- (237) Wang, Y.-J.; Zhao, N.; Fang, B.; Li, H.; Bi, X. T.; Wang, H. Carbon-Supported Pt-Based Alloy Electrocatalysts for the Oxygen Reduction Reaction in Polymer Electrolyte Membrane Fuel Cells: Particle Size, Shape, and Composition Manipulation and Their Impact to Activity. *Chem. Rev.* **2015**, *115*, 3433–3467.

- (238) Chen, A.; Holt-Hindle, P. Platinum-Based Nanostructured Materials: Synthesis, Properties, and Applications. *Chem. Rev.* **2010**, *110*, 3767–3804.
- (239) Song, C.; Zhang, J. Electrocatalytic Oxygen Reduction Reaction. In *PEM Fuel Cell Electrocatalysts and Catalyst Layers*; Zhang, J., Ed.; Springer: London, 2008; pp 89–134.
- (240) Shim, J. H.; Kim, Y. S.; Kang, M.; Lee, C.; Lee, Y. Electrocatalytic Activity of Nanoporous Pd and Pt: Effect of Structural Features. *Phys. Chem. Chem. Phys.* **2012**, *14*, 3974–3979.
- (241) Lv, J.-J.; Li, S.-S.; Wang, A.-J.; Mei, L.-P.; Feng, J.-J.; Chen, J.-R.; Chen, Z. One-Pot Synthesis of Monodisperse Palladium–copper Nanocrystals Supported on Reduced Graphene Oxide Nanosheets with Improved Catalytic Activity and Methanol Tolerance for Oxygen Reduction Reaction. *J. Power Sources* **2014**, *269*, 104–110.
- (242) Cha, A.; Shim, J. H.; Jo, A.; Lee, S. C.; Lee, Y.; Lee, C. Facile Synthesis of AuPd Nanochain Networks on Carbon Supports and Their Application as Electrocatalysts for Oxygen Reduction Reaction. *Electroanalysis* **2014**, *26*, 723–731.
- (243) Kondo, S.; Nakamura, M.; Maki, N.; Hoshi, N. Active Sites for the Oxygen Reduction Reaction on the Low and High Index Planes of Palladium. *J. Phys. Chem. C* **2009**, *113*, 12625–12628.
- (244) Ou, L.; Chen, S. Comparative Study of Oxygen Reduction Reaction Mechanisms on the Pd(111) and Pt(111) Surfaces in Acid Medium by DFT. *J. Phys. Chem. C* **2013**, *117*, 1342–1349.
- (245) Hoshi, N.; Nakamura, M.; Kondo, S. Oxygen Reduction Reaction on the Low Index Planes of Palladium Electrodes Modified with a Monolayer of Platinum Film. *Electrochim. Commun.* **2009**, *11*, 2282–2284.
- (246) Zhang, J.; Vukmirovic, M. B.; Sasaki, K.; Nilekar, A. U.; Mavrikakis, M.; Adzic, R. R. Mixed-Metal Pt Monolayer Electrocatalysts for Enhanced Oxygen Reduction Kinetics. *J. Am. Chem. Soc.* **2005**, *127*, 12480–12481.
- (247) Erikson, H.; Sarapuu, A.; Tammeveski, K.; Solla-Gullón, J.; Feliu, J. M. Enhanced Electrocatalytic Activity of Cubic Pd Nanoparticles towards the Oxygen Reduction Reaction in Acid Media. *Electrochim. Commun.* **2011**, *13*, 734–737.
- (248) Huang, K.-L.; Liu, Z.-T.; Lee, C.-L. Truncated Palladium Nanocubes: Synthesis and the Effect of OH– Concentration on Their Catalysis of the Alkaline Oxygen Reduction Reaction. *Electrochim. Acta* **2015**, *157*, 78–87.
- (249) Zhou, W.; Li, M.; Ding, O. L.; Chan, S. H.; Zhang, L.; Xue, Y. Pd Particle Size Effects on Oxygen Electrochemical Reduction. *Int. J. Hydrogen Energy* **2014**, *39*, 6433–6442.
- (250) Fernández, J. L.; Raghubeer, V.; Manthiram, A.; Bard, A. J. Pd–Ti and Pd–Co–Au Electrocatalysts as a Replacement for Platinum for Oxygen Reduction in Proton Exchange Membrane Fuel Cells. *J. Am. Chem. Soc.* **2005**, *127*, 13100–13101.
- (251) Cho, Y.-H.; Choi, B.; Cho, Y.-H.; Park, H.-S.; Sung, Y.-E. Pd-Based PdPt(19:1)/C Electrocatalyst as an Electrode in PEM Fuel Cell. *Electrochim. Commun.* **2007**, *9*, 378–381.
- (252) Rahul, R.; Singh, R. K.; Neergat, M. Effect of Oxidative Heat-Treatment on Electrochemical Properties and Oxygen Reduction Reaction (ORR) Activity of Pd–Co Alloy Catalysts. *J. Electroanal. Chem.* **2014**, *712*, 223–229.
- (253) Cao, D.; Sun, L.; Wang, G.; Lv, Y.; Zhang, M. Kinetics of Hydrogen Peroxide Electrocatalysis on Pd Nanoparticles in Acidic Medium. *J. Electroanal. Chem.* **2008**, *621*, 31–37.
- (254) Yang, F.; Cheng, K.; Mo, Y.; Yu, L.; Yin, J.; Wang, G.; Cao, D. Direct Peroxide–Peroxide Fuel Cell – Part 1: The Anode and Cathode Catalyst of Carbon Fiber Cloth Supported Dendritic Pd. *J. Power Sources* **2012**, *217*, 562–568.
- (255) Yi, Q.; Niu, F. Novel Nanoporous Palladium Catalyst for Electrocatalysis of Hydrogen Peroxide. *Rare Met.* **2011**, *30*, 332–336.
- (256) Medeiros, M. G.; Bessette, R. R.; Deschenes, C. M.; Patriassi, C. J.; Carreiro, L. G.; Tucker, S. P.; Atwater, D. W. Magnesium-Solution Phase Catholyte Semi-Fuel Cell for Undersea Vehicles. *J. Power Sources* **2004**, *136*, 226–231.
- (257) Yang, W.; Yang, S.; Sun, W.; Sun, G.; Xin, Q. Nanostructured Palladium–Silver Coated Nickel Foam Cathode for Magnesium–Hydrogen Peroxide Fuel Cells. *Electrochim. Acta* **2006**, *52*, 9–14.
- (258) Zhang, D.; Ye, K.; Cao, D.; Yin, J.; Cheng, K.; Wang, B.; Xu, Y.; Wang, G. Catalytic Behavior of a Palladium Doped Binder Free Paper Based Cobalt Electrode in Electroreduction of Hydrogen Peroxide. *J. Power Sources* **2015**, *273*, 1142–1147.
- (259) Sun, L.; Cao, D.; Wang, G. Pd–Ru/C as the Electrocatalyst for Hydrogen Peroxide Reduction. *J. Appl. Electrochem.* **2008**, *38*, 1415–1419.
- (260) Ma, J.; Sahai, Y.; Buchheit, R. G. Direct Borohydride Fuel Cell Using Ni-Based Composite Anodes. *J. Power Sources* **2010**, *195*, 4709–4713.
- (261) Yang, F.; Cheng, K.; Wu, T.; Zhang, Y.; Yin, J.; Wang, G.; Cao, D. Au–Pd Nanoparticles Supported on Carbon Fiber Cloth as the Electrocatalyst for H<sub>2</sub>O<sub>2</sub> Electroreduction in Acid Medium. *J. Power Sources* **2013**, *233*, 252–258.
- (262) Yang, F.; Cheng, K.; Wu, T.; Zhang, Y.; Yin, J.; Wang, G.; Cao, D. Dendritic Palladium Decorated with Gold by Potential Pulse Electrodeposition: Enhanced Electrocatalytic Activity for H<sub>2</sub>O<sub>2</sub> Electroreduction and Electooxidation. *Electrochim. Acta* **2013**, *99*, 54–61.
- (263) Yang, F.; Cheng, K.; Liu, X.; Chang, S.; Yin, J.; Du, C.; Du, L.; Wang, G.; Cao, D. Direct Peroxide–peroxide Fuel Cell – Part 2: Effects of Conditions on the Performance. *J. Power Sources* **2012**, *217*, 569–573.
- (264) Zeng, K.; Zhang, D. Recent Progress in Alkaline Water Electrolysis for Hydrogen Production and Applications. *Prog. Energy Combust. Sci.* **2010**, *36*, 307–326.
- (265) Al-Mufachi, N. A.; Rees, N. V.; Steinberger-Wilkins, R. Hydrogen Selective Membranes: A Review of Palladium-Based Dense Metal Membranes. *Renewable Sustainable Energy Rev.* **2015**, *47*, 540–551.
- (266) Wang, M.; Wang, Z.; Gong, X.; Guo, Z. The Intensification Technologies to Water Electrolysis for Hydrogen Production – A Review. *Renewable Sustainable Energy Rev.* **2014**, *29*, 573–588.
- (267) Kishore, S.; Nelson, J. A.; Adair, J. H.; Eklund, P. C. Hydrogen Storage in Spherical and Platelet Palladium Nanoparticles. *J. Alloys Compd.* **2005**, *389*, 234–242.
- (268) Kobayashi, H.; Yamauchi, M.; Kitagawa, H.; Kubota, Y.; Kato, K.; Takata, M. On the Nature of Strong Hydrogen Atom Trapping Inside Pd Nanoparticles. *J. Am. Chem. Soc.* **2008**, *130*, 1828–1829.
- (269) Narehood, D.; Kishore, S.; Goto, H.; Adair, J.; Nelson, J.; Gutierrez, H.; Eklund, P. X-Ray Diffraction and H-Storage in Ultra-Small Palladium Particles. *Int. J. Hydrogen Energy* **2009**, *34*, 952–960.
- (270) Catalano, J.; Giacinti Baschetti, M.; Sarti, G. C. Hydrogen Permeation in Palladium-Based Membranes in the Presence of Carbon Monoxide. *J. Membr. Sci.* **2010**, *362*, 221–233.
- (271) Hatlevik, Ø.; Gade, S. K.; Keeling, M. K.; Thoen, P. M.; Davidson, A. P.; Way, J. D. Palladium and Palladium Alloy Membranes for Hydrogen Separation and Production: History, Fabrication Strategies, and Current Performance. *Sep. Purif. Technol.* **2010**, *73*, 59–64.
- (272) David, E.; Kopac, J. Development of Palladium/ceramic Membranes for Hydrogen Separation. *Int. J. Hydrogen Energy* **2011**, *36*, 4498–4506.
- (273) Li, Y.; Ding, W.; Jin, X.; Yu, J.; Hu, X.; Huang, Y. Toward Extensive Application of Pd/ceramic Membranes for Hydrogen Separation: A Case Study on Membrane Recycling and Reuse in the Fabrication of New Membranes. *Int. J. Hydrogen Energy* **2015**, *40*, 3528–3537.
- (274) Amandusson, H.; Ekedahl, L.; Dannetun, H. Hydrogen Permeation through Surface Modified Pd and PdAg Membranes. *J. Membr. Sci.* **2001**, *193*, 35–47.
- (275) Sakamoto, Y.; Chen, F. L.; Furukawa, M.; Noguchi, M. Permeability and Diffusivity of Hydrogen in Palladium-Rich Pd–Y(Gd)-Ag Ternary Alloys. *J. Alloys Compd.* **1992**, *185*, 191–205.

- (276) Gao, H.; Lin, Y. S.; Li, Y.; Zhang, B. Chemical Stability and Its Improvement of Palladium-Based Metallic Membranes. *Ind. Eng. Chem. Res.* **2004**, *43*, 6920–6930.
- (277) Decaux, C.; Ngameni, R.; Solas, D.; Grigoriev, S.; Millet, P. Time and Frequency Domain Analysis of Hydrogen Permeation across PdCu Metallic Membranes for Hydrogen Purification. *Int. J. Hydrogen Energy* **2010**, *35*, 4883–4892.
- (278) Suleiman, M.; Jisrawi, N. M.; Dankert, O.; Reetz, M. T.; Bähzt, C.; Kirchheim, R.; Pundt, A. Phase Transition and Lattice Expansion during Hydrogen Loading of Nanometer Sized Palladium Clusters. *J. Alloys Compd.* **2003**, *356*–357, 644–648.
- (279) Jia, L.; Bulushev, D. A.; Beloshapkin, S.; Ross, J. R. H. Hydrogen Production from Formic Acid Vapour over a Pd/C Catalyst Promoted by Potassium Salts: Evidence for Participation of Buffer-like Solution in the Pores of the Catalyst. *Appl. Catal., B* **2014**, *160*–161, 35–43.
- (280) Dutta, S. A Review on Production, Storage of Hydrogen and Its Utilization as an Energy Resource. *J. Ind. Eng. Chem.* **2014**, *20*, 1148–1156.
- (281) Yamauchi, M.; Ikeda, R.; Kitagawa, H.; Takata, M. Nanosize Effects on Hydrogen Storage in Palladium. *J. Phys. Chem. C* **2008**, *112*, 3294–3299.
- (282) Zhao, W.; Fierro, V.; Zlotea, C.; Izquierdo, M. T.; Chevalier-César, C.; Latroche, M.; Celzard, A. Activated Carbons Doped with Pd Nanoparticles for Hydrogen Storage. *Int. J. Hydrogen Energy* **2012**, *37*, 5072–5080.
- (283) Ansón, A.; Lafuente, E.; Urriolabeitia, E.; Navarro, R.; Benito, A. M.; Maser, W. K.; Martínez, M. T. Hydrogen Capacity of Palladium-Loaded Carbon Materials. *J. Phys. Chem. B* **2006**, *110*, 6643–6648.
- (284) Campesi, R.; Cuevas, F.; Gadiou, R.; Leroy, E.; Hirscher, M.; Vix-Guterl, C.; Latroche, M. Hydrogen Storage Properties of Pd Nanoparticle/Carbon Template Composites. *Carbon* **2008**, *46*, 206–214.
- (285) López-Corral, I.; Germán, E.; Juan, A.; Volpe, M. A.; Brizuela, G. P. Hydrogen Adsorption on Palladium Dimer Decorated Graphene: A Bonding Study. *Int. J. Hydrogen Energy* **2012**, *37*, 6653–6665.
- (286) Contescu, C. I.; van Benthem, K.; Li, S.; Bonifacio, C. S.; Pennycook, S. J.; Jena, P.; Gallego, N. C. Single Pd Atoms in Activated Carbon Fibers and Their Contribution to Hydrogen Storage. *Carbon* **2011**, *49*, 4050–4058.
- (287) Wildgoose, G. G.; Banks, C. E.; Compton, R. G. Metal Nanoparticles and Related Materials Supported on Carbon Nanotubes: Methods and Applications. *Small* **2006**, *2*, 182–193.
- (288) Zacharia, R.; Kim, K. Y.; Fazle Kibria, A. K. M.; Nahm, K. S. Enhancement of Hydrogen Storage Capacity of Carbon Nanotubes via Spill-over from Vanadium and Palladium Nanoparticles. *Chem. Phys. Lett.* **2005**, *412*, 369–375.
- (289) Chen, C.-H.; Chung, T.-Y.; Shen, C.-C.; Yu, M.-S.; Tsao, C.-S.; Shi, G.-N.; Huang, C.-C.; Ger, M.-D.; Lee, W.-L. Hydrogen Storage Performance in Palladium-Doped Graphene/Carbon Composites. *Int. J. Hydrogen Energy* **2013**, *38*, 3681–3688.
- (290) Chen, S.; Ostrom, C.; Chen, A. Functionalization of TiO<sub>2</sub> Nanotubes with Palladium Nanoparticles for Hydrogen Sorption and Storage. *Int. J. Hydrogen Energy* **2013**, *38*, 14002–14009.
- (291) Cheon, Y. E.; Suh, M. P. Enhanced Hydrogen Storage by Palladium Nanoparticles Fabricated in a Redox-Active Metal-Organic Framework. *Angew. Chem., Int. Ed.* **2009**, *48*, 2899–2903.
- (292) Zlotea, C.; Campesi, R.; Cuevas, F.; Leroy, E.; Dibandjo, P.; Volkinger, C.; Loiseau, T.; Férey, G.; Latroche, M. Pd Nanoparticles Embedded into a Metal-Organic Framework: Synthesis, Structural Characteristics, and Hydrogen Sorption Properties. *J. Am. Chem. Soc.* **2010**, *132*, 2991–2997.
- (293) Contescu, C. I.; Brown, C. M.; Liu, Y.; Bhat, V. V.; Gallego, N. C. Detection of Hydrogen Spillover in Palladium-Modified Activated Carbon Fibers during Hydrogen Adsorption. *J. Phys. Chem. C* **2009**, *113*, 5886–5890.
- (294) Ma, L.; Zhang, J.-M.; Xu, K.-W. Hydrogen Storage on Nitrogen Induced Defects in Palladium-Decorated Graphene: A First-Principles Study. *Appl. Surf. Sci.* **2014**, *292*, 921–927.
- (295) Rangel, E.; Sansores, E. Theoretical Study of Hydrogen Adsorption on Nitrogen Doped Graphene Decorated with Palladium Clusters. *Int. J. Hydrogen Energy* **2014**, *39*, 6558–6566.
- (296) Ma, L.; Zhang, J.-M.; Xu, K.-W.; Ji, V. Hydrogen Adsorption and Storage on Palladium-Decorated Graphene with Boron Dopants and Vacancy Defects: A First-Principles Study. *Phys. E* **2015**, *66*, 40–47.
- (297) Lueking, A. Hydrogen Spillover to Enhance Hydrogen Storage—Study of the Effect of Carbon Physicochemical Properties. *Appl. Catal., A* **2004**, *265*, 259–268.
- (298) Konda, S. K.; Chen, A. Palladium Based Nanomaterials for Enhanced Hydrogen Spillover and Storage. *Mater. Today* **2015**, DOI: 10.1016/j.mattod.2015.08.002.
- (299) Ostrom, C. K.; Chen, A. Synthesis and Electrochemical Study of Pd-Based Trimetallic Nanoparticles for Enhanced Hydrogen Storage. *J. Phys. Chem. C* **2013**, *117*, 20456–20464.
- (300) Hübert, T.; Boon-Brett, L.; Black, G.; Banach, U. Hydrogen Sensors – A Review. *Sens. Actuators, B* **2011**, *157*, 329–352.
- (301) Hübert, T.; Boon-Brett, L.; Palmisano, V.; Bader, M. A. Developments in Gas Sensor Technology for Hydrogen Safety. *Int. J. Hydrogen Energy* **2014**, *39*, 20474–20483.
- (302) Gupta, D.; Dutta, D.; Kumar, M.; Barman, P. B.; Sarkar, C. K.; Basu, S.; Hazra, S. K. A Low Temperature Hydrogen Sensor Based on Palladium Nanoparticles. *Sens. Actuators, B* **2014**, *196*, 215–222.
- (303) Noh, J.-S.; Lee, J. M.; Lee, W. Low-Dimensional Palladium Nanostructures for Fast and Reliable Hydrogen Gas Detection. *Sensors* **2011**, *11*, 825–851.
- (304) Phan, D.-T.; Chung, G.-S. Effects of Pd Nanocube Size of Pd Nanocube-Graphene Hybrid on Hydrogen Sensing Properties. *Sens. Actuators, B* **2014**, *204*, 437–444.
- (305) Pan, Y.-T.; Yin, X.; Kwok, K. S.; Yang, H. Higher-Order Nanostructures of Two-Dimensional Palladium Nanosheets for Fast Hydrogen Sensing. *Nano Lett.* **2014**, *14*, 5953–5959.
- (306) Chen, X.; Wong, C. K. Y.; Yuan, C. A.; Zhang, G. Nanowire-Based Gas Sensors. *Sens. Actuators, B* **2013**, *177*, 178–195.
- (307) Kolmakov, A.; Klenov, D. O.; Lilach, Y.; Stemmer, S.; Moskovits, M. Enhanced Gas Sensing by Individual SnO<sub>2</sub> Nanowires and Nanobelts Functionalized with Pd Catalyst Particles. *Nano Lett.* **2005**, *5*, 667–673.
- (308) Liu, J.; Li, G. A Remote Sensor for Detecting Methane Based on Palladium-Decorated Single Walled Carbon Nanotubes. *Sensors* **2013**, *13*, 8814–8826.
- (309) Marikutsa, A. V.; Rumyantseva, M. N.; Yashina, L. V.; Gaskov, A. M. Role of Surface Hydroxyl Groups in Promoting Room Temperature CO Sensing by Pd-Modified Nanocrystalline SnO<sub>2</sub>. *J. Solid State Chem.* **2010**, *183*, 2389–2399.
- (310) Kim, B.; Lu, Y.; Hannon, A.; Meyyappan, M.; Li, J. Low Temperature Pd/SnO<sub>2</sub> Sensor for Carbon Monoxide Detection. *Sens. Actuators, B* **2013**, *177*, 770–775.
- (311) Yoosefian, M.; Barzgari, Z.; Yoosefian, J. Ab Initio Study of Pd-Decorated Single-Walled Carbon Nanotube with C-Vacancy as CO Sensor. *Struct. Chem.* **2014**, *25*, 9–19.
- (312) Antonaroli, S.; Crociani, B.; Di Natale, C.; Nardis, S.; Stefanelli, M.; Paolesse, R. Palladium Complexes Based Nanogravimetric Sensors for Carbon Monoxide Detection. *Sens. Actuators, B* **2015**, *208*, 334–338.
- (313) Athawale, A. A.; Bhagwat, S. V.; Katre, P. P. Nanocomposite of Pd-Polyaniline as a Selective Methanol Sensor. *Sens. Actuators, B* **2006**, *114*, 263–267.
- (314) Rai, P.; Yu, Y.-T. Citrate-Assisted One-Pot Assembly of Palladium Nanoparticles onto ZnO Nanorods for CO Sensing Application. *Mater. Chem. Phys.* **2013**, *142*, 545–548.
- (315) Chen, X.; Wu, G.; Cai, Z.; Oyama, M.; Chen, X. Advances in Enzyme-Free Electrochemical Sensors for Hydrogen Peroxide, Glucose, and Uric Acid. *Microchim. Acta* **2014**, *181*, 689–705.

- (316) Liu, H.; Chen, X.; Huang, L.; Wang, J.; Pan, H. Palladium Nanoparticles Embedded into Graphene Nanosheets: Preparation, Characterization, and Nonenzymatic Electrochemical Detection of  $H_2O_2$ . *Electroanalysis* **2014**, *26*, 556–564.
- (317) Huang, J.; Wang, D.; Hou, H.; You, T. Electrospun Palladium Nanoparticle-Loaded Carbon Nanofibers and Their Electrocatalytic Activities towards Hydrogen Peroxide and NADH. *Adv. Funct. Mater.* **2008**, *18*, 441–448.
- (318) Wang, J.; Wang, Z.; Zhao, D.; Xu, C. Facile Fabrication of Nanoporous PdFe Alloy for Nonenzymatic Electrochemical Sensing of Hydrogen Peroxide and Glucose. *Anal. Chim. Acta* **2014**, *832*, 34–43.
- (319) Hosseini, H.; Rezaei, S. J. T.; Rahmani, P.; Sharifi, R.; Nabid, M. R.; Bagheri, A. Nonenzymatic Glucose and Hydrogen Peroxide Sensors Based on Catalytic Properties of Palladium Nanoparticles/poly(3,4-Ethylenedioxythiophene) Nanofibers. *Sens. Actuators, B* **2014**, *195*, 85–91.
- (320) Huang, J.; Liu, Y.; Hou, H.; You, T. Simultaneous Electrochemical Determination of Dopamine, Uric Acid and Ascorbic Acid Using Palladium Nanoparticle-Loaded Carbon Nanofibers Modified Electrode. *Biosens. Bioelectron.* **2008**, *24*, 632–637.
- (321) Zhang, X.; Cao, Y.; Yu, S.; Yang, F.; Xi, P. An Electrochemical Biosensor for Ascorbic Acid Based on Carbon-Supported PdNinano-particles. *Biosens. Bioelectron.* **2013**, *44*, 183–190.
- (322) Reddaiah, K.; Reddy, T. M.; Mallikarjuna, K.; Narasimha, G. Electrochemical Detection of Dopamine at Poly(solochrome cyanine)/Pd Nanoparticles Doped Modified Carbon Paste Electrode and Simultaneous Resolution in the Presence of Ascorbic Acid and Uric Acid: A Voltammetric Method. *Anal. Methods* **2013**, *5*, 5627–5636.
- (323) Chen, A.; Chatterjee, S. Nanomaterials Based Electrochemical Sensors for Biomedical Applications. *Chem. Soc. Rev.* **2013**, *42*, 5425–5438.
- (324) Chen, X.; Lin, Z.; Chen, D.-J.; Jia, T.; Cai, Z.; Wang, X.; Chen, X.; Chen, G.; Oyama, M. Nonenzymatic Amperometric Sensing of Glucose by Using Palladium Nanoparticles Supported on Functional Carbon Nanotubes. *Biosens. Bioelectron.* **2010**, *25*, 1803–1808.
- (325) Lu, L.-M.; Li, H.-B.; Qu, F.; Zhang, X.-B.; Shen, G.-L.; Yu, R.-Q. In Situ Synthesis of Palladium Nanoparticle–Graphene Nano-hybrids and Their Application in Nonenzymatic Glucose Biosensors. *Biosens. Bioelectron.* **2011**, *26*, 3500–3504.
- (326) Zeng, Q.; Cheng, J.-S.; Liu, X.-F.; Bai, H.-T.; Jiang, J.-H. Palladium Nanoparticle/Chitosan-Grafted Graphene Nanocomposites for Construction of a Glucose Biosensor. *Biosens. Bioelectron.* **2011**, *26*, 3456–3463.
- (327) Singh, B.; Bhardwaj, N.; Jain, V. K.; Bhatia, V. Palladium Nanoparticles Decorated Electrostatically Functionalized MWCNTs as a Non Enzymatic Glucose Sensor. *Sens. Actuators, A* **2014**, *220*, 126–133.
- (328) Chung, T.-Y.; Tsao, C.-S.; Tseng, H.-P.; Chen, C.-H.; Yu, M.-S. Effects of Oxygen Functional Groups on the Enhancement of the Hydrogen Spillover of Pd-Doped Activated Carbon. *J. Colloid Interface Sci.* **2015**, *441*, 98–105.
- (329) Winkler, K.; Grodzka, E.; D’Souza, F.; Balch, A. L. Two-Component Films of Fullerene and Palladium as Materials for Electrochemical Capacitors. *J. Electrochem. Soc.* **2007**, *154*, K1–10.
- (330) Łukaszewski, M.; Hubkowska, K.; Koss, U.; Czerwiński, A. Characteristic of Hydrogen-Saturated Pd-Based Alloys for the Application in Electrochemical Capacitors. *J. Solid State Electrochem.* **2012**, *16*, 2533–2539.
- (331) Łukaszewski, M.; Żurowski, A.; Czerwiński, A. Hydrogen in Thin Pd-Based Layers Deposited on Reticulated Vitreous carbon—A New System for Electrochemical Capacitors. *J. Power Sources* **2008**, *185*, 1598–1604.
- (332) Branciewicz, E.; Grądzka, E.; Winkler, K. Comparison of Electrochemical Properties of Two-Component C60-Pd Polymers Formed under Electrochemical Conditions and by Chemical Synthesis. *J. Solid State Electrochem.* **2013**, *17*, 1233–1245.
- (333) Branciewicz, E.; Grądzka, E.; Basa, A.; Winkler, K. Chemical Synthesis and Characterization of the C60-Pd Polymer Spherical Nanoparticles. *Electrochim. Acta* **2014**, *128*, 91–101.
- (334) Grądzka, E.; Winkler, K.; Borowska, M.; Plonska-Brzezinska, M. E.; Echegoyen, L. Comparison of the Electrochemical Properties of Thin Films of MWCNTs/C60-Pd, SWCNTs/C60-Pd and Ox-CNOs/C60-Pd. *Electrochim. Acta* **2013**, *96*, 274–284.
- (335) El-Sheikh, S. M.; Ismail, A. A.; Al-Sharab, J. F. Catalytic Reduction of P-Nitrophenol over Precious Metals/highly Ordered Mesoporous Silica. *New J. Chem.* **2013**, *37*, 2399–2407.
- (336) Dong, Z.; Le, X.; Dong, C.; Zhang, W.; Li, X.; Ma, J. Ni@Pd Core–shell Nanoparticles Modified Fibrous Silica Nanospheres as Highly Efficient and Recoverable Catalyst for Reduction of 4-Nitrophenol and Hydrodechlorination of 4-Chlorophenol. *Appl. Catal., B* **2015**, *162*, 372–380.
- (337) Premkumar, T.; Geckeler, K. E. Synthesis of Honeycomb-like Palladium Nanostructures by Using cucurbit[7]uril and Their Catalytic Activities for Reduction of 4-Nitrophenol. *Mater. Chem. Phys.* **2014**, *148*, 772–777.
- (338) Xue, Y.; Lu, X.; Bian, X.; Lei, J.; Wang, C. Facile Synthesis of Highly Dispersed Palladium/Polypyrrole Nanocapsules for Catalytic Reduction of P-Nitrophenol. *J. Colloid Interface Sci.* **2012**, *379*, 89–93.
- (339) Li, H.; Han, L.; Cooper-White, J.; Kim, I. Palladium Nanoparticles Decorated Carbon Nanotubes: Facile Synthesis and Their Applications as Highly Efficient Catalysts for the Reduction of 4-Nitrophenol. *Green Chem.* **2012**, *14*, 586–591.
- (340) Sun, T.; Zhang, Z.; Xiao, J.; Chen, C.; Xiao, F.; Wang, S.; Liu, Y. Facile and Green Synthesis of Palladium Nanoparticles-Graphene-Carbon Nanotube Material with High Catalytic Activity. *Sci. Rep.* **2013**, *3*, DOI: [10.1038/srep02527](https://doi.org/10.1038/srep02527).
- (341) Gao, D.; Zhou, H.; Wang, J.; Miao, S.; Yang, F.; Wang, G.; Wang, J.; Bao, X. Size-Dependent Electrocatalytic Reduction of  $CO_2$  over Pd Nanoparticles. *J. Am. Chem. Soc.* **2015**, *137*, 4288–4291.
- (342) Lu, G.; Wang, H.; Bian, Z.; Liu, X. Electrochemical Reduction of  $CO_2$  to Organic Acids by a Pd-MWNTs Gas-Diffusion Electrode in Aqueous Medium. *Sci. World J.* **2013**, *2013*, 1–8.
- (343) Ha, S.; Larsen, R.; Masel, R. I. Performance Characterization of Pd/C Nanocatalyst for Direct Formic Acid Fuel Cells. *J. Power Sources* **2005**, *144*, 28–34.
- (344) Shen, P. K.; Xu, C. Alcohol Oxidation on Nanocrystalline Oxide Pd/C Promoted Electrocatalysts. *Electrochim. Commun.* **2006**, *8*, 184–188.
- (345) Qu, W.-L.; Wang, Z.-B.; Sui, X.-L.; Gu, D.-M.; Yin, G.-P. Titanium Compounds TiC–C and  $TiO_2$ –C Supported Pd Catalysts for Formic Acid Electrooxidation. *Int. J. Hydrogen Energy* **2012**, *37*, 15096–15104.
- (346) Pattabiraman, R. Electrochemical Investigations on Carbon Supported Palladium Catalysts. *Appl. Catal., A* **1997**, *153*, 9–20.
- (347) Hu, F. P.; Wang, Z.; Li, Y.; Li, C.; Zhang, X.; Shen, P. K. Improved Performance of Pd Electrocatalyst Supported on Ultrahigh Surface Area Hollow Carbon Spheres for Direct Alcohol Fuel Cells. *J. Power Sources* **2008**, *177*, 61–66.
- (348) Bambagioni, V.; Bianchini, C.; Marchionni, A.; Filippi, J.; Vizza, F.; Teddy, J.; Serp, P.; Zhiani, M. Pd and Pt–Ru Anode Electrocatalysts Supported on Multi-Walled Carbon Nanotubes and Their Use in Passive and Active Direct Alcohol Fuel Cells with an Anion-Exchange Membrane (Alcohol = Methanol, Ethanol, Glycerol). *J. Power Sources* **2009**, *190*, 241–251.
- (349) An, H.; Cui, H.; Zhou, D.; Tao, D.; Li, B.; Zhai, J.; Li, Q. Synthesis and Performance of Pd/SnO<sub>2</sub>–TiO<sub>2</sub>/MWCNT Catalysts for Direct Formic Acid Fuel Cell Application. *Electrochim. Acta* **2013**, *92*, 176–182.
- (350) Gooding, J. J. Nanostructuring Electrodes with Carbon Nanotubes: A Review on Electrochemistry and Applications for Sensing. *Electrochim. Acta* **2005**, *50*, 3049–3060.
- (351) Trojanowicz, M. Analytical Applications of Carbon Nanotubes: A Review. *TrAC, Trends Anal. Chem.* **2006**, *25*, 480–489.
- (352) Yang, S.; Dong, J.; Yao, Z.; Shen, C.; Shi, X.; Tian, Y.; Lin, S.; Zhang, X. One-Pot Synthesis of Graphene-Supported Monodisperse Pd Nanoparticles as Catalyst for Formic Acid Electro-Oxidation. *Sci. Rep.* **2014**, *4*, 1–6.

- (353) Yan, H.; Bai, Z.; Chao, S.; Yang, L.; Cui, Q.; Wang, K.; Niu, L. Synthesis of a Low Palladium Dosage Catalyst and Its High Performance Promoted by  $\text{Fe}_2\text{O}_3$  for Ethanol Electrooxidation. *RSC Adv.* **2013**, *3*, 20332–20337.
- (354) Huang, H.; Wang, X. Design and Synthesis of Pd– $\text{MnO}_2$  Nanolamella–graphene Composite as a High-Performance Multifunctional Electrocatalyst towards Formic Acid and Methanol Oxidation. *Phys. Chem. Chem. Phys.* **2013**, *15*, 10367–10375.
- (355) Thapa, A. K.; Shin, T. H.; Ida, S.; Sumanasekera, G. U.; Sunkara, M. K.; Ishihara, T. Gold–Palladium Nanoparticles Supported by Mesoporous B- $\text{MnO}_2$  Air Electrode for Rechargeable Li-Air Battery. *J. Power Sources* **2012**, *220*, 211–216.
- (356) Liu, P.; Lee, S.-H.; Cheong, H. M.; Tracy, C. E.; Pitts, J. R.; Smith, R. D. Stable Pd/ $\text{V}_2\text{O}_5$  Optical  $\text{H}_2$  Sensor. *J. Electrochem. Soc.* **2002**, *149*, H76–80.
- (357) Maciąk, E.; Opilski, Z.; Urbańczyk, M. Pd/ $\text{V}_2\text{O}_5$  Fiber Optic Hydrogen Gas Sensor. *J. Phys. IV* **2005**, *129*, 137–141.
- (358) Chen, S.; Bi, J.; Zhao, Y.; Yang, L.; Zhang, C.; Ma, Y.; Wu, Q.; Wang, X.; Hu, Z. Nitrogen-Doped Carbon Nanocages as Efficient Metal-Free Electrocatalysts for Oxygen Reduction Reaction. *Adv. Mater.* **2012**, *24*, 5593–5597.
- (359) Lv, J.-J.; Feng, J.-X.; Li, S.-S.; Wang, Y.-Y.; Wang, A.-J.; Zhang, Q.-L.; Chen, J.-R.; Feng, J.-J. Ionic Liquid Crystal-Assisted Synthesis of PtAg Nanoflowers on Reduced Graphene Oxide and Their Enhanced Electrocatalytic Activity toward Oxygen Reduction Reaction. *Electrochim. Acta* **2014**, *133*, 407–413.
- (360) Hamoudi, Z.; Aïssa, B.; El Khakani, M. A.; Mohamedi, M. Electrocatalytic Reduction of Oxygen at Binderless Carbon-Pt Nanostructured Electrodes: Effects of the Nature of the Carbon Support and the Pt Morphology. *Int. J. Electrochem. Sci.* **2012**, *7*, 12227–12235.
- (361) Dai, L.; Xue, Y.; Qu, L.; Choi, H.-J.; Baek, J.-B. Metal-Free Catalysts for Oxygen Reduction Reaction. *Chem. Rev.* **2015**, *115*, 4823–4892.